INL/EXT-06-01382

Developing and Evaluating Candidate Materials for Generation IV Supercritical Water Reactors

Final Technical Report
INERI 2003-008-K

J.I. Cole
J.L. Rempe
T.C. Totemeier
G.S. Was
K. Sridharan
T. Allen
J. Jang
S. Hong

March 2006

The INL is a U.S. Department of Energy National Laboratory
operated by Battelle Energy Alliance

INL/EXT-06-01382

Developing and Evaluating Candidate Materials for Generation IV Supercritical Water Reactors

Final Technical Report
INERI 2003-008-K

J.I. Cole[a]
J.L. Rempe[a]
T.C. Totemeier[a]
G.S. Was[b]
K. Sridharan[c]
T. Allen[c]
J. Jang[d]
S. Hong[e]

[a]Idaho National Laboratory
[b]University of Michigan
[c]University of Wisconsin
[d]Korea Atomic Energy Research Institute
[e]Korea Advanced Institute of Science and Technology

March 2006

Idaho National Laboratory
Idaho Falls, Idaho 83415

Prepared for the
U.S. Department of Energy
Office of Nuclear Energy
Under DOE Idaho Operations Office
Contract DE-AC07-05ID14517

INTERNATIONAL NUCLEAR ENERGY RESEARCH INITIATIVE

Developing and Evaluating Candidate Materials for Generation IV Supercritical Water Reactors

PI (U.S.): J. I. Cole, Idaho National Laboratory

PI (Korea): J. Jang, Korea Atomic Energy Research Institute

Collaborators: University of Michigan, University of Wisconsin, Korea Advanced Institute for Science and Technology

Project Number: 2003-008-K

Project Start Date: January 2003

Project End Date: December 2005

EXUCUTIVE SUMMARY

Research Objectives

The Generation IV Supercritical Water Reactor (GEN IV SCWR) is being proposed as an advanced high efficiency thermal reactor for baseload electricity production. One of the major unknowns with this reactor concept is the behavior of fuel cladding and structural components under the extremely aggressive SCWR environment. The objective of this project was to evaluate candidate materials for SCWR application. The path the project has taken is to first determine the most likely candidate materials by surveying the literature in three principle areas; existing supercritical water fossil plants (SCFP), commercial light-water reactors (LWR) and DOE research programs in liquid-metal-fast-breeder (LMFBR) and fusion reactors. The work then entailed efforts to evaluate candidate alloys in terms of high temperature mechanical properties, corrosion and stress corrosion cracking, radiation stability. As the diagram in Figure 1 below depicts, the qualification testing was designed to provide a better understanding of likely degradation processes, aiding in the development of potential mitigation strategies. Two anticipated outcomes of the project are the production of information that can ultimately be used by SCWR system designers and guidance for future investigations involving in-reactor irradiation experiments.

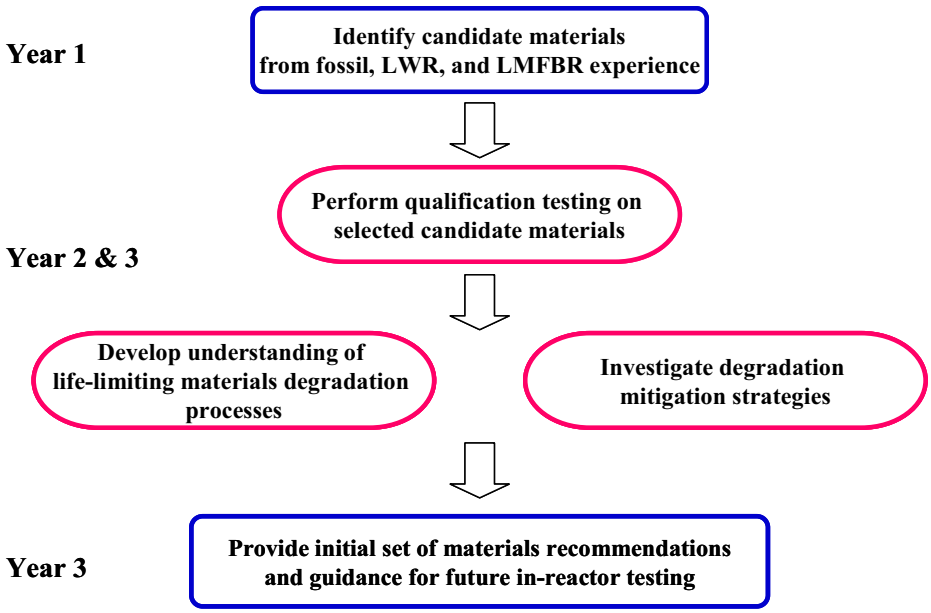

Figure 1 Chart of project objectives and research progress.

Research Progress

Highlights of Literature Survey

The literature survey was completed in the first half of year 1, and candidate materials were selected. As part of this effort, the areas where particular information gaps existed were identified in order to guide selection of the qualification test matrix.

Ferritic-martensitic (F-M) steels were chosen due to their extensive use in SCFP internals. In addition, one of the early generation ferritic alloys (HT-9) was tested extensively in the US LMFBR program and was shown to have extremely high swelling resistance. However, the creep strength of HT-9 is too low for application under SCWR conditions and thus it was not selected as a primary candidate alloy, although it was used in testing to establish baseline behavior on an alloy with well known radiation performance. F-M alloys were chosen as primary candidate alloys. Alloy Grade 91 frequent referred to asT91 or modified 9Cr has a nominal composition Fe-9Cr-MoVNb and has seen wide use in non-nuclear applications. Alloy HCM12A (Grade 122) sometimes referred to as T122 was developed for high creep resistance and has a nominal composition of 12Cr-MoVNbW, but has not yet seen extensive use in commercial SCFP. Both of these alloys are being considered as SCWR fuel cladding material; however, there is little or no data on their radiation behavior. Another alloy, NF616 (Grade 92), is a W modified version of grade 91 and also exhibits promising characteristics.

Results from the survey indicate that conventional 304 and 316 austenitic stainless steels may be highly susceptible to both swelling and stress corrosion cracking over the temperature range present in the SCWR environment. More advanced low-swelling alloys were developed for the LMFBR program. These alloys were optimized through the addition of stabilizing elements such as Ti and Nb in combination with thermomechanical treatments. The low swelling variants of austenitic stainless steels should also be considered as promising candidate alloys.

Superalloys have been developed for both thermal creep resistance and high corrosion resistance. Two of these alloys were selected as candidate alloys. Alloy 690 is a Ni-base superalloy developed for chemical processing and high-temperature aerospace applications. Alloy 800H is a high Ni and high Cr Fe-based alloy developed for chemical and petrochemical processing and is code qualified for nuclear applications. The major concern with higher Ni alloys is that earlier studies indicate they may be susceptible to grain boundary embrittlement during irradiation.

Although F-M alloys are highly resistant to radiation-induced swelling, one of their major limitations is low creep strength at temperatures above ~600°C. This problem has been addressed by the addition of dispersions of hard oxide particles to the material through mechanical alloying. The resulting oxide dispersion strengthened (ODS) material exhibits significantly higher creep strength than conventional ferritic alloys. The ODS alloys may be ideally suited for cladding applications, although the alloys are still in the early stages of development.

Highlights of Candidate Material Qualification Testing

The qualifications tasks involved testing in several key areas where potential materials properties limitations may be encountered and were designed to understand the major challenges posed by the SCWR environment. The major task areas included high temperature creep and tensile properties, corrosion and stress corrosion cracking behavior and radiation stability. At the suggestion of the annual reviewers, rather than perform a detailed study on the weldability of candidate alloys as was initially proposed, it was decided to focus more on the performance of welded samples in the SCW environment. The project initially had an aggressively broad workscope, with plans to test a variety of alloys within

several alloy classes. In order to complement GEN IV SCWR materials research activities and avoid duplication, the work scope was narrowed to focus primarily on ferritic-martensitic (F-M) alloys, while widening the range of qualification tests employed within the F-M alloy class. The following sections are separated by task and highlight the specific activities conducted and important results obtained.

High Temperature Tensile and Creep Behavior

Mechanical properties studies were conducted to ensure the candidate materials maintain adequate strength under service and accident conditions. The test focused on the F-M and ODS steels being considered for use as fuel cladding in the SCWR. Fuel cladding will be subject to thermal transients in loss of cooling feedwater off-normal events. The transient involves rapid heating and cooling from the operating temp to ~810-850°C. Because the maximum transient temperature lies near or above the equilibrium austenite transformation temperature for many of these steels (A_{e1} temperature), it has the potential to severely alter their microstructure and properties, either by formation of new untempered martensite or overtempering of the existing structure.

In order to evaluate the effects of the projected transient on the microstructure and properties of F-M steels, two representative alloys—modified 9Cr-1Mo-V (ASME Grade 91 steel) and HCM12A (ASME Grade 122 steel)—were subjected to the transient thermal cycle using a Gleeble thermal weld simulator, and the microstructures, tensile properties, and creep properties of the cycled alloys were assessed. Different combinations of maximum transient temperature and number of transient cycles were first evaluated and specimens were examined that had been cycled once, 5 times, and 10 times, to maximum temperatures of 810°C (reference transient temperature) and 845°C (limit transient temperature). These short term cyclic transients did not appear to significantly affect properties.

To determine off-normal thermal cycle conditions that could cause an appreciable change in the microstructure of mod. 9Cr-1Mo (Grade 91) specimen, the effects of the maximum temperature in the cycle and the hold time at 840°C (10 to 30 min) on the microstructure and hardness was investigated. Marked increase in hardness was found when the maximum cycle temperature increased from 860 to 870°C. The hardness increased after 10 sec at 840°C.

Thermal aging studies on commercially available 20 Cr oxide dispersion strengthened (ODS) alloys were also conducted. These studies revealed substantial loss of ductility in the alloys following even short term exposure at temperatures relevant to the SCWR (400 – 500°C). Because of the substantial embrittlement behavior of the commercial alloys, a small effort was initiated near the end of the project to fabricate and test experimental ODS alloys with better properties.

Finally, as part of efforts to further establish high temperature behavior of the F-M alloys thermal properties for T91 (a 9% Cr alloy) and HCM12A (a 12% Cr alloy) were investigated. Two methods available at Idaho National Laboratory's (INL's) High Temperature Test Laboratory (HTTL) were applied to estimate thermal diffusivity, thermal conductivity, and specific heat capacity. Results were compared with data in the literature and with data for other metals typically found in Light Water Reactor (LWR) vessels, SS304 and SA533B1.

Corrosion and Stress-Corrosion Cracking

The project has obtained substantial amount of corrosion and stress corrosion cracking (SCC) data. Three separate supercritical water corrosion and two separate SCC facilities were utilized for evaluating and qualifying the candidate alloys. As mentioned in the overview, the focus has been on testing candidate F-M alloys to complement corrosion studies being conducted as part of the GEN IV SCWR initiative investigating a broader range of alloys including Ni-based and austenitic stainless steels.

The corrosion tests were conducted in supercritical water in the temperature range 350 to 600°C in both deaerated and non-deaerated water having various oxygen levels up to ~3000 ppb. Samples were also SCC tested following exposure to high energy protons to emulate radiation damage that will be encountered in service. Overall, alloy HCM12A (12% Cr) oxidized less than T91 (9% Cr) in all environments. However, both these alloys had much greater rates of oxidation than austenitic stainless steels and high Ni alloys. F-M alloy samples exposed to 100 ppb oxygen had a lower rate of oxidation than in the deaerated case. The reason for the lower oxidation rate in the higher oxygen content supercritical water is believed to be the formation of a hematite (Fe_2O_3) layer in addition to magnetite (Fe_3O_4) that promotes a dense less permeable surface oxide thereby reducing corrosion. Tests conducted on the irradiated samples revealed the F-M alloys are highly resistant to SCC even following irradiation. The results of these experiments indicate that, as with currently operating light water reactors and fossil plants, controlling water chemistry can be critical to minimizing internals degradation due to corrosion and stress corrosion cracking.

In another series of experiments, the corrosion and SCC susceptibility of alloys was tested following plasma source ion implantation. Results obtained indicate that such surface modification can result in a lower rate of surface oxidation (as measured by weight gain) during long term exposure tests. Detailed analysis to elucidate the mechanism of such changes in corrosion behavior revealed changes in formation morphology of the oxide on surface of the implanted alloys vs. the un-implanted alloys. Such changes were measured by examining the samples using electron backscatter diffraction (EBSD) in the scanning electron microscope to identify the spatial distribution of oxide phases forming on the surface of the alloys during exposure.

Radiation Stability

The potential impact of in-core radiation damage on candidate alloys was evaluated. Alloys with a limited radiation damage database were selected for heavy-ion irradiation damage studies. The 12 chromium F-M alloy HCM12A and the austenitic alloy 800H were irradiated with heavy-ions (Ni^{++}) at 500°C to doses of 5 and 50 displacements per atom (dpa). The microstructures of the alloys were examined with transmission electron microscopy (TEM) following irradiation. Neither alloy exhibited void formation up to a dose of 50 dpa. The radiation damage in the HCM12A alloy manifested itself as an increase in the density of network dislocations, while the radiation damage in the 800H alloy generated a high density of faulted dislocation loops. At the higher dose, a population of extremely small precipitates also formed in alloy 800H and the dislocation loop structure was refined. The refinement of the dislocation structure is thought to be associated with the small precipitates acting as sinks for the point defects generated from the displacement damage.

F-M alloys T91 and HCM12A samples irradiated to 7 dpa using 2 MeV protons at 400°C were also characterized using transmission electron microscopy. The microstructure of the irradiated alloy T91 contained dislocation loops, black dot damage and precipitates, while, in addition to these features, alloy HCM12A contained a population of voids in the material. In addition to the microstructural analysis, grain boundary chemistry measurements were conducted on alloy T91. These measurements indicate strong enrichment of chromium and depletion of iron at the grain boundary.

An ODS alloy irradiated with heavy-ions showed even stronger resistance to radiation damage than the F-M alloys as evidenced by lower swelling compared to a F-M alloy irradiated under the same conditions.

Weldability/Joining

Ferritic-Martensitic (F-M) alloys Grade 91 and HCM12A plates were joined by GTAW (Gas-Tungsten-Arc-Weld) at Idaho Nation laboratory. To avoid cracking of the weld and to attain adequate strength and ductility, pre- and post-weld heat treatments were performed. The plates were then machined across the weld into SCC bar and coupons. The samples were then sent to the Universities of Wisconsin and Michigan for corrosion and SCC testing.

Irradiation Testing Recommendations

Existing irradiated materials such as those irradiated as part of the fusion and/or fast breeder reactor programs should be considered for testing in supercritical water as a first step in future testing campaigns. This will serve two purposes, 1) develop a methodology for testing of irradiated components in SC water and 2) provide some initial lower cost data to guide, more in depth testing campaigns. In the absence of in-pile SCW testing capabilities, a variety of specimens including tensile, creep, fracture toughness and microstructure should be irradiated over the range of temperatures relevant to the SCWR (300-600°C) in one of the available test reactors such as ATR or HFIR. Post-irradiation testing of the irradiated materials in SC water can then be conducted to ensure that irradiation under conditions relevant to the SCWR do not lead to excessive swelling, embrittlement or loss of high temperature creep strength. In order to save cost, such irradiations can be joined with current irradiation testing programs planned for either the Advanced Fuel Cycle Initiative or combined with other GEN IV materials irradiation programs where irradiation conditions are compatible.

CONTENTS

FIGURES

TABLES

Developing and Evaluating Candidate Materials for Generation IV Supercritical Water Reactors

1. Task 1 - Literature Survey

Contributors:

James Cole, Joy Rempe and Terry Totemeier, INL
Todd Allen and Kumar Sridharan, U. W.
Gary Was, U. M.
Jinsung Jang, KAERI

1.1 Task Summary

In this phase of the project, a literature survey was conducted to identify the most promising candidate alloys for further testing and analysis. Information resources that were evaluated include supercritical fossil plant and other non-nuclear experience and experience gained in various DOE nuclear breeder and fusion reactor programs. The literature survey was conducted to ensure the selection of candidate alloys with the greatest potential and to minimize duplication of testing. Nearly 200 references were reviewed for the literature survey.

1.2 Highlights of Literature Survey

In the early stages of planning of the project, it was determined to limit the scope of the survey to specific issues that were perceived as the most critical for qualifying candidate materials. These issues were determined as:.

- High temperature tensile and creep
- Corrosion and stress corrosion cracking
- Radiation stability
- Weldability/Joining

In addition to the literature reviews conducted as part of this program, collaborators also considered literature reviews being conducted under the Generation IV SCWR R&D program.

Table 1 lists potential candidate materials for SCWR reactor core internals for which qualification tests will be conducted. Perceived advantages and disadvantages of each of the alloy classes are also cited.

The excessive swelling and poor cracking resistance of commercial 304 stainless steels under high temperature irradiation essentially eliminates it from consideration for SCWR applications. For a thermal reactor with components that receive lifetime doses less than ~50 dpa, cold worked 316 SS may be adequate from a swelling perspective. However, early tests on conventional 316 SS indicate that it is susceptible to stress corrosion cracking under SC water conditions thus eliminating it from consideration in this testing program. In applications where swelling resistance is paramount, the Ti-modified stainless steel alloys have shown no significant swelling up to dose levels of 100 dpa. Research on radiation resistant SS for the DOE-NE NERI program indicate the IASCC resistance of

austenitic stainless steels is enhanced optimally with oversized Zr solute additions and grain boundary structure modifications. Testing of this alloy under SC water conditions would further indicate the

Table 1 Candidate alloy list.

Alloy Class	Alloy	Advantages	Limitations
Ferritic-Martensitic			
	T91- Fe-9Cr-MoVNb	Low swelling	Corrosion, high temperature creep strength, low temperature radiation embrittlement
	HCM12A (T122)- Fe-12Cr-MoVNbW	Low swelling	Corrosion, high temperature creep strength, low temperature radiation embrittlement, neutronics
Austenitic Stainless Steels			
	Alloy D-9- Ti–Modified Fe-15Cr-15Ni-2.2Mo	Corrosion resistance, High temperature creep strength.	Low thermal conductivity, susceptibility to irradiation assisted stress corrosion cracking.
High Ni alloys			
	Alloy 690 Ni-30Cr-10Fe	High temperature creep and corrosion resistance	Irradiation-induced grain boundary embrittlement.
	Alloy 800H Fe-32Ni-20Cr-TiAl	High temperature creep and corrosion resistance	Irradiation-induced grain boundary embrittlement.
ODS			
	MA957 Fe-14Cr-Mo +0.25$Y_2 0_3$	High temperature creep strength, swelling resistance	Corrosion, low temperature radiation embrittlement.

effectiveness of these modifications on improving alloy resistance to IASCC. Although these alloys show promise, they are in the early stages of development and in order to limit the total number of alloys tested, weren't evaluated in this project.

Over 100 references were reviewed to investigate two alloy classes: high-chromium ferritic-martensitic (F-M) steels, and iron-based oxide dispersion strengthened (ODS) alloys. In addition to basic high-temperature properties, information was gathered on other issues relevant to the application of these alloys in the SCWR, namely anisotropy, joining, irradiation embrittlement, and the effects of thermal transients during off-normal events.

Alloys with strengths suitable for use in normal SCWR operating conditions are available in both classes. With respect to off-normal conditions, no data on the properties of F-M steels at temperatures above 700°C were found, while data on the ODS alloys were available for temperatures up to 1100°C. Issues of concern identified for the F-M steels were the extremely poor strength expected at temperatures above 700°C and the potential weakening resulting from exposure to temperature transients greater than 800°C. For the ODS alloys, the primary issues identified were the extreme anisotropy of properties in the annealed, coarse-grained condition (in particular the poor hoop strength of tubes), the lack of well-qualified joining techniques, and the potential for embrittlement due to alpha-prime precipitation during irradiation at temperatures less than 500°C.

Finally, the literature survey revealed that there are very little data on the irradiation and corrosion and stress corrosion cracking behavior of high-nickel superalloys in supercritical water. The limited data that are available suggest that high-nickel alloys may be susceptible to grain boundary embrittlement above 500°C when exposed to irradiation.

2. Task 2 - High Temperature Mechanical and Physical Properties of Candidate Alloys

2.1 Task Summary

Mechanical and physical properties were charted for the candidate alloys over a range of temperatures and test conditions to ensure the candidate materials maintain adequate properties under service and accident conditions. These tests were conducted for relevant materials and test conditions where a lack of properties property data currently exists.

In order to complement other work being conducted as part of the GEN IV SCWR program, this effort focused primarily on F-M alloys. Commercially available F-M and Fe-based ODS alloys were examined. Where possible, the same heats of materials were used across a series of tests. Compositions of the alloys used in the following studies are listed in Table 2 and Table 3 for the F-M and ODS alloys respectively.

Table 2 Chemical Composition (wt%) of F-M alloys.

Alloy	Fe	C	Cr	Mo	V	Cu	W	Ni	Mn	Si	Al	Nb	N	P	S
Grade 91															
Heat 1 (Reference Cycles)	Bal.	0.10	8.34	0.90	0.22	0.17	--	0.21	0.45	0.28	0.022	0.076	0.048	0.009	0.003
Heat 2 (Varied Cycles)	Bal.	0.10	8.70	0.90	0.21	0.28	--	0.18	0.33	0.27	0.005	0.074	0.042	0.012	0.004
Grade 122	Bal.	0.11	10.83	0.30	0.19	1.02	1.89	0.39	0.64	0.27	0.001	0.054	0.063	0.016	0.002

Table 3 Chemical compositions of MA956 and PM2000 alloy

Alloy		Chemical Composition(wt%)						Processing Condition	Size, mm/ Shape
		Fe	Cr	Al	Ti	Y_2O_3	Others		
MA 956	Rod	Bal.	19.4	4.8	0.4	0.5	0.015C	1330°C, 1h annealed, AC	25ϕ Rod
	Tube	Bal.	19.8	4.7	0.4	0.5	0.018C	Cold drawn and annealed	44.5OD × 2.34t Tube
PM 2000	As-rolled Plate	Bal.	20	5.5	0.5	0.5	-	As-rolled	1.7t Plate
	As-forged Bar	〃	〃	〃	〃	〃	-	81.8% Warm-deformed	162Φ Bar
	Forged and Recrystallized Bar	〃	〃	〃	〃	〃	-	93.07%, 97.5%, 99.94% Warm-deformed and recrystallized	100 Φ 60 Φ 9 Φ Bar
	Extruded and Recrystallized Tube	〃	〃	〃	〃	〃	-	Warm-deformed and recrystallized	33.7 Φ ×2t Tube

2.2 High-Temperature Tensile Testing of HCM12A (T122)

Contributors:

Terry Totemeier, Joy Rempe, INL

High-temperature tensile tests were performed on specimens of HCM12A (T122) ferritic-martensitic steel to better predict material response under SCWR off-normal and accident conditions. The tensile strength and ductility of HCM12A (T122) as a function of test temperature are shown in Figure 2 and Figure 3. Both the yield and ultimate tensile strength dramatically decrease between 600 and 800°C. Less decrease is observed above 800°C, although the magnitude of the strength is very low, less than 100 MPa. Both ductility parameters generally increase with test temperature, although a slight reduction is observed at 1000°C relative to 900°C.

The tensile behavior observed at room temperature and 600°C agree well with data reported in the literature for this alloy [2]. The dramatic decrease in strength with temperature above 600°C is expected, resulting from carbide coarsening and increased dislocation climb. At the two highest test temperatures, the alloy is in the austenite phase field and only solid solution strengthening mechanisms are effective. At all temperatures above 600°C, the strength will be very strain-rate dependent due to creep effects. The strain rate chosen is typical for tensile tests. Higher strengths would be obtained for higher strain rates, and vice versa for lower strain rates.

The tensile strengths of HCM12A (T122) at very elevated temperature compare favorably with those of annealed 304 SS. High-temperature tensile data (temperatures up to 1100°C) were reported by Korth, et al. [2]. 304 maintains a slight strength advantage to ~850°C, but its tensile strength decreases to 82 MPa at 927°C and 40 MPa at 977°C, lower than HCM12A (T122). The strengths of both steels, however, are considerably less than that of oxide-dispersion strengthened alloys. The tensile strength of annealed MA956 at 800°C is approximately 150 MPa, decreasing to 120 MPa at 1100°C. The ductility of MA956 at these temperatures is relatively low with less than 10% tensile elongation [3].

The time at temperature prior to testing also plays a strong role in determining the behavior of HCM12A (T122), as the initial, heat-treated microstructure is unstable at elevated temperatures, especially 800°C and above. Longer holds prior to testing will result in greater carbide coarsening and dissolution, and commensurately lower strength. The duration chosen (15 minutes) represents a compromise between obtaining some degree of thermal equilibrium

The elastic modulus (Figure 4) clearly decreases from 25°C to 800°C, as expected. There is considerable scatter in the modulus data for 900 and 1000°C, likely resulting from the low loads and strains in the elastic region at these temperatures. Given the scatter and the apparent increase in modulus, these data are not considered reliable. A discontinuity in modulus might be expected, however, due to the transformation of the low-temperature ferrite structure to the high-temperature austenite structure.

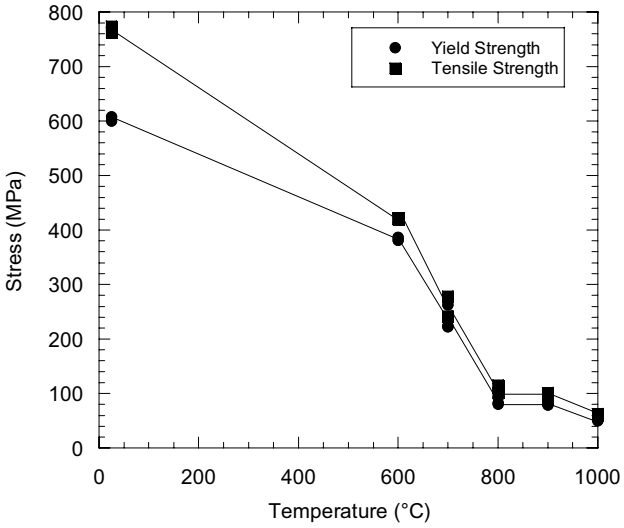

Figure 2 HCM12A (T122) elevated temperature tensile strength.

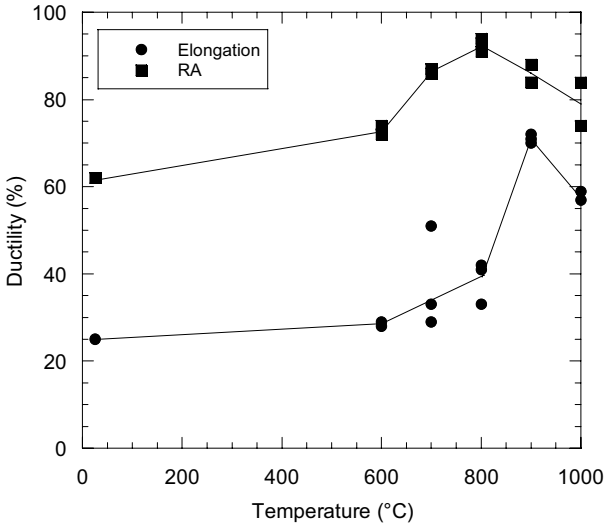

Figure 3 HCM12A (T122) elevated temperature tensile ductility.

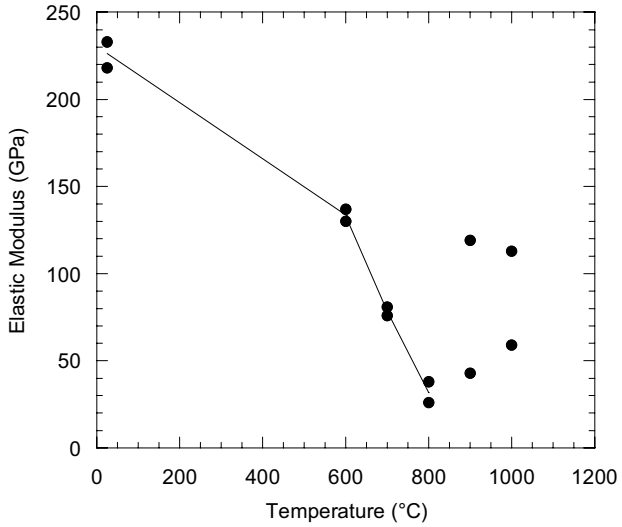

Figure 4 HCM12A (T122) Elevated temperature elastic modulus.

2.2.1 References

1. K. Miyata, et al., ISIJ International, vol. 40 (2000), p.1156.

2. J. L. Rempe, et al., *Light Water Reactor Lower Head Failure Analysis*, NUREG/CR-5642, 1993.

3. W.F. Brown, Jr., et al., eds. *Aerospace Structural Metals Handbook* (CINDAS, West Lafayette, IN), 1997.

2.3 Effect of Thermal Cycling on Microstructure and Properties of Ferritic-Martensitic Steels

Contributors:

Terry Totemeier, Joy Rempe, INL

2.3.1 Overview

Ferritic-martensitic steels are being considered for use as fuel cladding in the SCWR. The fuel cladding will be subject to thermal transients in loss of cooling feedwater off-normal events. The transient involves rapid heating and cooling from the operating temp to ~810-850°C; a plot of projected fuel cladding temperature during the transient is shown in Figure 5. Because the maximum transient temperature lies near or above the equilibrium austenite transformation temperature for these steels (A_{e1} temperature), it has the potential to severely alter their microstructure and properties, either by formation of new untempered martensite or overtempering of the existing structure. Untempered martensite will form if transformation to austenite occurs during the transient, which will re-transform to martensite during the rapid cool-down following the transient. Even if the transient temperature does not result in martensite formation, exposure of the existing tempered martensite structure to temperatures exceeding the normal tempering temperature (760°C) will result in overtempering and a resulting loss in creep strength. Both austenite formation and overtempering are diffusion-limited processes, however, so the time scale of the transient will be critical in determining its effect. The extremely short duration of the projected transient suggests that the effects may be minimal.

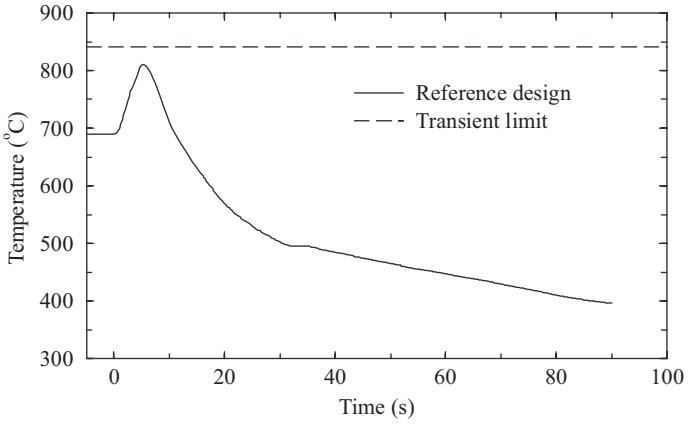

Figure 5 Projected fuel cladding temperature in a SCWR off-normal event.

In order to evaluate the effects of the projected transient on the microstructure and properties of ferritic-martensitic steels, two representative alloys—modified 9Cr-1Mo-V (ASME Grade 91 steel) and HCM12A (ASME Grade 122 steel)—were subjected to the transient thermal cycle using a Gleeble thermal weld simulator, and the microstructures, tensile properties, and creep properties of the cycled alloys were assessed.

2.3.2 Experimental Procedures

2.3.2.1 Thermal Cycling and Test Procedure

A Gleeble thermal simulator was used to subject the thermal transient cycle to cylindrical specimens 10 mm in diameter and 107 mm long. Different combinations of maximum transient

temperature and number of transient cycles were first evaluated by microstructural analysis and hardness measurements; specimens were examined that had been cycled once, 5 times, and 10 times, to maximum temperatures of 810°C (reference transient temperature) and 845°C (limit transient temperature). For creep-rupture testing, two cycle conditions were evaluated: 5 cycles at 810°C and 5 cycles at 845°C. Most creep-rupture tests were performed on specimens that had been cycled to 810°C.

Room-temperature tensile tests were performed on baseline material and specimens that had received five thermal cycles to 810°C. Creep-rupture tests were performed on thermally-cycled material over a wide range of conditions: temperatures varying from 550°C to 650°C and stresses ranging from 100 to 300 MPa. Creep-rupture tests were performed in air using standard lever-arm load frames with averaging, axial extensometers. Test temperatures were controlled to within ±5°C. Nearly all creep-rupture tests were run to failure.

In the second part of the study a wider range of thermal transient conditions were studied in order to identify transient parameters which resulted in significant microstructural changes for the Grade 91 steel. Specimen blanks were subjected to a series of transient cycles with peak temperatures ranging from 860 to 960°C and a series of transient cycles with a temperature hold at 840°C which ranged from 10 to 1800 s. In both series the transient heating and cooling rates were 24°C/s. Specimen blanks were only subjected to a single transient cycle in the second part of the study.

2.3.2.2 Transformation Temperature Measurement

Phase transformation temperatures in the two steels (Grade 91 heat 2) were measured using a Theta Industries (Port Washington, NY) vertical differential dilatometer. Cylindrical specimens 12 mm in length and 3 mm in diameter were heated to 1050 °C in rough vacuum; a Pt standard with the same dimensions was used as the reference. Transformation temperatures were measured at a standard rate of 0.05 °C/s and a rapid rate of 0.8 °C/s. The rapid rate was the closest simulation of the transient heating rate, the maximum available from the dilatometry equipment. The ferrite-to-austenite transformation temperature A_{c1} was determined from the dilation curves using the technique described in [1]. For Grade 91 steel the A_{c1} temperatures at the slow and fast heating rates were 827 and 842 °C respectively while for Grade 122 steel, they were 811 and 841 °C.

2.3.2.3 Microstructure and Mechanical Property Evaluation

Microstructures after thermal transient cycling were evaluated using optical and scanning electron microscopy (SEM). Metallographic cross-sections were prepared using standard techniques and immersion etched using either Vilella's reagent or a solution of 30 ml ethanol, 3 g picric acid, 0.6 ml nitric acid, and 1 ml hydrochloric acid. The latter etch was used to reveal carbide precipitates in SEM examination. Carbide size distributions were measured from SEM images of etched sections taken at high magnification (20 to 40 kX). Figure 6 contains a typical image and a plot illustrating representative size distributions.

Multiple Vickers microhardness measurements with a 500 g load were taken in the center of the heated zone and in an unaffected region of the blank to determine the effect of transient cycling on hardness. Tensile tests were performed at room temperature and creep-rupture tests were performed at 550, 600, and 650 °C. Creep-rupture tests were performed using standard lever-arm machines with averaging, rod-in-tube type extensometers; tests were generally performed to specimen failure. Broken specimens were optically examined for anomalous failure features; none were observed.

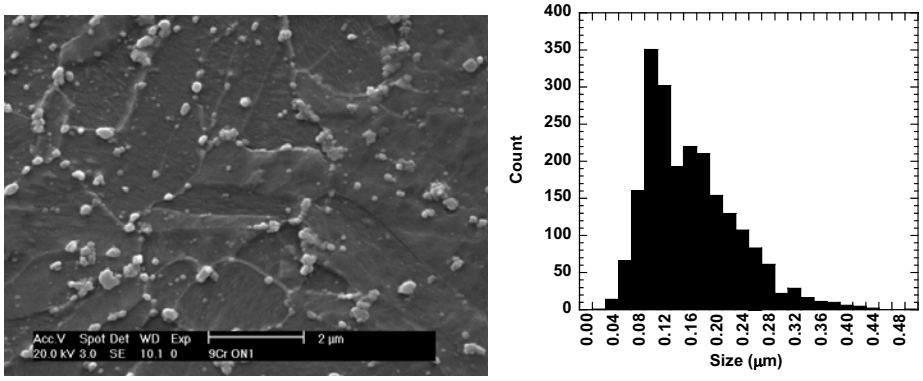

Figure 6 Typical SEM image of etched microstructure and resulting carbide size distribution.

2.3.3 Results

2.3.3.1 Effect of Cycling on Microstructure, Hardness, and Room-Temperature Tensile Properties

Essentially no effect of the thermal cycle at either temperature was observed. The structure of both alloys after cycling consisted of tempered martensite indistinguishable from the baseline structure. No areas of untempered martensite were observed. Figure 7 and Figure 8 are a comparison of typical baseline and cycled microstructures for T91 and HCM12A respectively. Table 4 summarizes the precipitate size distribution and microhardness results. A small, but statistically significant, increase in mean carbide precipitate diameter was observed for 9Cr-1MoVNb after thermal cycling. As expected, the mean diameter was higher for the 845°C transient temperature. In contrast, no significant changes in mean carbide diameter were observed for HCM12A.

Table 4 Effect of thermal transient on mean carbide diameter and microhardness.

Condition	Mean Carbide Diameter ± 95% Confidence Interval (nm)	Mean Microhardness ± 95% Confidence Interval (HV_{500})
9Cr-1MoVNb		
Baseline	101 ± 6	225 ± 5
5 cycles @ 810°C	128 ± 6	222 ± 2
5 cycles @ 845°C	143 ± 8	228 ± 2
HCM12A		
Baseline	138 ± 8	247 ± 2
5 cycles @ 810°C	143 ± 10	241 ± 2
5 cycles @ 845°C	140 ± 8	238 ± 3

The changes in hardness were also slight. No statistically significant change was observed for 9Cr-1MoVNb; but a small, barely significant decrease in microhardness was observed for HCM12A. The change in Rockwell C-scale macrohardness with cycling was evaluated for 9Cr-1MoVNb to provide a cross-check to the microhardness measurements; the hardness decreased a small amount (from a baseline of 20 HRC to 17.5 HRC) after cycling to 845°C. Room temperature tensile test results are listed in. Changes in tensile properties were somewhat more marked; 20-30 MPa decreases in yield and tensile strengths were observed for both alloys after cycling at 810°C. No changes in ductility were observed.

The effects of varied maximum transient temperature and hold time at 840°C transient temperature on the microhardness of Grade 91 steel are shown in Figure 9a and Figure 9b,

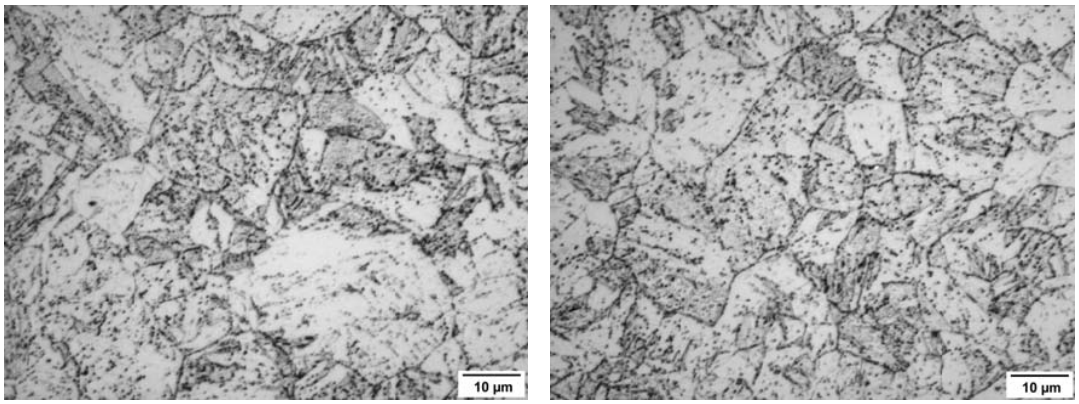

(a) (b)

Figure 7 Optical microstructure of Grade 91 steel (heat 1): (a) baseline prior to cycling, (b) after five transient cycles to 840 °C maximum temperature.

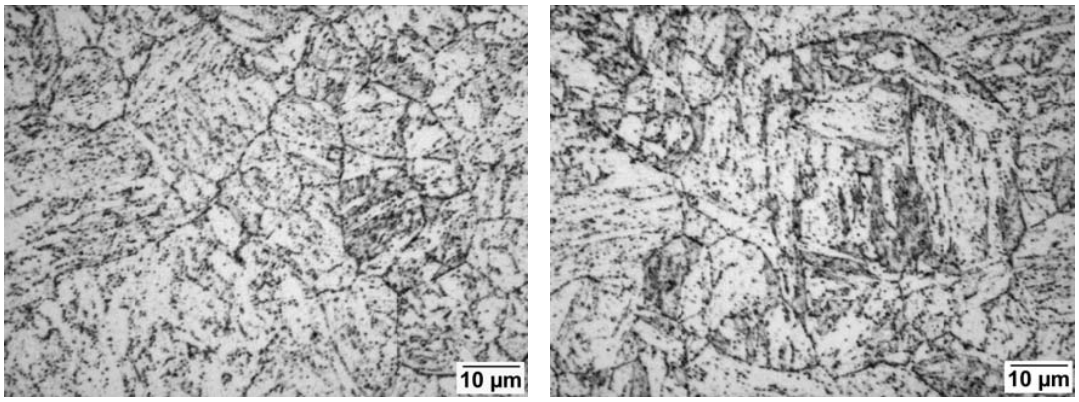

(a) (b)

Figure 8 Optical microstructure of Grade 122 steel: (a) baseline prior to cycling, (b) after five transient cycles to 840 °C maximum temperature.

Table 5 Effect of thermal transient on tensile properties.

Condition	Yield Strength (MPa)	Ultimate Tensile Strength (MPa)	Ductility (%)	Reduction in Area (%)
9Cr-1MoVNb				
Baseline	581	735	27	70
5 cycles @ 810°C	562	727	27	70
HCM12A				
Baseline	644	808	25	58
5 cycles @ 810°C	610	780	24	60

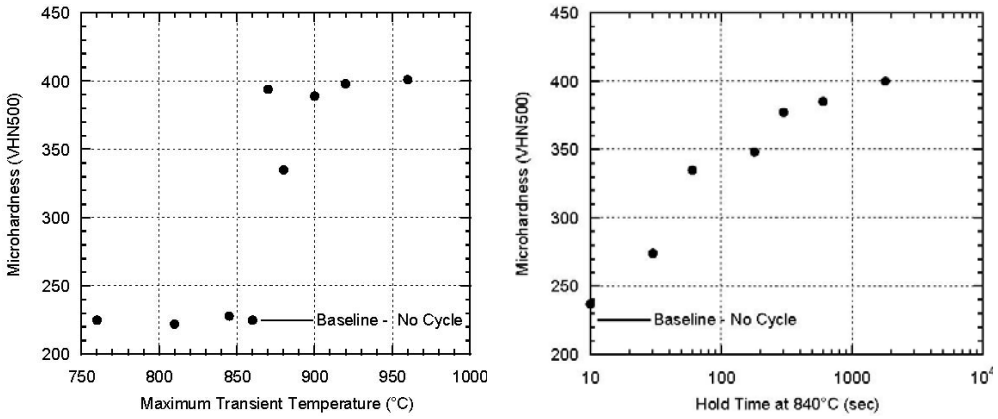

Figure 9 Variation of Grade 91 (heat 2) post-transient microhardness with (a) maximum transient temperature without hold, (b) hold time at 840 °C maximum transient temperature.

respectively. Also indicated are the pre-cycling baseline hardness values. No change in microhardness was observed for maximum cycle temperatures of 860°C and below; for transient temperatures above 860°C the microhardness dramatically increased to a plateau level of 400 VHN_{500}. Hold periods at 840°C greater than 10 s resulted in microhardness that increased with hold duration; a maximum microhardness of 400 VHN_{500} was observed after 1800 s holding at 840°C. Etched optical microstructures observed after cycling reflected the microhardness changes; significant fractions of untempered martensite were observed for maximum transient temperatures of 870°C and above and 840 °C hold periods greater than 10 s. Typical baseline and cycled structures are shown in Figure 10; lightly etched areas in the cycled microstructures are untempered martensite.

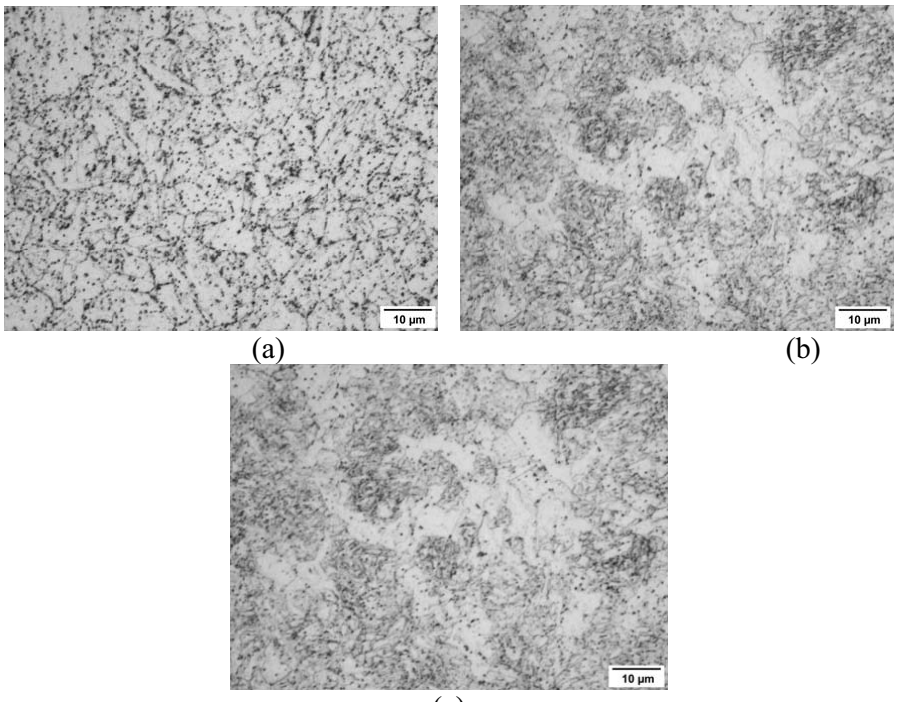

Figure 10 Optical microstructure of Grade 91 steel (heat 2): (a) baseline prior to cycling, (b) 870°C maximum transient temperature, (c) 30 s hold time at 840°C maximum transient temperature.

2.3.3.2 *Effect of Cycling on Creep-Rupture Properties*

Figure 11 shows a comparison of minimum creep rates and rupture lives for thermally-cycled Grade 91 steel to those obtained for the same alloy in a standard heat treatment condition. Minimum creep rates and rupture lives are indistinguishable from baseline and literature data over a wide range of temperatures and stresses. Specimens which were cycled to 870 °C maximum temperature or with a 30 s hold at 840°C show dramatically lowered creep strength, slightly greater than a factor of 10 in either minimum creep rate or rupture life at the condition tested, 600°C and 145 MPa.

Figure 12 compares rupture life data for cycled Grade 122 steel with literature data—again there is apparently no effect of repeated transients at either 810 or 840°C. Creep ductilities for both alloys (not shown) after thermal cycling are not different than in a standard heat treatment condition, with typical failure elongations of 25-30% for Grade 91 and 15-20% for Grade 122.

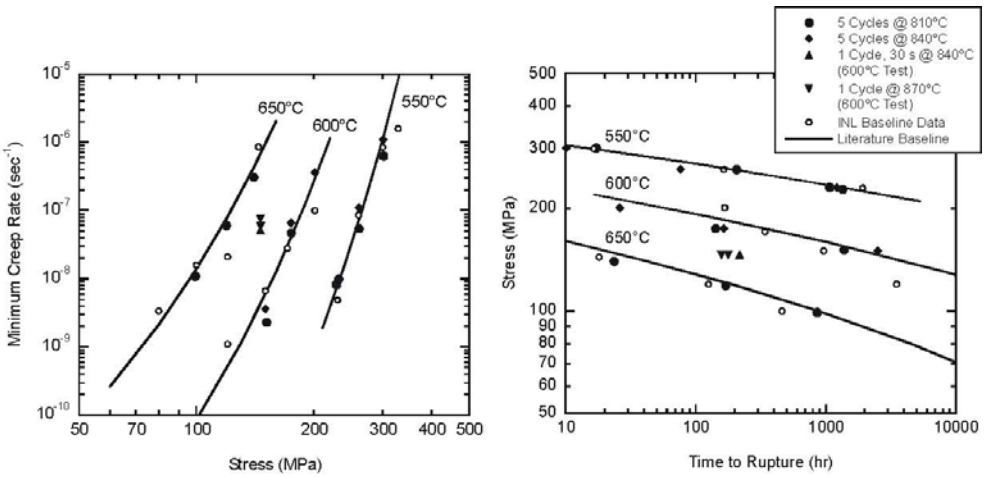

(a) (b)

Figure 11 Comparison of (a) minimum creep rate and (b) rupture life for transient-cycled Grade 91 steel with baseline data.

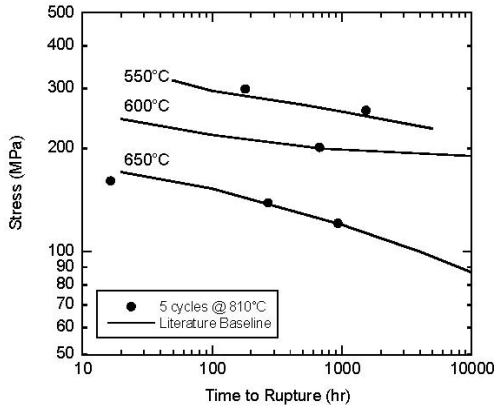

Figure 12 Comparison of rupture life for Grade 122 steel after transient cycling with lines representing baseline data from reference [4].

2.3.4 Discussion of Transient Studies Results

The results obtained demonstrate that thermal cycling to either 810 or 845°C has a negligible effect on the microstructure and properties of 9Cr-1MoVNb and HCM12A steels. The slight changes observed in mean carbide diameter, hardness, and room temperature tensile strength are consistent with a small degree of overtempering with no evidence for martensitic transformation, consistent with the short duration of the transient. The overtempering has no detrimental effect on creep properties for the conditions of interest; in fact, an apparent improvement in creep strength was observed after cycling at 845°C.

These observations are consistent with the maximum transient temperatures, the rapid heating and cooling rates, and the short transient durations. The 810 and 840 °C maximum transient temperatures do not exceed the A_{c1} temperatures measured for either steel at a heating rate of 0.8 °C/s, which were 842 and 841 °C for Grade 91 and Grade 122, respectively. Since the transient heating rate is considerably greater at 24 °C/s, the transformation temperature during the transient will be even higher than those measured (A_{c1} increases with heating rate [1]). The observation of a dramatic increase in hardness for Grade 91 steel when the maximum transient temperature was increased from 860 to 870 °C indicates that A_{c1} for a heating rate of 24 °C/s lies between these two temperatures. Such an increase is consistent with that observed when the heating rate was increased from 0.05 °C/s to 0.8 °C/s. In this case a 16 X increase in heating rate resulted in a 15 °C increase in A_{c1}. The 30 X increase in heating rate from 0.8 to 24 °C/s appears to result in a 20 °C increase in A_{c1}. Because the A_{c1} temperature for ferritic-martensitic steels is roughly proportional to the logarithm of the heating rates [1], these relative increases are consistent.

The very limited degree of overtempering observed due to the transient cycles at 810 and 840°C is due to the very short time above the standard 760°C tempering temperature during the transient; approximately 4 s for the 810 °C transient and 7 s for the 840 °C transient. Tempering is a diffusion-based process [5], and time at temperature is required—standard tempering times are greater than one hour, so it is not surprising that exposure times less than 10 s have little effect on a previously-tempered structure.

Observation of significantly increased hardness and untempered martensite in the microstructure of Grade 91 steel held at 840 °C for times greater than 10 s is also consistent with the measured transformation characteristics. Although A_{c1} for continuous heating at 24 °C/s is considerably greater than 840 °C (860-870 °C as indicated by the maximum transient temperature tests), 840 °C is greater than the equilibrium transformation temperature A_{e1}. The value of A_{c1} measured at the slow heating rate of 0.05 °C/s, 827 °C, can be taken as a reasonable approximation of A_{e1}. Therefore transformation to austenite will occur at 840 °C given sufficient holding time. The kinetics of the transformation are evident in the increasing hardness with hold duration at 840 °C with the transformation apparently complete at 1800 s (a microhardness equivalent to the plateau level in the maximum temperature transient tests was obtained).

In all cases the cooling rates to 100 °C following the transient were sufficient to produce fully martensitic structures in these air-hardening steels. Very slow cooling below A_{r1} (austenite-to-ferrite transformation temperature during cooling) and above the martensite start temperature would be required to produce ferritic rather than martensitic structures from austenite formed in the transient. Martensite start temperatures are between 350 and 400 °C for the two steels, so cooling to a reactor "warm standby" temperature of approximately 250 °C would result in the formation of untempered martensite [6].

The results of these studies confirm that both the "reference" transient cycle and cycles at the "limit" transient temperature will not be damaging to fuel cladding using either ferritic-martensitic steel. The safety margin is not great, however, as an increase of merely 20 °C above the current "limit" temperature would result in significant microstructural alteration and degradation of elevated

temperature strength, as will any small hold duration at the limit temperature (equivalently, "rounding" of the transient peak with significant time above A_{e1} will also cause transformation).

The limited creep-rupture tests performed on Grade 91 steel with microstructure altered by the transient show that the creep rate is increased and the rupture life decreased by an order of magnitude. These reductions were observed for the first transient conditions that caused an observable change—further increases in maximum temperature or hold time above A_{e1} may result in further strength reduction as the fraction of untempered martensite in the structure increases. These reductions are consistent with other studies of off-normal microstructures in ferritic-martensitic steels [7]—the major problem is that the fine distribution of carbide and carbonitride precipitates essential to the strength of ferritic-martensitic steels [8] is disrupted. The presence of untempered martensite is not only detrimental to elevated temperature creep strength but also low-temperature toughness [9], a characteristic that was not measured in this study.

Transient conditions which do not result in microstructural transformation and loss of strength for other ferritic-martensitic steels (or other heats of the steels studied), will be dependent on the specific transformation characteristics for the steel in question. In an ideal case, the maximum "off-normal" transient temperature would lie reasonably below the A_{e1} temperature for the cladding steel. An additional factor, which was not considered in this study, is the effect of radiation exposure on ferrite to austenite transformation kinetics of ferritic-martensitic steels. Fuel cladding will experience a high radiation dose over its lifetime, and the altered chemistry and stored energy of lattice defects resulting from the irradiation may significantly affect transformation temperatures and kinetics.

2.3.5 References:

1. C. Garcia de Andres, F.G. Caballero, C. Capdevila, L.F. Alvarez, Mater. Charact. 48 (2002) 101.
2. T.C. Totemeier, J.A. Simpson. In: 4th International Conference on Advances in Materials Technology for Fossil Power Plants. Hilton Head, SC: EPRI, 2004. p. 1269.
3. V.K. Sikka, M.G. Cowgill, B.W. Roberts, in: J.W. Davis, D.J. Michel (Eds.), Ferritic Alloys for Use in Nuclear Energy Technologies, TMS, Warrendale, PA, 1983, p. 413.
4. A. Iseda, Y. Sawaragi, S. Kato, F. Masuyama, in: Creep: Characterization, Damage and Life Assessments, ASM International, Materials Park, OH, 1992, p. 389.
5. G. Krauss, Steels: Heat Treatment and Processing Principles, ASM International, Materials Park, OH, 1990
6. J. Buongiorno, P. MacDonald, Supercritical Water Reactor (SCWR): Progress Report for the FY-03 Generation-IV R&D Activities for the Development of the SCWR in the U.S., Idaho National Engineering and Environmental Laboratory Report INEEL/EXT-03-01210, 2003.
7. M.J. Cohn, J.F. Henry, D. Nass, J. Press. Vess. - T. ASME 127 (2005) 197.
8. F. Abe, Mater. Sci. Eng. A387-389 (2004) 565.
9. G. Cai, H.-O. Andren, L.-E. Svensson, Metall. Mater. Trans. A 28A (1997) 1417.

2.4 Evaluation of Microstructure and Mechanical Properties of Commercial ODS Alloys

Contributors:

Jinsung Jang, KAERI

S. Hong, KAIST

2.4.1 Overview

Two commercially available ODS alloys, MA956 and PM2000 alloys, were obtained. The alloys are supplied by Special Metals(MA956) and Plansee GmbH(PM2000). Their essential features are highly oxidation resistant and extremely creep resistant ferritic Fe-Cr-Al based alloys containing 4.5~5.5%Al and 0.5%Y2O3. The aluminum enhances corrosion and oxidation resistance. The creep performance has been found to be optimum at Y_2O_3 content of approximately 0.5 wt%. Chemical compositions and processing conditions of the alloys were presented previously in Table 3.

2.4.2 Microstructure

Microstructures of as-received MA956 and PM2000 are observed by optical microscopy after polishing and etching with 15HCl+5HNO3+80C2H5OH solution. Their microstructures are shown in Figure 13. MA956 rod has highly elongated recrystallized grain and its GAR(Grain Aspect Ratio) is over 100. To compare grain boundary area between different samples, surface per unit volume(Sv, mm-1) are introduced. Given the columnar grain structure, the surface per unit volume of recrystallized grain boundary is measured according to Bhadeshia et. al. [1]. Thus, the columnar grains are approximated as space filling hexagonal prisms of cross-sectional side length a and height c, where c>>a. The recrystallized microstructure in MA ODS alloys are anisotropic because the grain growth rate is much higher along the extrusion direction, the final recrystallized grains can be also approximated as space filling hexagonal prisms. Table 6 shows surface per unit volume and GAR for each specimen. In recrystallized condition like MA956 rod, the grain shape tends to become more elongated; and surface per unit volume decrease.

(a) (b) (c)

Figure 13 Optical microstructure of as-received (a) MA956 rod, (b) tube and (c) PM2000 plate.

From TEM micrographs shown in Figure 14, the size distributions of oxide particles in MA956 and PM2000 are analyzed as shown in Figure 15. The size distributions of the two different alloys are very similar and average dispersoid size is measured 20nm. Recrystallized MA956 rod shows very low dislocation density within the grains. But, in case

of PM2000 tube, it shows small grains with high dislocation density caused by heavy deformation.

Table 6 Microstructure analysis of as-received MA956 and PM2000 alloy.

	MA956 Rod	MA956 Tube	PM2000 Plate
GAR	> 100(Max.=44)	~10	~10
SV(mm-1)	< 0.16	13	50

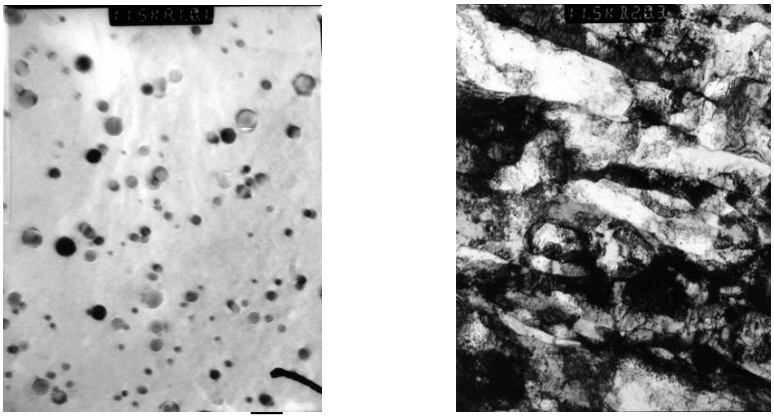

(a) (b)

Figure 14 TEM micrograph of (a) MA956 rod and (b) PM2000 plate.

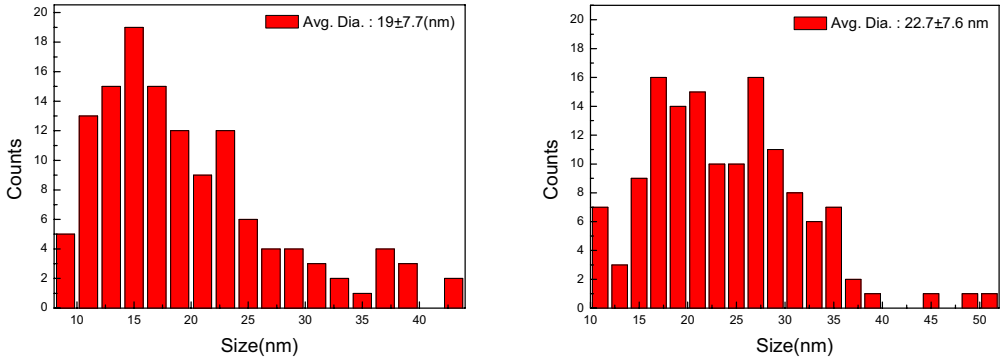

(a) (b)

Figure 15 Oxide distribution of (a) MA956 rod and (b) PM2000 plate.

Tensile properties of PM2000 alloy were measured at room temperature and high temperature by using ASTM E-8 subsize specimens. Specimens were wire-cut in the longitudinal direction from as-received plate. Tensile tests were performed at R.T., 500°C, 550°C, 600°C, 700°C, and 800°C with a crosshead speed of 0.5mm/min using Instron 4206 machine. Specimens were kept isothermally at the testing temperature for at least 20mins before the test.

Figure 16 shows engineering tensile properties of MA956 and PM2000 alloy at various temperatures. Their tensile properties are very similar because their chemical compositions are nearly same. Tensile properties vary significantly above 500°C. Significant decrease of strength above 500°C can be explained by large void formation through accelerated diffusion at high temperature.

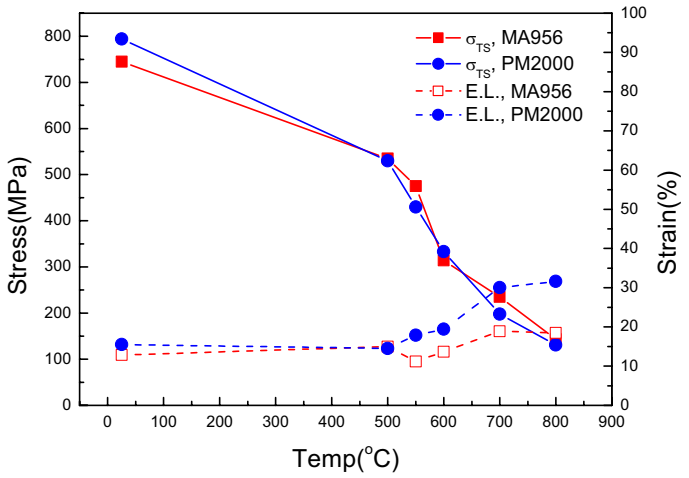

Figure 16 Summary of tensile properties of MA956 and PM2000.PM2000 is in as-rolled condition containing small grains, which are not appropriate at high temperature.

2.4.3 Creep Rupture Properties

Creep rupture tests of MA956 and PM2000 alloy are conducted in the constant load creep tester equipped by an electrical furnace and LVDT. Test conditions and results are summarized in Table 7. Figure 17 shows comparison between experimentally measured Larson-Miller parameters and reported values by manufacturer. MA956 shows better creep rupture properties than PM2000 because PM2000 is in as-rolled condition containing small grains, which are not appropriate at high temperature.

Table 7 Test conditions and results on the creep rupture properties of MA956 and PM2000 alloys.

Temperature(°C)	PM2000		MA956	
	Stress (MPa)	Life Time (hrs)	Stress (MPa)	Life Time (hrs)
520	230	430.1	350	9
550	210	11.64	300	5.5
	180	751	250	33.5
600	190	6.3	200	50
	130	954	180	-
700	150	17.52	150	738.5
	120	300	-	-

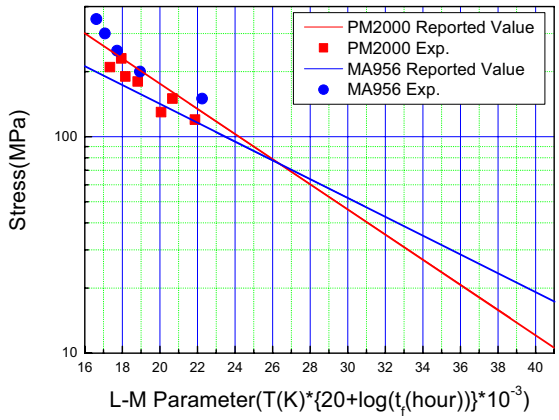

Figure 17 Larson-Miller parameters of MA956 and PM2000.

Figure 18 is the typical creep rupture result of PM2000 alloy tested at 520°C and 230Mpa. Even though this curve shows creep behavior that deviated somewhat from the conventional case (primary, steady state, and tertiary stage) due to accelerated creep rupture test, the creep deformation is retarded due to dislocation pinning by dispersoids in coarse grained microstructure. High temperature strengthening mechanism of ODS alloy is Orowan hardening induced by dislocation-dispersoid interaction, and many interactions are observed in TEM micrograph.

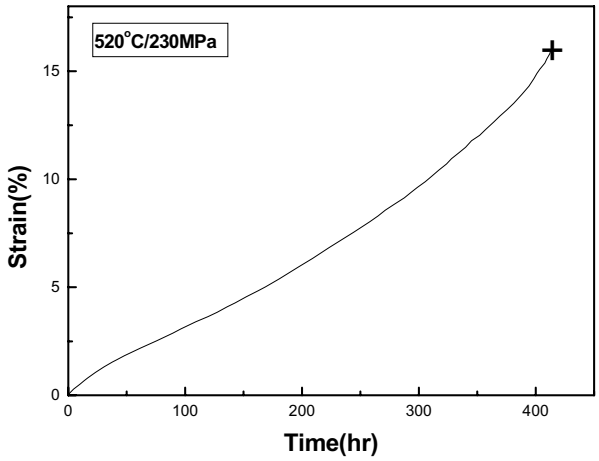

Figure 18 Typical creep rupture curve of PM2000 tested at 520°C, 230MPa.

2.4.4 475°C Embrittlement

Hardening of Fe-Cr alloy during aging in the vicinity of 475°C causes an increase of yield stress and tensile strength, and also an increase of the ductile–brittle transition temperature[2]. The phenomenon in ODS alloys is similar to this so-called "475°C embrittlement" observed in duplex stainless steels and Fe–Cr based alloys.

Tests to investigate the embrittlement behavior of the ODS alloys were conducted. In all cases specimens are removed from the centre of the raw material. Heat treatments are carried out in a box furnace in air. Isothermal heat treatments at 475°C are performed from 0 to 500hrs. Isochronal (100

h) aging treatments are also performed at 400, 475, 550°C. The grain size and texture of the microstructures are not expected to change since the recrystallization temperature of these alloys is much higher. Micro-vickers hardness test(Akashi HM-124) is performed for mounted and polished specimens at a cross section perpendicular to the longitudinal direction of the bar. Indentations are made with 500gf load and 10 s dwell time. At least 5 measurements are made on each sample.

Figure 19 shows the hardness increase during isothermal heat treatments at 475°C for different materials. In all cases, hardness increases very fast at the earlier stages of hardening. As-extruded MA956 tube and PM2000 plate show higher hardness than recrystallized MA956 rod. Hardness increase during isochronal heat treatments is shown in Figure 20. Hardness increases from 400 to 475°C and then decreases to very small values at 550°C. In all cases, maximum hardening occurs at 475°C, i.e., neither the processing route nor the texture or grain size affect the temperature at which maximum hardening occurs.

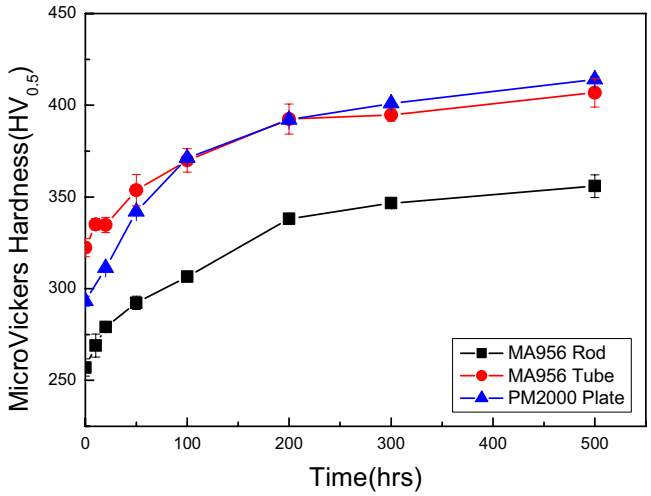

Figure 19 Hardness change of MA ODS alloys during isothermal heat treatment at 475°C.

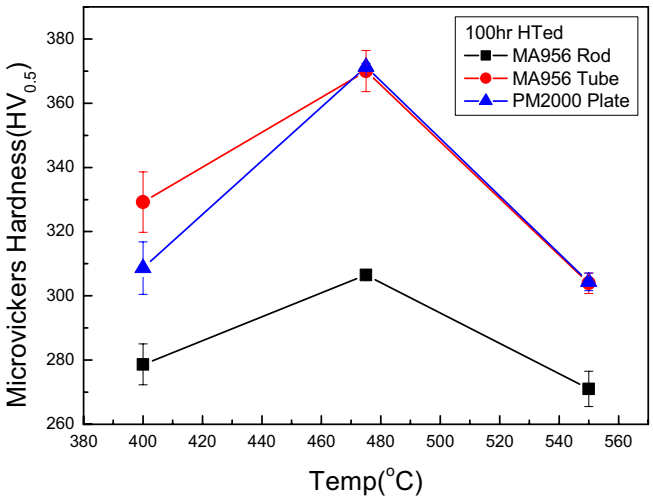

Figure 20 Hardness change of MA ODS alloys during isochronal heat treatment(100hrs).

Charpy impact tests for MA956 rod are performed on the specimens heat treated at 475°C for 0~100hrs. Schenck Trebel impact tester is used, and test conditions are 150J for hammer energy and 5.42m/sec for hammer speed. Charpy specimens with V-notch are machined in a perpendicular direction to the elongated grain. Different from the hardness increase behavior, impact energy increases very sharply due to the high strain rate. When the heat treatment time increases, the fracture mode changes to more brittle mode as shown in Figure 21. Figure 22 shows representative fracture surface with both grain boundary facet and cleavage surface, which are typically shown in brittle fracture mode.

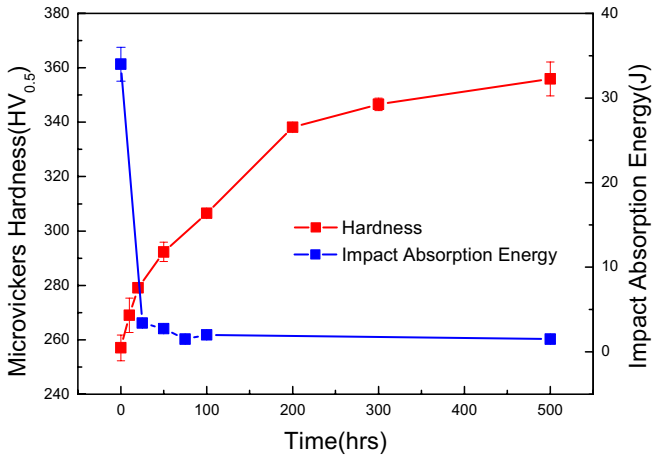

Figure 21 Hardness and absorbed impact energy change of MA956 alloy during isothermal heat treatment at 475°C.

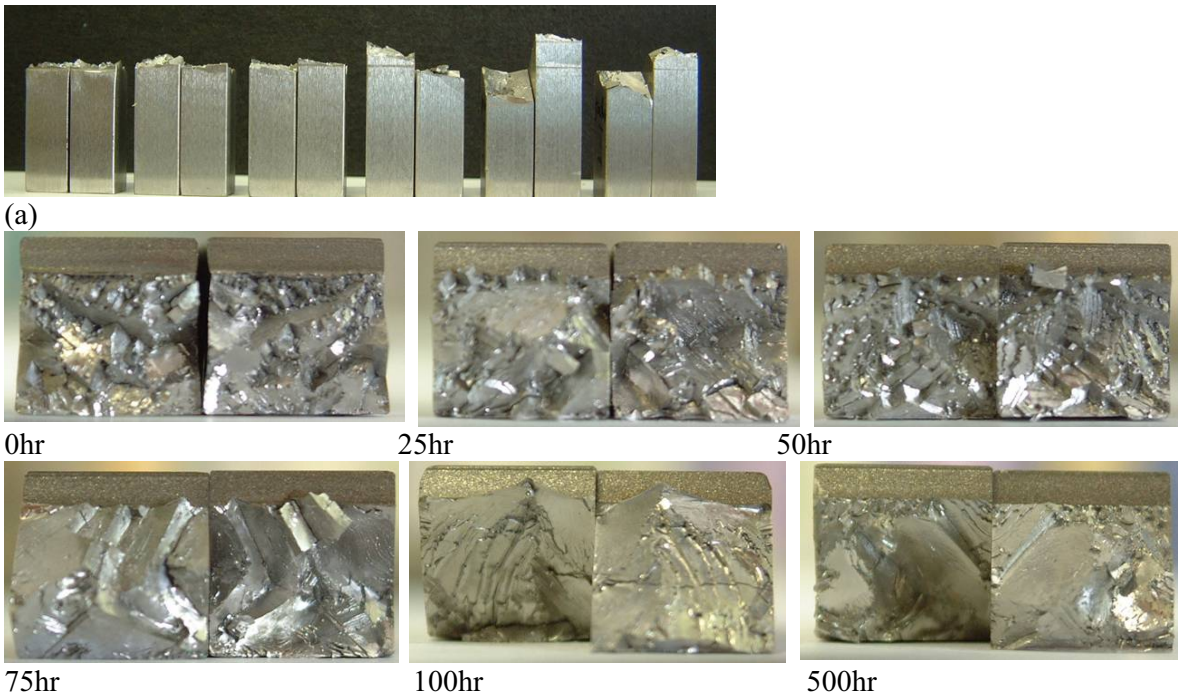

Figure 22 Fracture surface of Charpy impact tested MA956 rod. (a) side view(time increases from left to right) (b) top view.

Several mechanisms responsible for the 475°C aging embrittlement of Fe-12Cr steels have been suggested. The mechanisms responsible for this decrease in toughness have The mechanisms responsible for this decrease in toughness have never been unequivocally explained, but it has been generally attributed to the precipitation of second phases and/or impurity segregation. The first is the segregation of potent embrittling elements, such as Sn or P, to the prior austenitic grain boundaries in the conventional Fe-Cr material. The segregation of impurities to the grain boundaries dramatically worsens the situation for the conventional material, consistent with reports of a synergistic relationship between the amount of segregants and hardness on the toughness of steels [3]. The second is the presence of alpha prime phase, which is well known embrittler for higher Cr-containing steels [4] and Ni-base alloys [5]. After isothermal aging at 475°C, Fe-Cr alloys contain large quantities of alpha prime phase (Cr-rich, bcc structure) in addition to Cr-rich M23C6 carbides and complex Cr-Fe-Mo-Ni-Si rich precipitates. Although the role of the carbides and Ni silicides have not been fully understood, the decrease of the DBTT(Ductile Brittle Transition Temperature) with the deembrittling treatment coinciding with the disappearance of the alpha prime phase in the microstructure strongly infers that the alpha prime phase is playing a strong role.

Hardness or strength level of the material is considered to be very important for susceptibility to aging embrittlement. Fe-10Cr alloys developed for steam turbine applications have not reported significant increases of the DBTT upon isothermal aging at 475°C and above [6]. However, these materials possess a lower strength than Fe-Cr alloy with high Cr content; and thus, should be more tolerant to the formation of alpha prime phase. At some point, there is a critical Cr content (or Cr equivalent) below which alpha prime will not form.

2.4.5 Mechanical Properties of Fabricated Experimental ODS Alloys

Having found that the commercial 20%Cr Fe-base ODS alloys were significantly subject to the thermal embrittlement at 475°C it was attempted to develop a series of experimental Fe-base ODS steels by MA(Mechanical alloying) and HiPPing (Hot Isostatic Pressing)/Hot Rolling processes; and the mechanical properties of the ODS alloys were evaluated. Table 8 shows the tensile properties of the experimental Fe-base ODS alloys at room temperature and at 600°C. Figure 23 shows the stress-strain curves of the ODS alloys at 600°C. There seems to be a large effect of the nitrogen addition on the strength by nitrogen addition.

Table 8 Tensile test results of developed Fe-base ODS alloys at room temperature and at 600°C.

RT					600oC	
Alloys	YS (MPa)	UTS (MPa)	El (%)	YS (MPa)	UTS (MPa)	El (%)
#1	544	785	24.6	334	401	27.2
#2	584	790	16.8	355	431	29.7
#3	1170	1802	3.5	539	686	19.9
#4	1427	1933	5.2	519	668	22.6

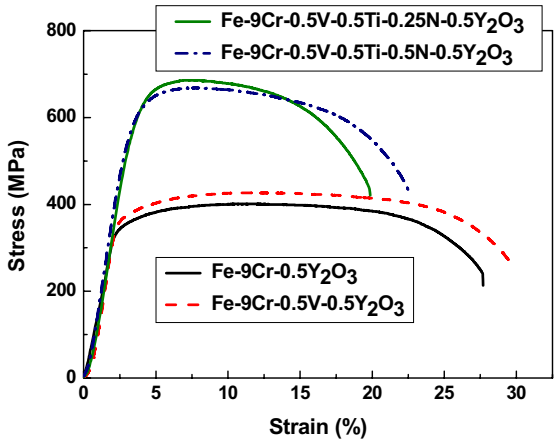

Figure 23 Stress-strain curves of experimental Fe-base ODS alloys at 600°C.

2.4.6 References

1. C. Capdevila, H.K.D.H. Bhadeshia, Adv. Eng. Mat., Vol. 3, No. 9, pp. 647, 2001.
2. J. Chao, J. L. Gonzalez-Carrasco, Mater. Sci. Technol., Vol. 14, pp.440, 1998.
3. T. M. Angeliu, E. L. Hall, M. Larsen, A. Linsebigler and C. Mukira, "Aging Embrittlement of Fe-12Cr Steels", GE Report Number 98CRD067, GE Research & Development Center, April 1998.
4. P. J. Grobner, "The 475℃ Embrittlement of Ferritic Stainless Steels", Met. Trans. A, Vol. 4, pp. 251-260, 1973.
5. J. F. Radovich, "Effect of Alpha Chromium on Long Time Behavior of Alloy 718", Superalloys 718, 625, 706 and Various Derivatives, E. A. Loria ed., TMS Society, pp. 409-415, 1997.
6. C. Berger, E. Potthast, R. Bauer and G. A. Honeyman, "Development of High Strength 9-12%CrMoV Steels for High Temperature Rotor Forgings", 11th International Forgemasters Meeting, Terni/Spoleto, Italy, June 1991.

2.5 Thermal Properties of SCWR Materials

Contributors:

Joy Rempe, Keith Condie, Darrel Knudson, INL

2.5.1 Overview

As part of efforts to evaluate candidate alloys for Super Critical Water Reactor (SCWR) applications, selected high temperature thermal properties for T91 (a 9% Cr alloy) and HCM12A (a 12% Cr alloy) were investigated. Two methods available at Idaho National Laboratory's (INL's) High Temperature Test Laboratory (HTTL) were applied to estimate thermal diffusivity, thermal conductivity, and specific heat capacity. Results are compared with data in the literature and with data for other metals typically found in Light Water Reactor (LWR) vessels, SS304 and SA533B1.

2.5.2 Background

Several American Society of Testing and Measurement (ASTM)-approved methods for measuring thermal conductivity exist, but each of these methods has limitations that hinder efficient measurement of materials at temperatures and conditions of interest. INL's HTTL is investigating several methods for measuring thermal conductivity at high temperatures (up to 3000 K). One of these methods is classified as a steady state method, and it relies on radial conduction techniques. The remaining two methods are classified as transient state methods: one that relies on transient diffusivity techniques and one that relies on hot-wire techniques. These transient methods require smaller sized samples for testing. Because the amount of candidate SCWR materials available for testing was limited, only transient methods were considered. This section describes the two transient techniques that were investigated and provides details related to applying each method.

2.5.2.1 Transient Pulsed Diffusivity Methods

This effort primarily relied upon pulsed Thermal Diffusivity Methods (TDMs) to obtain high temperature SCWR candidate material thermal properties. TDMs are based on the material's thermal diffusivity, α; the thermophysical property that best determines the speed of heat propagation by conduction during changes of temperature with time. The thermal diffusivity, α, is defined by

$$\alpha = \frac{k}{\rho c_p} \qquad (1)$$

where k represents the thermal conductivity, c_p represents the specific heat capacity, and ρ represents the density. As indicated in this definition, the thermal diffusivity affects any conductive transient heat transfer process within the medium. The higher the thermal diffusivity, the faster the heat propagation.

In this project, TDM data were obtained using an Anter Thermal Properties Analyzer (FL 5000) System that is installed at INL's HTTL (see Figure 24). This system uniformly heats a small disk-shaped sample (approximately 12 mm in diameter and 2 to 4 mm thick) over its front face with a very short pulse of energy from a laser in a temperature-controlled furnace. The time-temperature history of the rear face of the sample is recorded through high-speed data acquisition from a solid-state optical sensor with very fast thermal response. Thermal diffusivity is determined from the time interval after the flash for the rear face to increase in temperature (using the Clark and Taylor method[1]). Specific heat capacity and thermal conductivity data were estimated using comparative techniques with software provided by Anter[2].

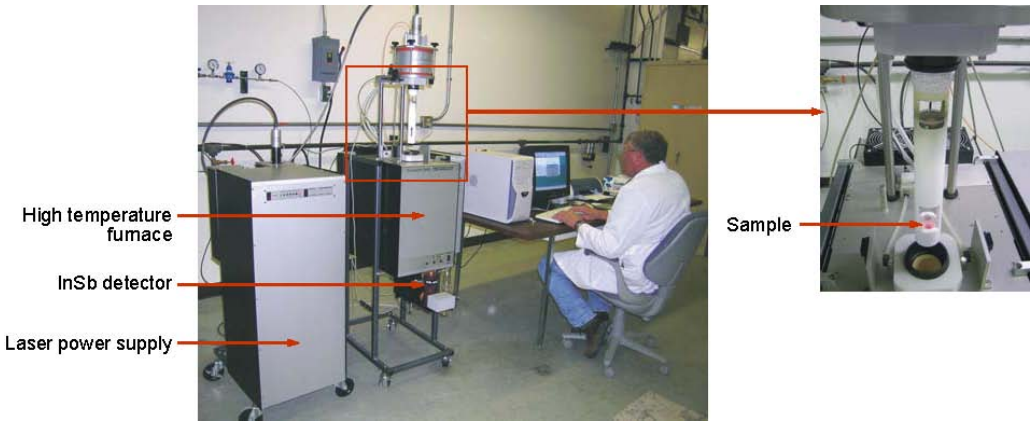

Figure 24 Laser Flash Thermal Property Analyzer installed at HTTL.

2.5.2.2 *Transient Hot Wire Method*

In addition to TDM data, INL also explored the use of Transient Hot Wire Method (THWM) techniques for obtaining SCWR thermal conductivity data. The THWM, sometimes referred to as the line heat source method, is based on a linear heat source of infinite length and infinitesimal diameter. The method was first suggested by Schleirmacher[3]. Numerous references may be found in the literature describing applications of this method to measure the thermal conductivity of solids, fluids, and gases (e.g., see references [4-9]). Today, several commercial vendors offer systems measuring thermal conductivity based on THWM techniques (e.g., see reference [10]).

Figure 25 shows a sketch of the design initially proposed for investigating this method. A heater is placed in the center of the sample that extends nearly the entire length of the sample. The heater element is constructed similar to a thermocouple. However, a single wire with high electrical resistivity (e.g., rhenium or molybdenum) is threaded through two-hole, high temperature electrical insulation material (e.g., hafnia); and its ends are connected to power leads at the top. The threaded wires are placed in a high temperature sheath material (e.g., niobium alloy) and then swaged to form an integral heater. For initial temperature measurements, commercially-available thermocouples were used (e.g., Type K chromel/alumnel). However, higher-temperature, in-pile testing will require INL-developed thermocouples composed of alloys of molybdenum and niobium thermocouples that resist transmutation [1].

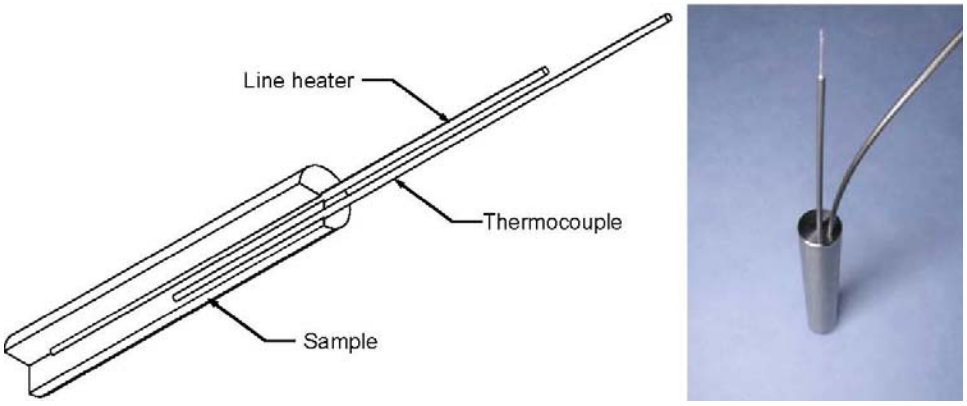

Figure 25 Sketch and photo of sample with heater and thermocouple installed.

Several options are available for placing the heater and thermocouple in the sample. At INL, the heater and thermocouples were inserted into holes that were drilled into the sample (as shown in Figure 25). Contact resistance between the heater and the sample raises the heater temperature and extends the time to t_1 (when the temperature rise becomes linear). Likewise, any contact resistance between the thermocouple and the sample has a similar effect.

Heater power is provided by a small DC power supply with the power determined by precise measurements of current and voltage. Because the resistance of candidate materials for the heater element increases with temperature, it is necessary to continuously adjust the voltage to maintain a constant power level. This control is provided automatically using a LabView program, which monitors the power and adjusts the voltage several times a second to keep the power constant.

2.5.3 Approach

Tests were completed to obtain high temperature thermal property data for candidate SCWR materials using the TDM and THWM described previously. In addition, data were obtained for typical materials found in LWR vessels (SA533B1, which is used for most LWR vessels; and SS304, which is used for LWR piping and internal structures).

Using an Anter FL5000, thermal diffusivity data were obtained using the Clark and Taylor approximation. Comparison reference samples (Austenitic Stainless Steel and Iron) provided by Anter were used to estimate thermal conductivity and specific heat capacity for materials with this method. The THWM approach was applied to directly obtain thermal conductivity data for these materials. Note that this study was the first attempt by INL to apply THWM techniques.

2.5.4 Results

2.5.4.1 FL5000

As noted in Section 2.5.2.1, TDM data were obtained in this project using an Anter FL5000 system installed at the HTTL. Test samples were approximately 12 mm in diameter and 2 to 4 mm thick. Test samples were designated by a test number (e.g., 400 through 430), their thickness (e.g., 2 to 4), a numeric letter (e.g., A through C to denote the first through third sample of a particular thickness), their coating (e.g, “C” for graphite sprayed, “BN” for boron nitride sprayed, or “GB” for grit blasted), and the voltage at which samples were tested (e.g., 1200 to 1500 V).

Thermal diffusivity data were calculated using the Clark and Taylor method [1], which is encoded into software provided by Anter for the FL5000 system. Specific heat capacity and thermal conductivity data were estimated using comparative techniques with software and reference samples provided by Anter. However, peak temperatures for which specific heat capacity and thermal conductivity data could be estimated were constrained to peak test temperatures for these reference samples (due to concerns about variations in data if samples were subjected to temperatures at or above where they experience a phase transition).

2.5.4.1.1 Stainless Steel

Thermal diffusivity data for stainless steel samples (SS304) are plotted in Figure 26. As indicated by the legend in this figure, SS304 data were obtained from testing 13 samples with thicknesses varying from 2 to 4 mm, laser powers varying from 1000 to 1500 V, and various types of sample coatings (graphite, boron nitride, and grit blasted). Data in this figure suggest that variations in test parameters did not produce any discernible trend in the test data. Figure 27 compares the SS304 data with data obtained from the Anter reference stainless steel sample, Anter reference sample thermal diffusivity data, and the recommended diffusivity (based on Touloukian data) from Figure 28.

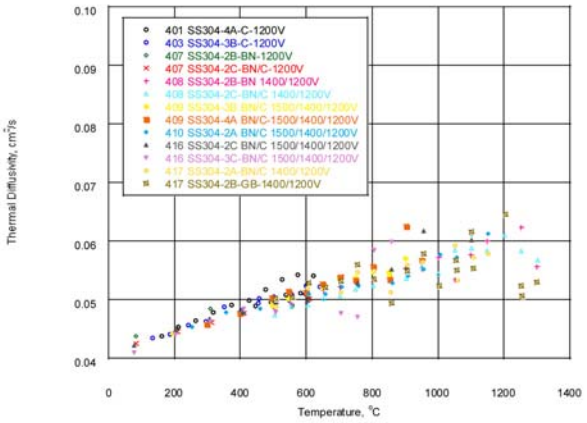

Figure 26 SS304 thermal diffusivity data.

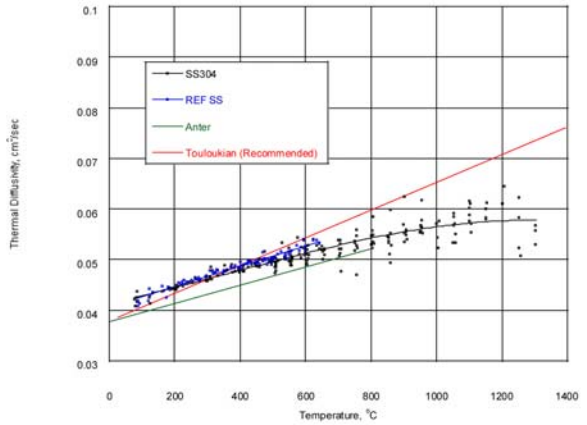

Figure 27 Comparison of SS304 and reference stainless steel thermal diffusivity data with values provided in the literature (literature curves extrapolated above 1000 °C).

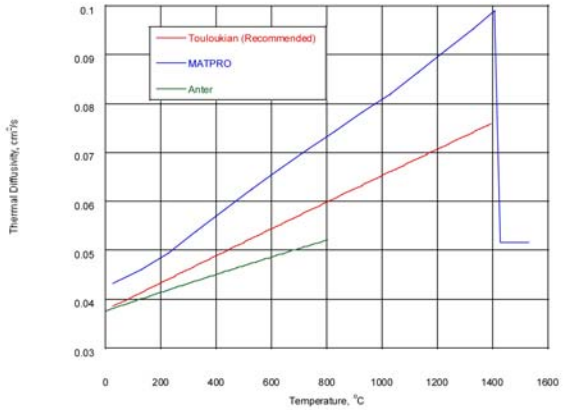

Figure 28 Comparison of selected reference information for stainless steel thermal diffusivity.

Recommended values for stainless steel are extrapolated above 1000 °C. As shown in Figure 27, the SS304 data agree fairly well with reference sample data. Values for the SS304 and reference samples also agree fairly well with Figure 28, the recommended values at lower temperatures. More scatter occurs in data obtained at higher temperatures. However, high temperature data appear lower than the recommended Touloukian values at temperatures above 600 °C.

Using software provided by Anter, the specific heat capacity and thermal conductivity of the SS304 samples were estimated using comparative techniques and data for a similar sample (in this case, the reference stainless steel sample provided by Anter). Figure 29 and Figure 30 illustrate the data obtained using these techniques. Recommended curves (which are based on Touloukian data) are also plotted in these figures.

Curve fits from data estimated with the Anter comparative software are similar to the recommended values. However, there is considerable scatter in the data. More testing is needed to reduce the uncertainty in the specific heat capacity and the thermal conductivity of this material (especially at higher temperatures).

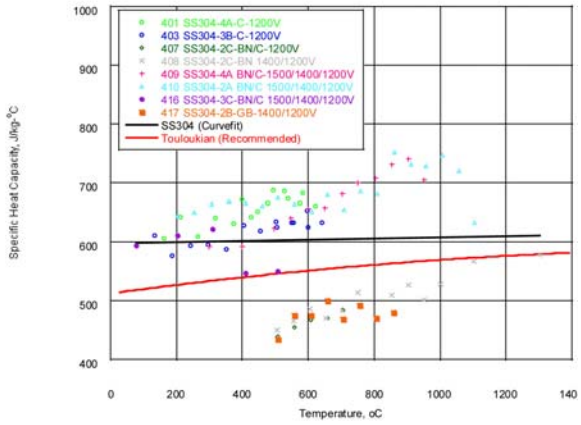

Figure 29 Comparison of SS304 specific heat capacity data obtained with FL5000 and Touloukian data.

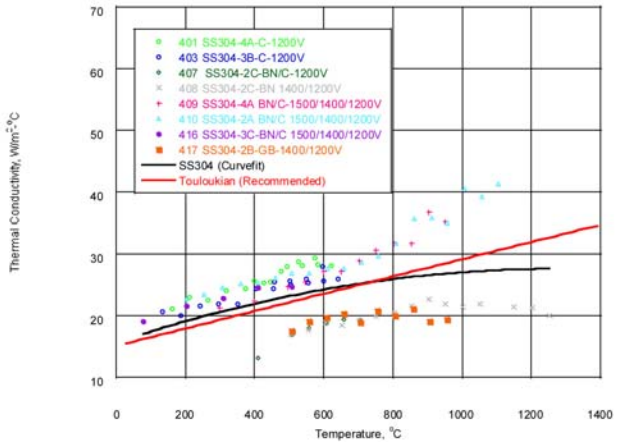

Figure 30 Comparison of SS304 thermal conductivity data obtained with FL5000 and Touloukian data.

2.5.4.1.2 SA533B1

Thermal diffusivity data for SA533B1 samples tested are plotted in Figure 31. The SS304 data were obtained from testing 9 samples with thicknesses varying from 2 to 4 mm, laser powers varying from 1000 to 1500 V, and various types of coatings (graphite, boron nitride, and grit blasted). Data suggest that variations in test parameters did not significantly affect test data. As in SS304 tests, there is more scatter in higher temperature SA533B1 data. However, a change in the behavior of the SA533B1 diffusivity occurs at temperature above 727 °C, which is the temperature where this material starts to experience a transformation (from ferritic to austenitic steel). Data also indicate that the general behavior of thermal diffusivity for carbon steel is more similar to that of iron than the stainless steel reference data. Figure 32 compares the SA533B1 data with data obtained for an Anter reference iron sample, Anter reference iron thermal diffusivity data, and the recommended diffusivity (based on MATPRO data). As shown in Figure 32, the newly obtained iron data are consistent with data recommended by Anter.15 The new SA533B1 data is similar (but somewhat lower) than data recommended by MATPRO (MATPRO SA533B1 data are based on information from Spanner, et al.12). More scatter occurs in data obtained at higher temperature. Note the relatively flat behavior in the SA533B1 data at higher temperatures (although there is a slight peak at around 1100 °C).

Using software provided by Anter, the specific heat capacity and thermal conductivity of the SA533B1 samples were estimated using comparative techniques and recommended material property data for reference iron. Figure 33 and Figure 34 illustrate the data obtained using these techniques. Recommended curves from MATPRO information are also plotted in these figures.

Curvefits from data estimated with the Anter comparative software yield similar values to the recommended values. However, there is considerable scatter in the data. More testing is needed to reduce the uncertainty in the specific heat capacity and the thermal conductivity of this material (especially at higher temperatures). For temperatures above 500°C, new data suggest higher specific heat capacities and lower thermal conductivities for SA533B1 than currently documented in the literature..

2.5.4.1.3 T91

Thermal diffusivity data for T91 samples tested at INL are plotted in Figure 35. The T91 data were obtained from eight tests using samples with thicknesses varying from 2 to 4 mm, laser powers varying from 1000 to 1400 V, and various types of coatings (graphite, boron nitride, and grit blasted). As indicated in this figure, variations in these test parameters did not significantly affect test data. There is more scatter in higher temperature T91 data. Test data suggest that a change in the behavior of the T91 diffusivity occurs at temperatures above 700 °C, such as might occur with a phase transformation. Data also indicate that the thermal diffusivity for T91 is much more similar to that of reference iron than reference stainless steel sample data.

Figure 36 compares the T91 data with recommended data obtained for the Anter reference iron sample (based on Touloukian data). Note that the recommended curve is extrapolated for temperatures above 1000 °C. The new T91 data appears much lower than iron at lower temperatures, but very similar at temperatures above 700 °C.

Using software provided by Anter, the specific heat capacity and thermal conductivity of the T91 samples were estimated using comparative techniques and data for reference iron. Figure 37 and 34 illustrate the data obtained using these techniques. A curve, based on ASM thermal conductivity data is also plotted in Figure 38. A curvefit from data estimated with the Anter comparative software yields similar, but slightly higher, values to the recommended thermal conductivity values. However, there is considerable scatter in the data. More testing is needed to reduce the uncertainty in the specific heat capacity and the thermal conductivity of this material (especially at higher temperatures).

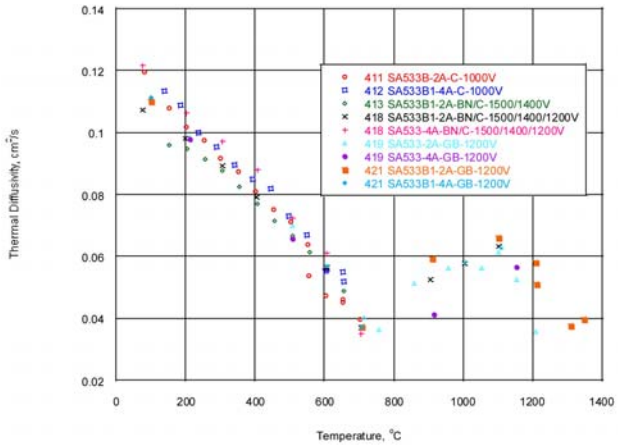

Figure 31 INL SA533B1 thermal diffusivity data.

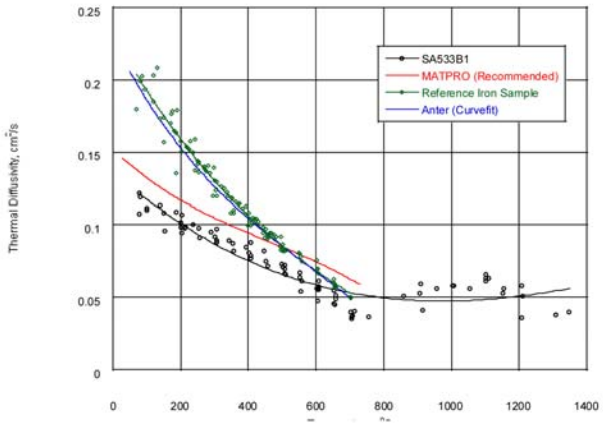

Figure 32 Comparison of INL SA533B1 thermal diffusivity data, reference iron data, and values provided in the literature.

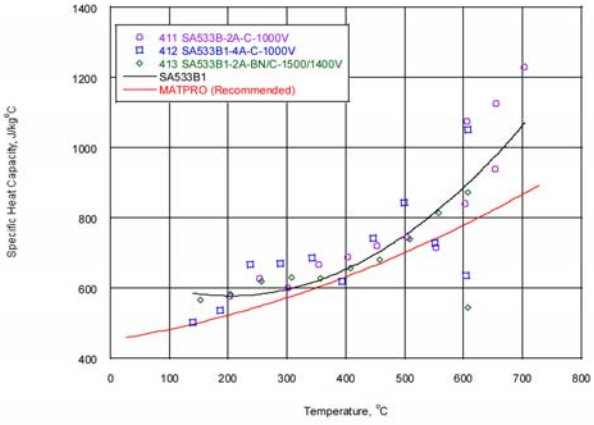

Figure 33 Comparison of INL SA533 specific heat capacity data and MATPRO data.

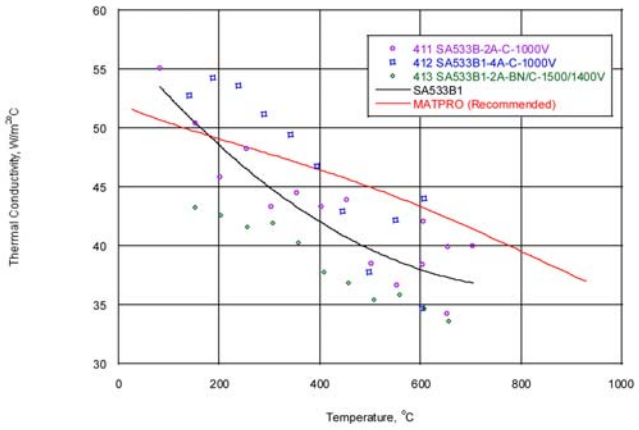

Figure 34 of INL SA533B1 thermal conductivity data and MATPRO data.

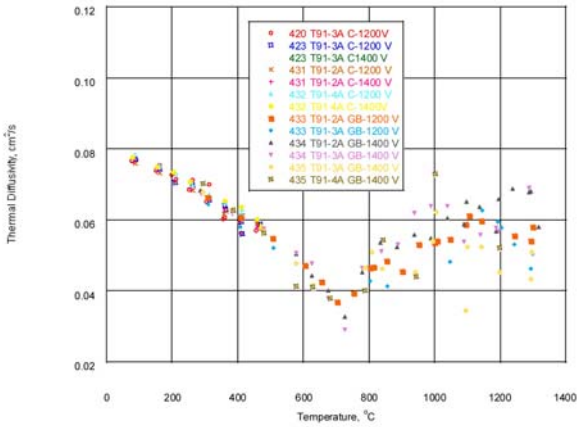

Figure 35 INL T91 thermal diffusivity data.

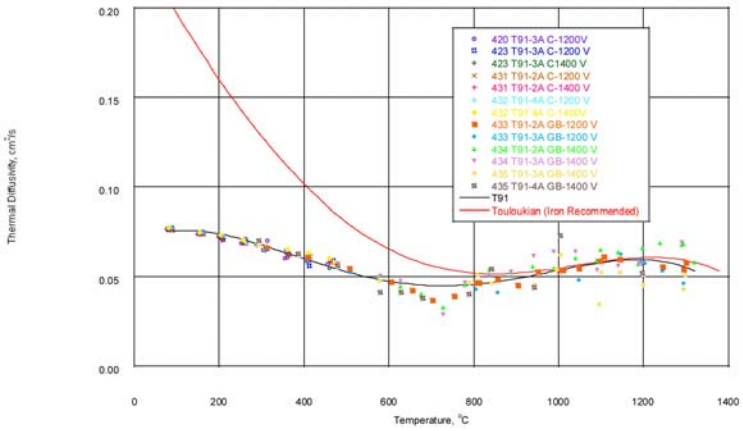

Figure 36 of INL T91 thermal diffusivity data and values provided in the literature.

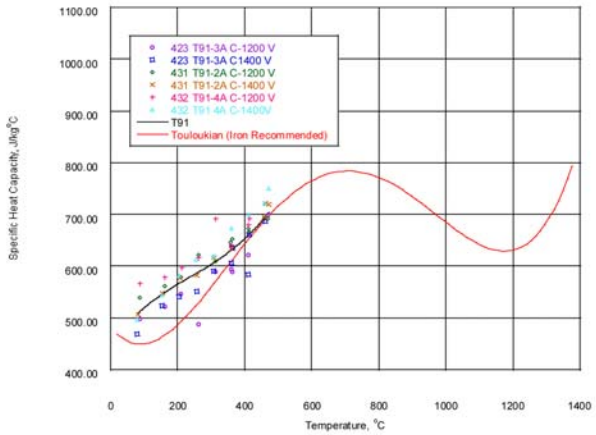

Figure 37 Comparison of INL T91 specific heat capacity data and ASM data.

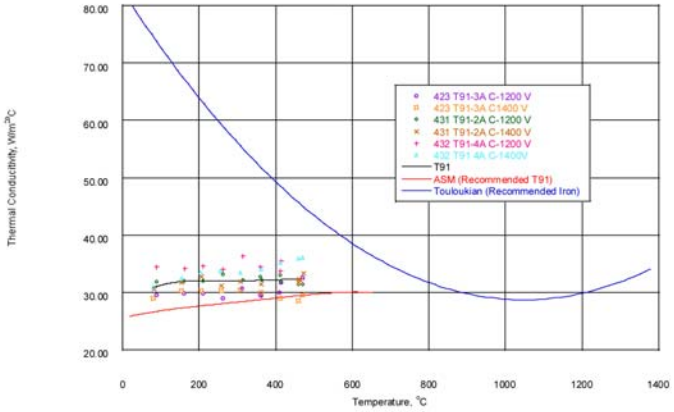

Figure 38 Comparison of INL T91 thermal conductivity data and ASM data.

2.5.4.1.4 HCM12A

Thermal diffusivity data for HCM12A samples tested at INL are plotted in Figure 39. The HCM12A data were obtained from seven tests using samples with thicknesses varying from 2 to 4 mm, laser powers varying from 1000 to 1400 V, and various types of coatings (graphite, boron nitride, and grit blasted). As indicated in this figure, variations in these test parameters did not significantly affect test data. There is more scatter in higher temperature HCM12A data. Test data suggest that a change in the HCM12A diffusivity occurs at temperatures near 700 °C, such as might occur with a phase transformation. Data also indicate that the thermal diffusivity for HCM12A is more similar to that of reference iron than reference stainless steel sample data.

Figure 40 compares the HCM12A data with data obtained for an Anter reference iron sample, Anter reference iron thermal diffusivity data, and the recommended diffusivity (based on ASM data). Note that literature curves are extrapolated for temperatures above 700 °C. The new HCM12A data is similar (but somewhat higher) than the ASM data (for the lower temperatures where ASM data are available).

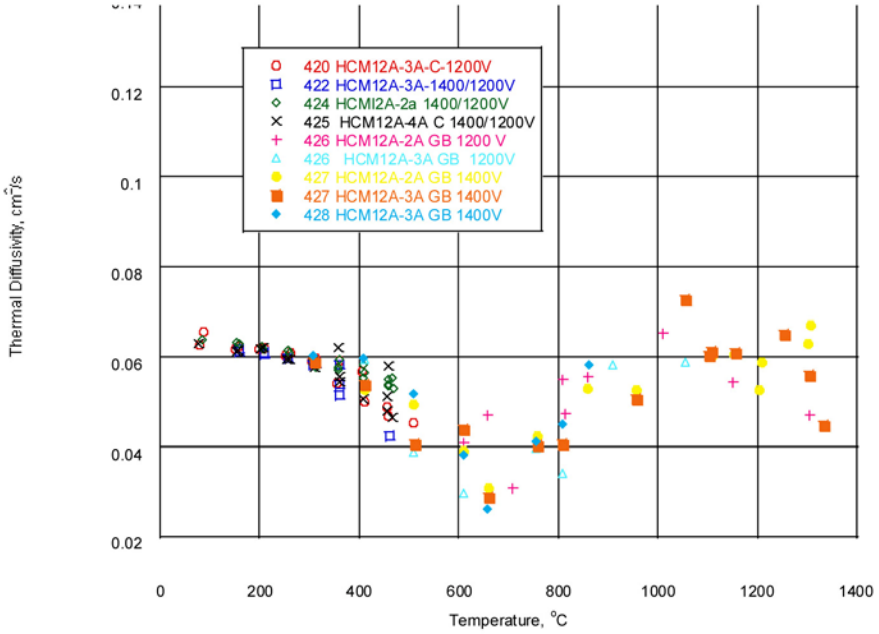

Figure 39 INL HCM12A thermal diffusivity data.

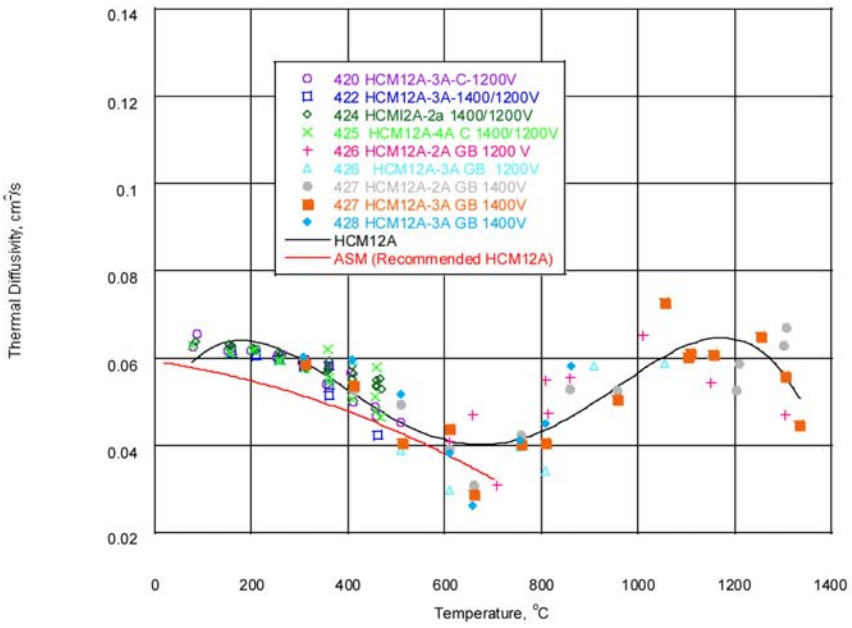

Figure 40 Comparison of INL HCM12A thermal diffusivity data and values provided in the literature.

Using software provided by Anter, the specific heat capacity and thermal conductivity of the HCM12A samples were estimated using comparative techniques and data for reference iron. Figure 41 and Figure 42 illustrate the data obtained using these techniques. Curves based on ASM data are also plotted in these figures.

Curvefits from data estimated with the Anter comparative software yield similar values to the recommended values. However, there is considerable scatter in the data. More testing is needed to reduce the uncertainty in the specific heat capacity and the thermal conductivity of this material (especially at higher temperatures). New data suggest similar specific heat capacities and higher thermal conductivities for HCM12A for temperatures where comparative techniques are available.

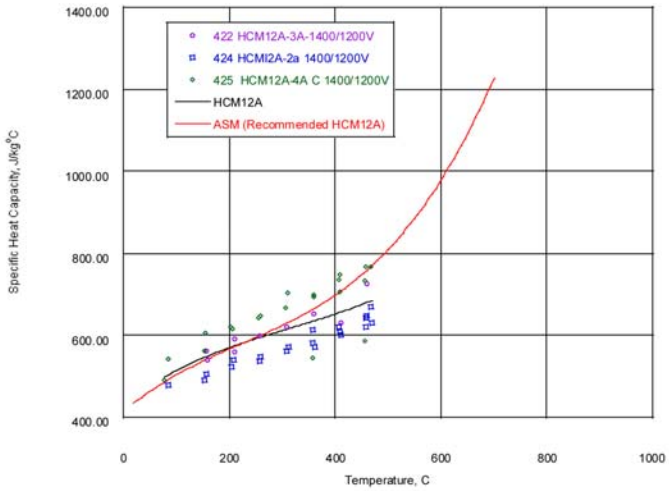

Figure 41 Comparison of INL HCM12A specific heat capacity data and ASM data.

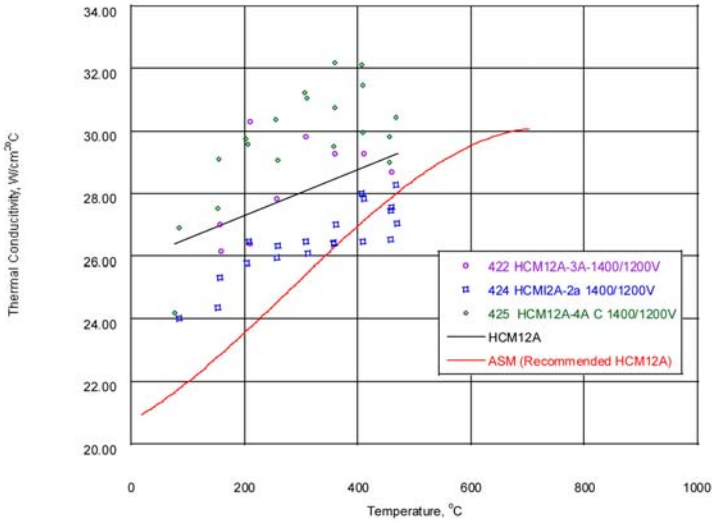

Figure 42 Comparison of INL HCM12A thermal conductivity data and ASM data.

2.5.4.1.5 Summary of FL5000 Results

The FL5000 System was applied to obtain thermal diffusivity data for the SCWR materials for temperatures up to 1400°C. Low temperature results (less than 1000 °C), as summarized in Table 9, indicate that the measured diffusivity data behavior is similar to data available in the literature for all of the materials tested (at least for those materials where data were available in the literature). High temperature diffusivity data were obtained for all of these materials. As discussed in this section, diffusivity values for the two SCWR materials and SA533B1 experienced a minimum at around 700 °C, which corresponds to where a phase transition occurs in carbon steel. It is interesting to also note that high temperature diffusivity data obtained for stainless steel differed from values reported in the literature (although it should be noted that literature values were extrapolated for temperatures above 1000 °C).

Software provided by Anter was employed to estimate sample thermal conductivity using comparative techniques. However, these efforts were hindered by reference sample test temperature limits. Values estimated with comparative techniques differed from values reported in the literature by up to 25% (see Table 9).

Table 9 Comparison of FL5000 TDM results with available literature data.

Material	Data Source	Thermal Diffusivity, cm^2/s				Thermal Conductivity, $W/m^2 \cdot °C$			
		20 °C	600 °C	1000 °C	1200 °C	20 °C	600 °C	1000 °C	1200 °C
SS304	Reference	0.037	0.055	0.065	0.072	15	24	29	33
	INL	0.037	0.052	0.056	0.058	20	25	27	28
SA533B1	Reference	0.15	0.055	NA	NA	52	44	NA	NA
	INL	0.12	0.052	0.052	0.052	57	38	NA	NA
T91	Reference	NA	NA	NA	NA	25	30	NA	NA
	INL	0.075	0.05	0.055	0.060	30	33	NA	NA
HCM12A	Reference	0.06	0.04	NA	NA	21	NA	NA	NA
	INL	0.06	0.04	0.055	0.065	26	30	NA	NA

2.5.4.2 Hot Wire Results

As noted in Section 2.5.2.2, an initial attempt was also made to apply THWM techniques. Figure 25 illustrates the geometry of the sample proposed for testing with a linear heater and thermocouple installed in it. Samples fabricated from SS304, SA533B1, and T91 were tested (HCM12A was not tested because of sample material limitations). This initial effort was limited to room temperature tests. Results from these efforts are summarized in this section.

2.5.4.2.1 Hot Wire Test Data

Two series of room temperature tests were completed for SS304, SA533B1, and T91 samples. Results from both series yielded similar values for thermal conductivity. Data obtained from the first series of tests are plotted in Figure 43. It is interesting to note that curves for carbon steel and stainless steel are similar. Reference information suggests that the slope of the carbon steel curve should be considerably higher than the slope of the stainless steel curve.

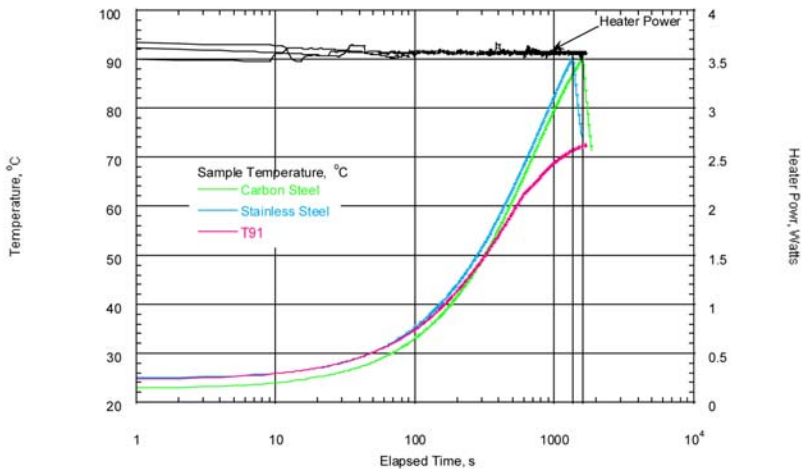

Figure 43 Results from room temperature hot wire tests.

2.5.4.3 Discussion of Hot Wire Results

Equation (2) was applied to estimate the thermal conductivity of each material using values for t1, t2, T1, T2, and the average heater power in Figure 43. Results, summarized in Table 10, indicate that estimated values for thermal conductivity using data from this setup are at least two orders of magnitude too small. It should be noted that the obtained data were similar to data obtained for the second series of tests. Hence, these data are repeatable. It should also be noted that the data varied if the outer boundary heat transfer condition varied. LWR material sample tests were repeated using highly insulated exterior boundary heat transfer conditions. The slopes of the SA533 and SS304 thermal response curves for these two materials were still similar, but considerably different than results from the uninsulated tests.

Table 10 Calculated thermal conductivity from room temperature THWM data.

Sample	t_1, sec	T_1, °C	t_2, sec	T_2, °C	t_0, sec[a]	l_{heater}	Q_w, W/m	k_{calc}, W/m°C	k_{ref},[b] W/m°C	k_{ref}/k_{calc}
SS304	600	68.12	1000	82.49	0.00	0.07239	49.34	0.140	15	107.5
SA533B1	600	65.85	1000	79.73	0.00	0.07239	49.25	0.144	52	360.5
T91	150	39.06	600	62.22	0.00	0.07239	49.25	0.235	25	106.5

a. Initial guess. However, subsequent guesses cannot give us the needed factor of 100 to get the reference thermal conductivity values.
b. Room temperature reference values in Table 1.

To better understand why there are such large differences between values for thermal conductivity from reference data and estimated with Figure 43 test data, it is useful to consider the recommended values for test geometries discussed in 2.5.2. Table 11 summarizes results from calculations performed to verify the suitability of the initial test setup using criteria discussed in Section 2.2.

Material availability and ease of insertion for future in-pile applications led to the initially-selected geometry for test samples and testing. This selection resulted in many of the Section 2.5.2.2 suggested criteria not being met (as indicated by the red shading in Table 11).

Table 11 Evaluation of Section 2.2 criteria for room temperature THWM setup.

Sample	α, cm^2/s	x, cm	Criterion 1	Criterion 2	Criterion 3: Eqn. 2, cm		Criterion 4: Eqn 3, s		Criterion 5: Eqn. 4, s	
			d_{sample}/d_{heater}	l_{heater}/d_{heater}	L_{sample}	$7.96*(\alpha t_2)^{0.5}$	t_1	x^2/α	t_2	$0.1(d_{sample}/4\alpha)$
SS304	0.12	0.4191	8	45.6	7.62	87.2	600	1.46	1000	0.34
SA533B1	0.037	0.4191	8	45.6	7.62	48.4	600	4.75	1000	1.09
T91	0.0075	0.4191	8	45.6	7.62	53.4	150	2.34	600	0.54

For example, Criterion 1 was not met for any of the samples. This criterion was not considered feasible. A ratio of dsample/dheater of at least 60 would require that the heater diameter be less than 0.001" (for a 0.5" diameter sample) or a 3.75" diameter sample (for the current 0.0625" diameter heater). Such small heater sizes are not considered viable, and such large samples of SCWR materials were not available. Criterion 3 was also not met for any of the samples tested. This criterion, which was suggested to counter end effects, related the sample length, thermal diffusivity, and total test time, t2, using Equation (3). Although the total test time could be increased by lowering the heater power, other requirements on the test time suggest that the heater power was adequate. Hence, sample lengths between 48 and 87 cm would be required to satisfy this criterion (which was not possible because of limited material availability). Criterion 5, which compared the total test time to the sample diameter and thermal diffusivity, was also not met. To met this criterion, one would also need sample diameters that were between 15 and 25 inches, which was also not viable for these tests.

Criterion 2, which was designed to minimize end effects, was met for all of the samples. The ratio of the sample length to diameter was 45.6, which was within the recommended range of 31 to 100. Criterion 4, which was designed to ensure that the thermal front reaches the temperature sensor, relates the distance between the heater probe and temperature sensor and the sample material thermal diffusivity.

In summary, initial efforts to apply THWM techniques appear to have yielded inaccurate values of thermal conductivity for the materials tested. It is speculated that errors in measured values are due to the selected sample, sensor, and heater geometries. Alternate geometries will be explored during the next year in other programs as INL continues its efforts to develop THWM techniques for in-pile applications.

2.5.5 Thermal Properties Summary and Recommendations

As part of efforts to evaluate candidate alloys for SCWR applications, selected high temperature thermal properties for T91 (a 9% Cr alloy) and HCM12A (a 12% Cr alloy) were investigated. Two methods available at INL's HTTL were applied to estimate thermal diffusivity, thermal conductivity, and specific heat capacity. Results are compared with data in the literature and with data for other metals typically found in LWR vessels, SS304 and SA533B1. However, a review of data in the literature indicated that material property data for these materials are extrapolated for temperatures above 1000 °C (and many are extrapolated at temperatures above 700 °C).

The FL5000 System was applied to obtain thermal diffusivity data for the SCWR materials for temperatures up to 1400 °C. Low temperature results (less than 1000 °C) indicate that the measured diffusivity data behavior is similar to data available in the literature for all of the materials tested (at least for those materials where data were available in the literature). Figure 44 compares curvefits for thermal diffusivity data obtained for these materials. As shown in this figure, diffusivity values for the two SCWR materials and SA533B1 experienced a minimum at around 700 °C, which corresponds to where a phase transition occurs in these materials. Values for the thermal diffusivity for these

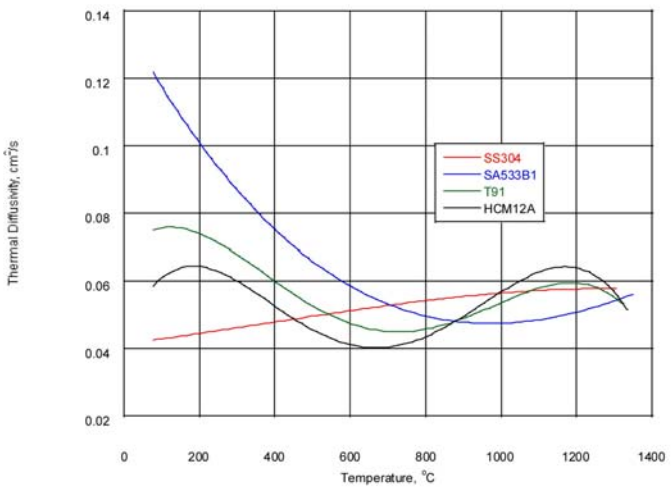

Figure 44 Comparison of thermal diffusivity data for materials tested.

materials at high temperatures (e.g., greater than 1000 °C) are similar (ranging from 0.05 to 0.065 cm2/s). It is interesting to also note that high temperature diffusivity data obtained for stainless steel differed from values reported in the literature (although it should be noted that literature values were extrapolated for temperatures above 1000 °C).

Software provided by Anter was employed to estimate thermal conductivities using comparative techniques. Data for SS304 could be obtained for temperatures higher than reported in the literature. However, as indicated in Figure 45, candidate SCWR and SA533B1 tests were limited to lower temperatures because they rely upon comparisons with reference iron sample test data, and it was recommended that this iron sample not be tested above its phase transition temperature. Lower temperature data in Figure 45 indicate that the two candidate materials have thermal conductivities that are lower than SA533B1, but higher than SS304. Additional tests are needed to evaluate their thermal conductivity at higher temperatures. Values estimated with these comparative techniques differed from values reported in the literature by up to 25%, which is consistent with scatter observed in thermal conductivity data reported in the literature.

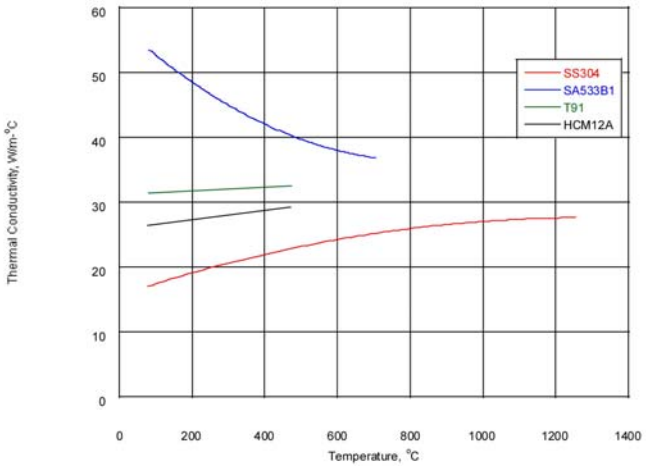

Figure 45 Comparison of thermal conductivity data for materials tested.

As noted in Section 2.1, an initial attempt was also made to apply THWM techniques. Figure 25 illustrates the geometry of the sample proposed for testing with a linear heater and thermocouple installed in it. Samples fabricated from SS304, SA533B1, and HCM12A were tested (T91 was not tested because of sample material limitations). This initial effort was limited to room temperature tests. Results indicate that estimated values for thermal conductivity are at least two orders of magnitude too small. It should be noted that the obtained data were similar to data obtained for the second series of tests. Hence, these data are repeatable. It is speculated that the error in measured values are due to the selected sample, sensor, and heater geometries. Alternate geometries will be explored during the next year as part of a different research project as INL continues its efforts to develop THWM techniques for in-pile testing.

2.5.6 References:

1. Clark, III, L. M. and R. E. Taylor, "Radiation Loss in the Flash Method for Measurement of Thermal Diffusivity," Journal of Applied Physics, 34(7):1909-1913, 1975.

2. Anter Corporation, see www. anter.com.

3. J. C. Spanner et al., Nuclear Systems Material Handbook, TID-26666, April 1976.

4. G. V. Smith, Evaluations of the Elevated Temperature Tensile and Creep Rupture Properties of C-Mo, Mn-Mo, and Mn-Mo-Ni Steels, Metal Properties Council, American Society for Testing and Materials, ASTM Data Series Publication DS47, 1971.

5. ASM International, Alloy Digest, T91/P91, 2002.

6. ASM International, Alloy Digest, HCM 12A, 2002.

7. Anter Corporation, Technical Note 102, Unitherm TM 600 Guarded hot plate thermal conductivity system, http://www.anter.com; accessed February 6, 2004).

8. N.N. Mohsenin, Thermal properties of foods and agricultural materials, Gordon and Breach Science Publishers, NY, 1980.

9. Prelovsek, P., Uran, B., "Generalized Hot Wire Method for Thermal Conductivity Measurements," J. Phys. E: Sci Instrum., Vol. 17, 1984.

10. Carslaw, H.S., and Jaeger, J.C., Conduction of Heat in Solids, 1959, Oxford University Press.

11. Healy, J. J., de Groot, J. J., and Kestin, J.1976, "The Theory of the Transient Hot-wire Method for Measuring Thermal Conductivity," Physical, 82C 392-408.

12. J. C. Spanner et al., *Nuclear Systems Material Handbook,* TID-26666, April 1976.

3. Task 3 - Corrosion and Stress Corrosion Cracking Studies

3.1 Task Summary

Corrosion and stress corrosion cracking (SCC) resistance of candidate materials in supercritical water is another key property that must be evaluated. The objective of this task is to chart the corrosion and stress corrosion cracking susceptibility of candidate materials in supercritical water under prototypic temperatures and water chemistries. As part of this task, the feasibility of using surface modification techniques to improve corrosion and SCC response is being evaluated. By conducting tests at multiple facilities, the impact of different experimental setups and techniques can be evaluated. As with the rest of the tasks, the efforts in this task have focused on evaluation of F-M alloys with a few additional experiments on other alloy types for comparison purposes.

3.2 SCC and Oxidation Experiments on F-M Steels

Contributors:

G. S. Was, University of Michigan

3.2.1 Design of the Stress Corrosion Cracking Test Facility

Figure 46 shows a schematic of the multi-sample supercritical water, stress corrosion cracking (SCW-SCC) facility in the High Temperature Corrosion Laboratory (HTCL) at the University of Michigan. Table 12 presents the summary of the specification for the main components of the facility. The test facility is composed of three main sub-systems: solution makeup system, solution feed & bleed system, and test vessel & load control system. In the solution makeup system there are two glass columns; one is a main water column and the other is a mixing column. Deionized water is filled in the mixing column and the makeup water is transferred to the main column. The test solution in the mixing column is fed through a high-pressure pump. To ensure high purity of the test water, a recirculation pump connected to the mixing column and ion-exchange resin runs continuously during a test. The solution feed & bleed system is mainly composed of a water chemistry monitoring system, a high-pressure pump, a preheater, a cooler, a back pressure regulator, and a water purification system. The specification of the high-pressure pump and water chemistry monitoring system is described in Table 12.

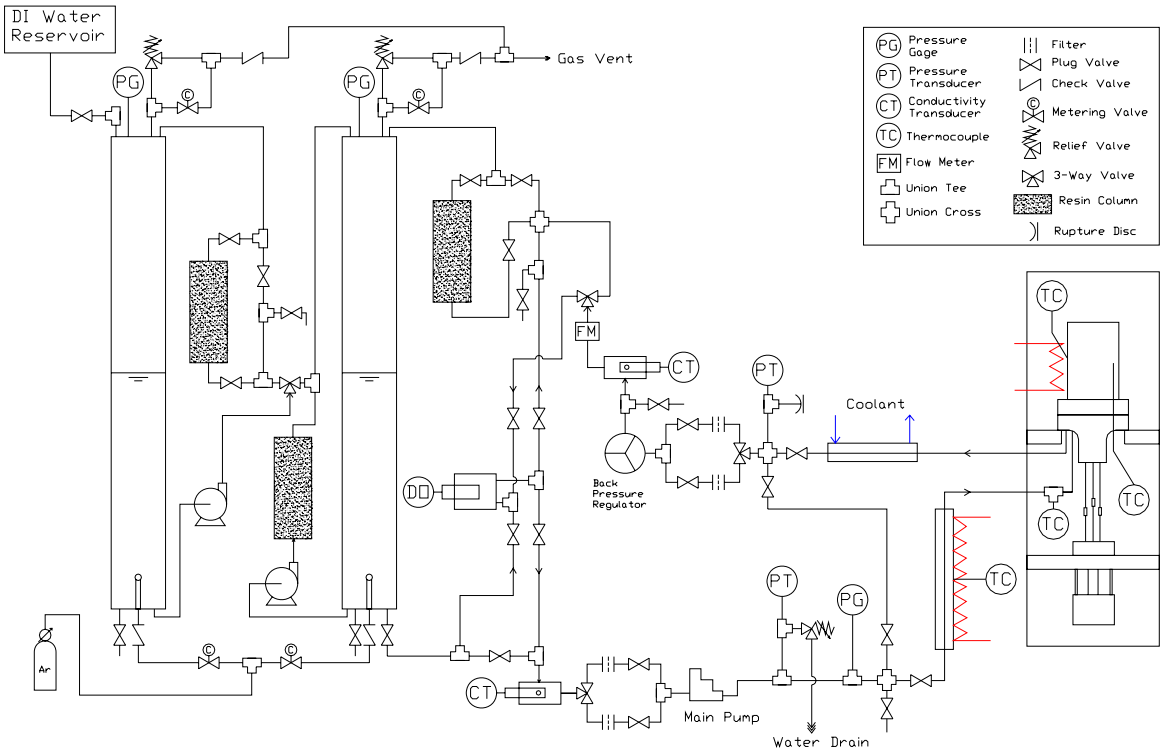

Figure 46 Schematic of multi-sample SCW-SCC facility in HTCL.

Table 12 Summary of the specifications for the main components of the SCW-SCC facility in HTCL.

Component Description	Main Specification	Comments
Test Vessel	Materials: Alloy 625 Max. Pressure: 4,350 psi @ 600 ^{o}C 5" ID & 12.5" Depth	Autoclave mounted in inverted position
Stepper Motor & Controller	Max. Load Capacity: ± 4,000 lb_f Max. Stroke Range: 4" Max. Stroke Rate: 2 in/min Min. Stroke Rate: 10^{-38} in/min Load Resolution: 0.1 lb_f Stroke Resolution: 0.0001" Waveform generator & Ramp generator	
High Pressure Pump	Flow Range: 0.01-250 mL/min Max. Pressure: 5,000 psi across the flow range Pulsation: <3% @150 mL/min & 2,500 psi Materials: 316SS	3-head design for high flow and low pulsation
Conductivity Meter	Range: 0.02-600 μS/cm Cell Constant Accuracy: ±1% of reading Max Pressure/Temp.: 250 psig@ 93 ^{o}C Materials: Ti, PEEK	
Dissolved Oxygen Meter	Operating Range: 0-10,000 ppb Accuracy: 1 ppb Flow Rate: 50-2,000 mL/min Temperature: 5-50 ^{o}C Pressure: <45 psig Materials: 316SS, Polyacetal	

A test vessel made of alloy 625 was installed in the inverted position (head at the bottom) on a load frame as represented in Figure 46. An inverted geometry has the advantage that the high-pressure fittings and penetrations on the top of vessel cover can be maintained at relatively low temperature without an additional cooling system. Another unique character of this vessel system is the fact that four SCC samples can be tested at the same time, which provides rapid sample throughput and reduces test-to-test variability caused by water chemistry variation in different tests. A stepper motor and controller with the load capacity of ± 4,000 lb_f was used in this system. By using the stepper motor and controller the strain rate can be decreased down to less than 10^{-8} s^{-1}. Figure 47 shows the photograph of the multi-sample SCC test facility in SCW environments.

3.2.2 Cross sectional analysis of F-M alloy gauge fractures

The F-M alloy samples exhibited extensive necking that consumed a considerable fraction of the gage section. In order to analyze cracking in a consistent manner, the gage sections were divided into three areas; A, B and C, as shown in Figure 48. Area A was defined by the distance from the fracture surface to the point where the gage width was80% of the original value. Area B extended from 80% to 90% and area C below the 90%point. Only cracks in areas B and C were recorded and included in the analysis. The total number of intergranular cracks of length greater than 3 μm was counted over a 2 mm length in areas B and C in SEM to determine a linear crack density, and the crack depths were characterized from cross sections.

Figure 47 Photograph of the multi-sample SCW-SCC facility in HTCL.

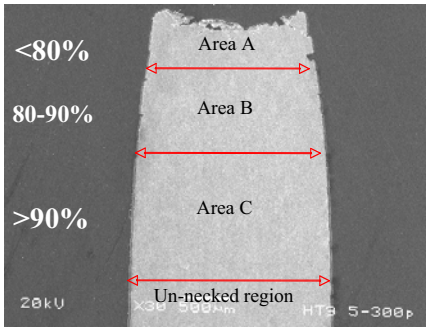

Figure 48 Areas A, B, and C defined on an HT-9 SCC sample tested in 500°C and 300ppb DO.

Cross sections of SCC samples of HT-9 for IG crack analysis were prepared by mounting in epoxy resin and then polishing with SiC paper. The mounted specimens were etched in 25% HCl and 75% HNO_3 in order to highlight the grain boundaries. Cracks were investigated in SEM in both secondary-electron (SE) mode and back scattered-electron (BSE) mode. The oxide layers on specimens were clearly observed in BSE mode. Crack depth was determined with Scion Image© software by comparing the crack length measured from the outer oxide layer to the deepest point, to that on the scale bar.

3.2.3 500°C SCC and Oxidation Rate Experiments in Deaerated and 100 ppb Dissolved Oxygen SCW

Initially two tests were conducted in supercritical water to begin to assess the SCC and oxidation behaviors of alloys T91, HCM12A and HT-9. Both tests were conducted at 500°C with the difference being the amount of oxygen in the water. The initial test was conducted in deaerated SCW at 500°C in the multi-sample supercritical water (MSCW) system built for this project. The CERT test was conducted on two T-91 samples, one HCM12A sample and one HT-9 sample at a strain rate of 3×10^{-7} s^{-1}. The second test was conducted on samples of T91 and HCM12A in 500°C supercritical water with the exception that the water contained approximately 100 ppb of oxygen. Data from fossil plant operation has shown that the addition of oxygen to the water in the range of 50-150 ppb promotes the formation of hematite (Fe_2O_3) in addition to magnetite (Fe_3O_4) that aids in promoting a more dense and less permeable oxide to reduce the oxidation rate[1,2]. . Additional baseline experiments were conducted in argon.

The stress-strain plots for all of the samples tested are shown in Figure 49. In the stress-strain plot, all samples showed similar work softening behavior. The two T91 samples tested in deaerated SCW exhibited different stress-strain behavior. The literature data for the mechanical properties of T91 [1-9] show a large amount of scatter such that the different stress-strain plots for the two T-91 samples fall within this scatter. The behavior of T-91 in deaerated SCW, 100 ppb O2 in SCW and Ar gas, all at 500°C are shown in Figure 49 (b). Only the sample in Ar has an atypical yield point. Otherwise, the stress-strain behaviors are similar, as are the strains at failure. Argon tests were conducted to serve as reference data for the SCW tests.

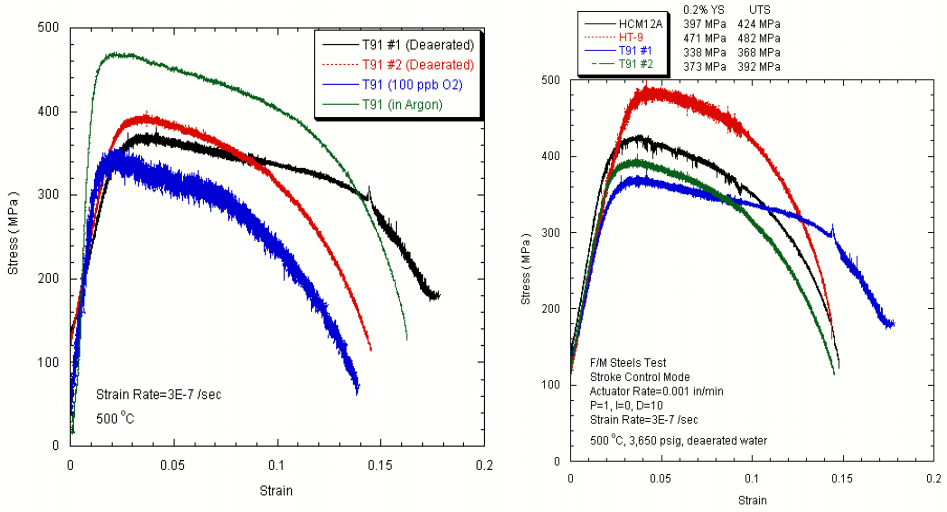

(a) (b)

Figure 49 Engineering stress-strain curves for (a) F/M steels tested in deaerated SCW and (b) T91 compared with the results tested in 100 ppb DO SCW and pure Ar gas.

The fracture surfaces of the failed samples are shown in Figure 50. All display ductile fracture behavior. The fracture surfaces of all samples except T91 #1 were exposed to SCW for about a day while waiting for T91 to fail. Therefore, they contained more oxide and were not as clear as that of T91 #1. The HT-9 sample showed less necking than other samples. The gage section surface cracks of HT-9 were deeper and wider than others, as shown in Figure 51. Some surface cracks of HT-9 have appearance similar to IGSCC cracks. Facture and side surfaces of T91 in 100 ppb DO were similar to those in

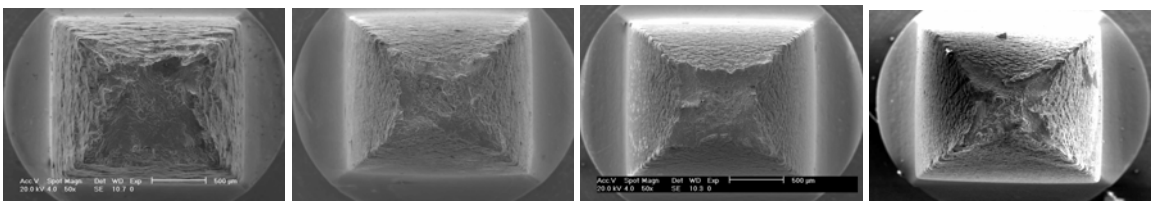

(a) HT-9 (b) HCM12A (c) T91 #1 (d) T91 #2

Figure 50 SEM images of the fracture surfaces of (a) HT-9, (b) HCM12A, (c) T91 #1, and (d) T91 #2.

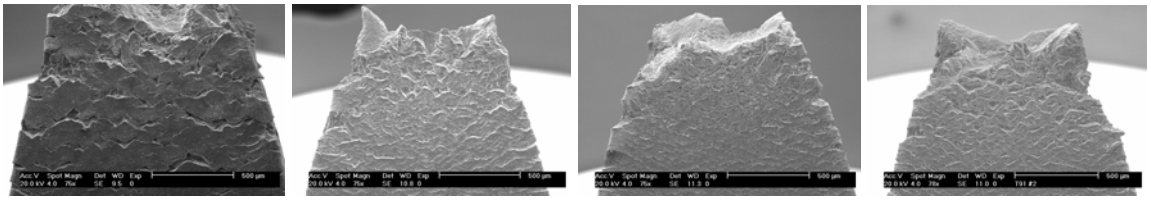

(a) HT-9 (b) HCM12A (c) T91 #1 (d) T91 #2

Figure 51 SEM images of the gage section surfaces of (a) HT-9, (b) HCM12A, (c) T91 #1, and (d) T91 #2.

deaerated SCW except for the presence of continuous side cracks. The reduction of area for T91 under SCW was lower than that under Ar gas.

The corrosion coupon analysis of T91 and HCM12A in deaerated SCW was performed by SEM, EDS, XRD, and XPS. Table 13 summarizes the oxidation results as measured by weight gain. Note two features of these weight gain measurements. First, HCM12A oxidizes less than does T91 in both environments. Also, samples in SCW containing 100 ppb oxygen result in less oxidation than those in deaerated SCW.

Table 13 Analysis of oxide weight gain and thickness after exposure to SCW at 500°C.

Alloy	T91-C-1	T91-C-2	HCM12A-C-1	HCM12A-C-2
System	MSCW	SCW	MSCW	SCW
Exposure time (hr)	182.2	236	182.2	236
Temperature (°C)	500	500	500	500
O2 content	<10 ppb	100-110 ppb	<10 ppb	100-110 ppb
Weight change (mg/dm2)	137.30	165.00	119.94	143.00
Weight change rate (mg/dm2/day)	18.090	16.785	15.803	14.547
Oxide thickness rate (μm/day)*	1.41304	1.12920	1.23485	1.02798

Cross-sections from the samples were analyzed by conducting energy dispersive x-ray analysis to determine the composition profile of the oxides. The images of the cross-sections show two distinct oxide layers from the metal substrate, Figure 52. The results of the composition profile using EDS line scan show two distinct oxide/metal ratios. The atomic percent ratio of O/Fe in outer oxide layer is 1.27 for T91 and 1.30 for HCM12A. These values are close to the ratio of O/Fe in Fe_3O_4 (1.33). For the inner layer, the O/M ratio (M = (Fe, Cr)) are 1.46 for T91 and 1.37 for HCM12A. These values are between O/M ratio of M_2O_3 (1.5) and M $_3O_4$ (1.33).

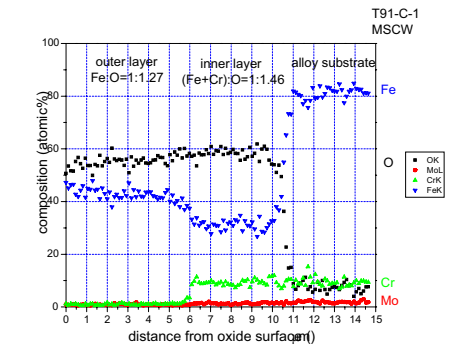

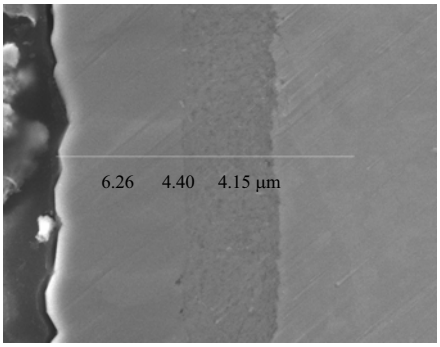

(a) T91 in deaerated SCW

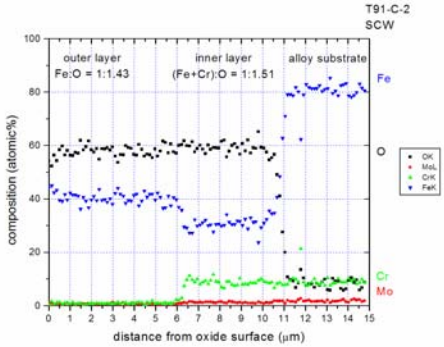

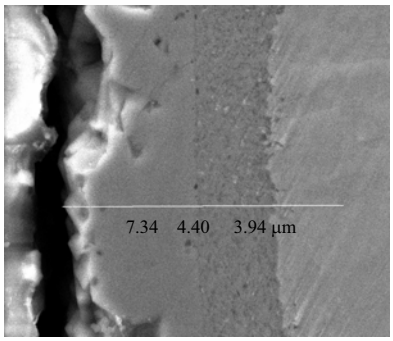

(b) T91 in 100 ppb DO SCW

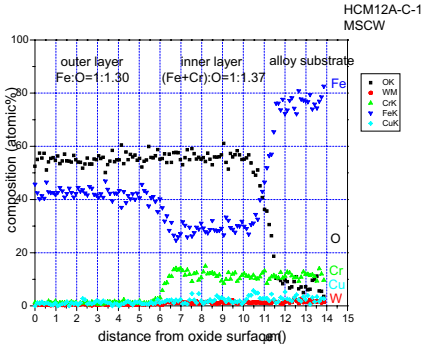

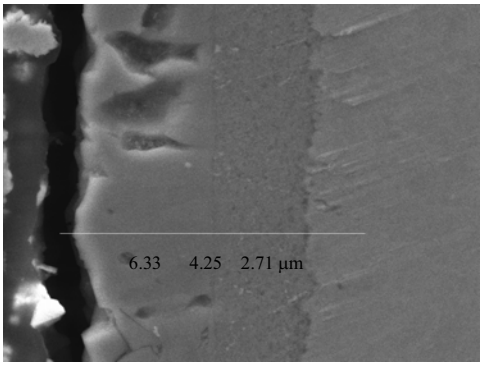

(a) HCM12A in deaerated SCW

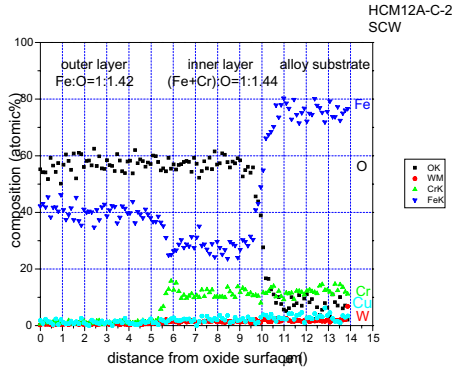

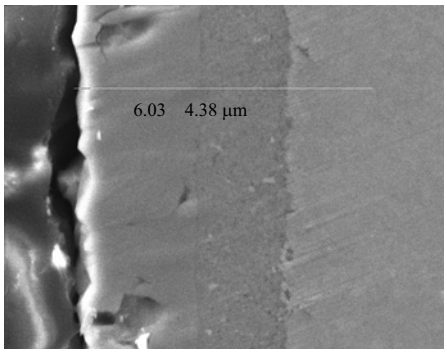

(b) HCM12A in 100 ppb DO SCW

Figure 52 Chemical composition profiles on oxide layer cross-section by using EDS analysis.

The addition of 100 ppb oxygen to the water resulted in two changes to the oxide films on both T91 and HCM12A. First, the films were about 10% thinner than in the deaerated case. Second, the stoichiometry was slightly more oxygen rich. Both of these observations are consistent with the objectives of combined water chemistry control [1,2] in which the addition of small amounts of oxygen enhance the formation of hematite crystals between the magnetite grains and reduce the oxidation rate. However, XRD measurements were made only of the outer oxide and this was only magnetite.

The glancing angle XRD technique was used in order to investigate the oxide phase on the corrosion coupons. Results from XRD agrees with chemical composition profiles of the outer oxide layer by the EDS technique. The diffraction patterns show that the outer layer is magnetite (Fe_3O_4), Figure 53. Because the penetration of X-rays from the surface ranges from 1-5 μm and the outer layer is ~5μm, this phase pertains to the outer layer only. Therefore, it can be concluded that the outer oxide structure is magnetite (Fe_3O_4).

A Perkin-Elmer model PHI 5400 XPS system was used for the XPS measurement to identify the oxide type. The data suggests the oxide types observed on T91 and HCM12A in deaerated SCW are Fe_2O_3, Fe_3O_4 and FeOOH. Since the analysis depth of XPS is from 0.5 nm to 100 nm from the surface, it is possible that there is a thin outer oxide film composed of hematite (Fe_2O_3) and The XPS analysis suggests that Fe_2O_3, Fe_3O_4 and FeOOH are present in a very thin surface layer. The analysis depth of XPS is only a few to a hundred nanometers. So it may be possible that a thin layer composed of hematite and FeOOH sits on top of the magnetite layer. The estimated thickness of this film should be the same as penetration length for X-rays.

In conclusion, results suggest the following oxide structure starting at the metal-oxide interface: metal -->$(Fe,Cr)_3O_4$ --> Fe_3O_4 + FeOOH? going from inside to outside.. The inner layer likely forms by a solid state oxidation process. The middle layer probably forms by the re-precipitation of magnetite by re-precipitation of the dissolve iron ions. This picture is similar to oxidation of T91 under steam at 575-650ºC [10].

3.2.4 400°C Tests in Deaerated SCW.

Constant extension rate tensile (CERT) tests were performed in the Multi-sample supercritical water system at 400°C. There were two types of samples in this test, (1) SCC bars: HT-9, HCM12A, T91, and T91-CSLE, and (2) corrosion coupons: HT-9, T91, and HCM12A. The system was heated up to 400°C for 20 hours before straining. The total exposure time of 151.5 hours was determined by the time to failure of the last sample. The SCC samples were strained at a strain rate of $3x10^{-7}$ s^{-1}. During exposure, the temperature inside autoclave was controlled to within ± 5°C of maintain 400°C. The pressure was maintained at 3,655 ± 15 psig. High purity water was used as test solution and the dissolved oxygen (DO) content was maintained below 10 ppb at inlet and outlet lines by purging argon gas continuously. The inlet conductivity was 0.06 μS/cm, and the outlet conductivity was 0.075 ± 0.005 μS/cm. The flow rate was maintained at around 90 ml/min.

3.2.4.1 SCC results

The stress-stain curves of the experiment in 400°C in deaerated supercritical water are shown in Figure 54 and the results are summarized in Table 14. All of samples exhibit similar work softening behavior, consistent with the experiments conducted at 500°C. The HCM12A sample failed at a strain of 10.0% and HT-9 failed at 10.6%. Both of T91 and T91-CSLE had higher ductility with failure strains of 11.2% and 12.8%, respectively.

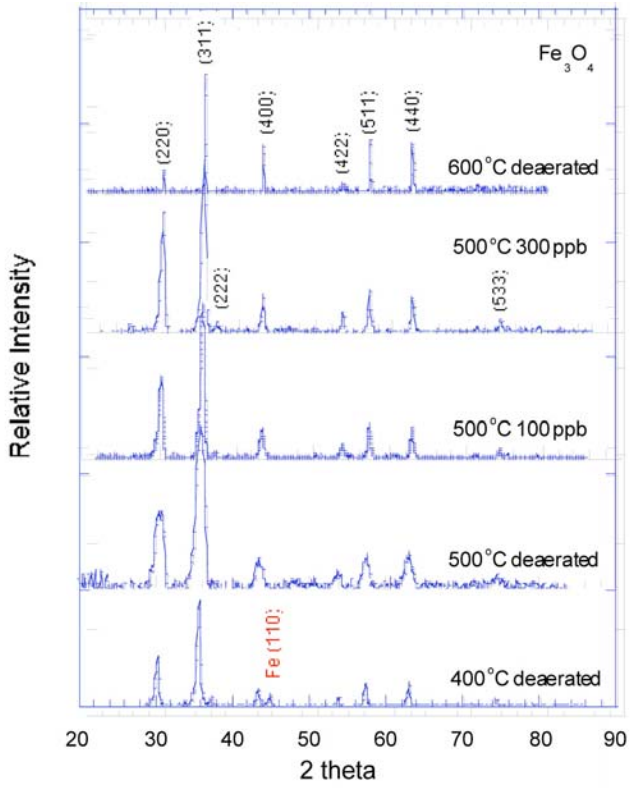

a) T91

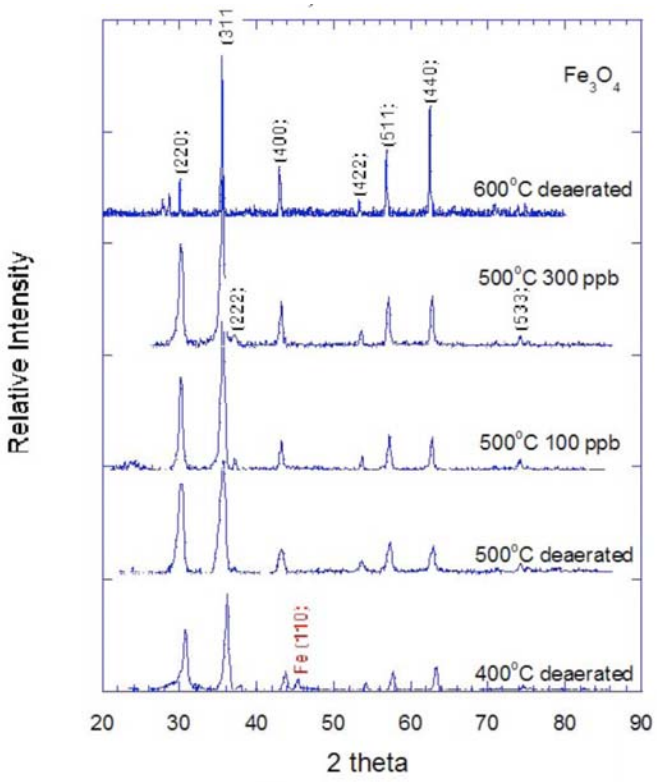

b) HCM12A

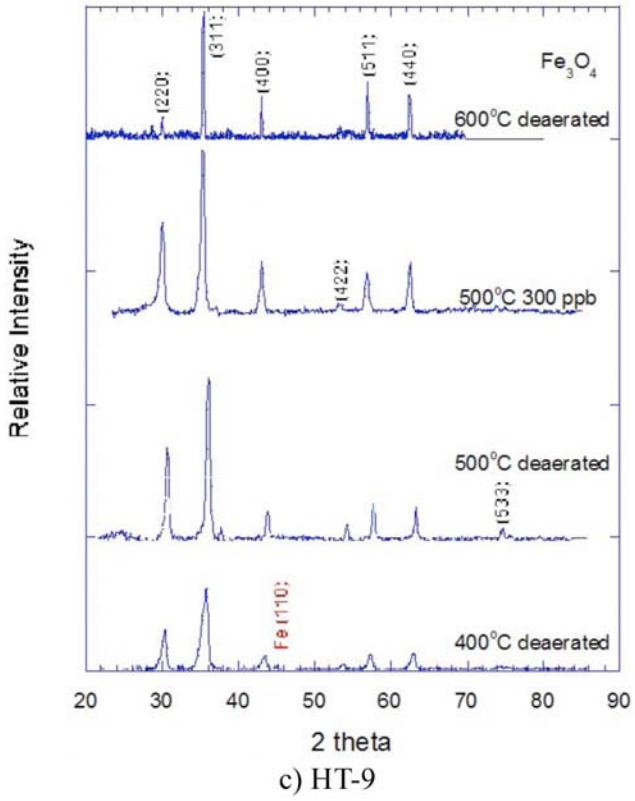

Figure 53 Glancing angle XRD spectra of the outer oxide layer of T91, HCM12A and HT-9 tested in SCW at 400°C, 500°C deaerated SCW, and at 500°C +100 ppb DO and 500°C+300 ppb DO. Spectrum of T91 at 600°C deaerated was measured by theta-2theta Philips

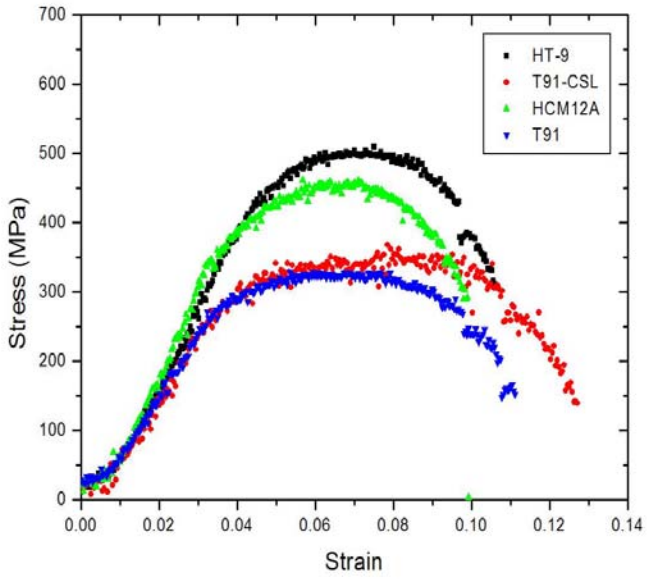

Figure 54 Stress-strain curves of HT-9, HCM12A, T91, and T91-CSLE tested in deaerated, 400°C SCW.

Table 14 Summary of the results obtained the CERT tests in 400°C deaerated SCW.

Alloys	YS (MPa)	UTS (MPa)	Elongation (%)	RA (%)	Fracture Surface
HCM12A	485	560	10.0	47.21	Ductile
HT-9	520	600	10.6	45.69	Ductile, IG
T91	380	425	11.2	68.47	Ductile
T91-CSLE	400	450	12.8	67.40	Ductile

* Because of the test facility characteristics, stress-strain curve to get real YS and UTS.

HT-9 exhibited the highest values for both YS and UTS, followed by HCM12A, T91-CSLE, and T91, respectively. The yield and ultimate strengths were greater than those measured in similar tests at 500°C. These results agree with YS values given in literatures [11-18]. As shown in Figure 55, the YS is relatively stable with temperature from 0 °C to around 400 °C, above which the YS begins to drop.

SEM investigation of SCC fracture surfaces shows typical ductile fracture in all samples. Cracking on the gage section surfaces of samples is shown in Figure 56 and the fracture surfaces of samples are shown in Figure 57. SEM investigation shows that some surface cracks on HT-9 appear to be intergranular in nature, as shown in Figure 58.

3.2.4.2 Corrosion coupons

Exposure to deaerated, 400°C SCW for 151.5 hours resulted in the formation of oxide on corrosion coupons of HT-9, HCM12A, and T91. Figure 59(a) presents the weight gain from this experiment. The values are highest in HT-9, followed by T91, and HCM12A. The weight gain rate in 400°C (151.5 hours exposure time) is much less than in 500°C (182.2 hours exposure time) as presented in Figure 59(b)

Results form X-ray diffraction (XRD) analysis show that the oxide in the outer layer of the coupon is magnetite (Fe3O4). In addition, a major peak (110) from the iron substrate was evident in the XRD patterns of each alloy. The iron peak is more clearly seen in HCM12A and T91 than in HT-9, and implies that magnetite is the only oxide present in the film. However, a cross section analysis will be performed to investigate the structure of the oxide layers in these samples.

3.2.5 500°C test in 300 ppb dissolved oxygen SCW

Constant extension rate tensile (CERT) tests were performed in the Multi-sample supercritical water system. The SCW experiment was controlled at a temperature of 500°C with a dissolved oxygen content of ~300 ppb. High purity water was used as the feed stream and the dissolved oxygen (DO) content was maintained at 320 ± 20 ppb at the autoclave inlet by bubbling argon gas containing 1.5% oxygen continuously through a water mixing column. After obtaining a stable oxygen content, the system was heated up to 500°C for 30 hours before straining. Tensile samples were strained at a strain rate of $3x10^{-7}$ s^{-1}. Three corrosion coupons of alloys HT-9, T91, and HCM12A were loaded in this test. The total exposure time of 182 hours was planned to meet the same time range of the test in 500°C deaerated SCW (182.2 hours). During exposure, the temperature inside the autoclave was controlled within ± 5°C of the target temperature of 500°C. The pressure was maintained at 24.24 ± 0.07 MPa for ~100 hours before a slightly dropped to 24.13 ± 0.07 MPa due to a problem with the pump.

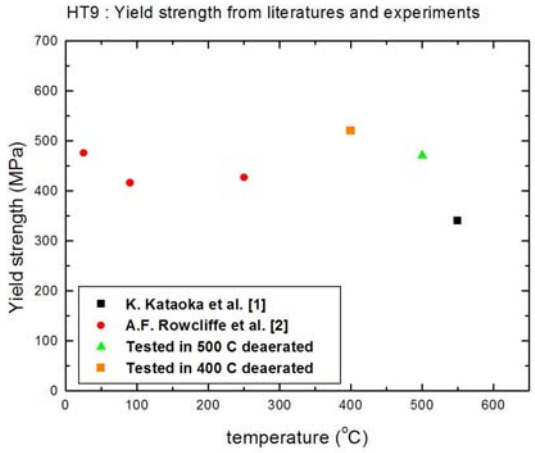

(a) HT-9

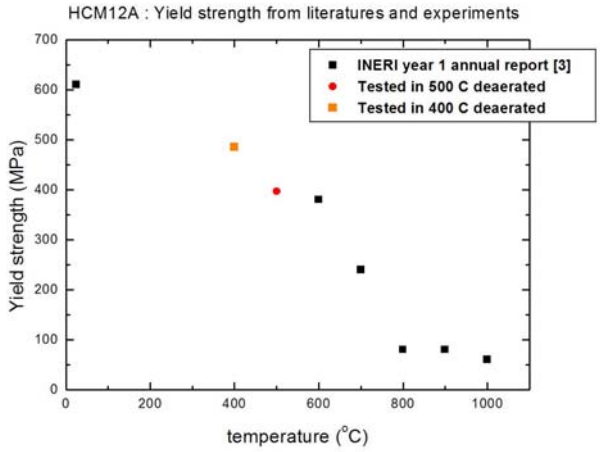

(b) HCM12A

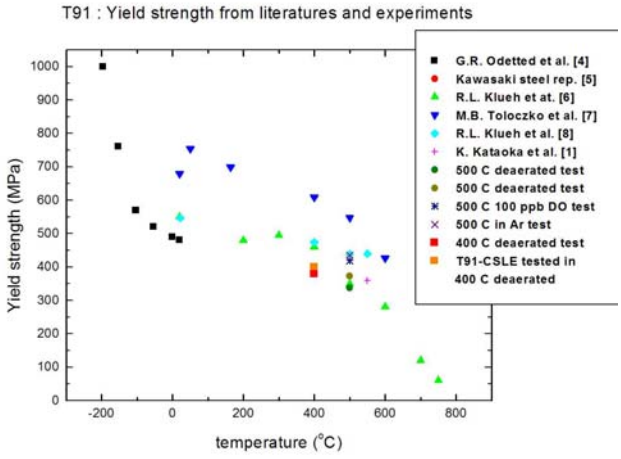

(c) T91

Figure 55 Comparison of YS at various temperatures from the literature and from our experiments.

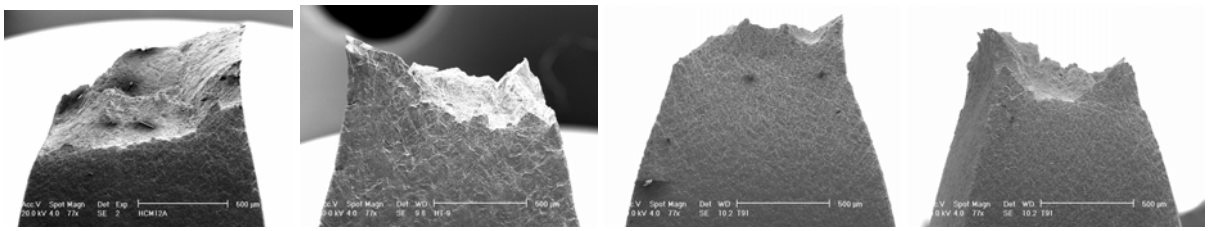

(a) HCM12A (b) HT-9 (c) T91 (d) T91-CSLE

Figure 56 SEM images of the gage section surfaces of HCM12A, HT-9, T91, and T91-CSLE tested in 400°C deaerated SCW.

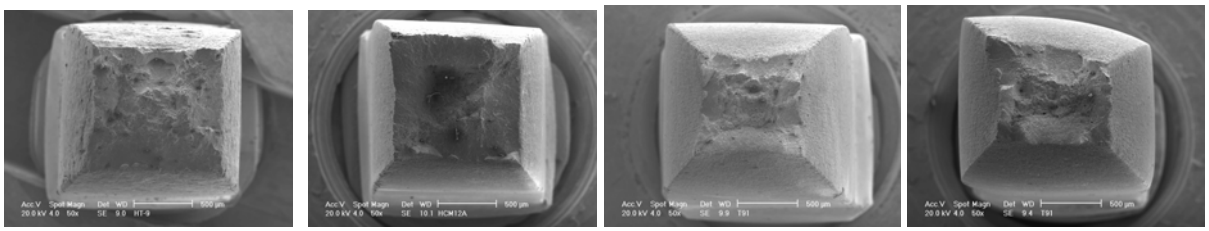

(a) HCM12A (b) HT-9 (c) T91 (d) T91-CSLE

Figure 57 SEM images of the fracture surfaces of HCM12A, HT-9, T91, and T91-CSLE tested in 400°C deaerated SCW.

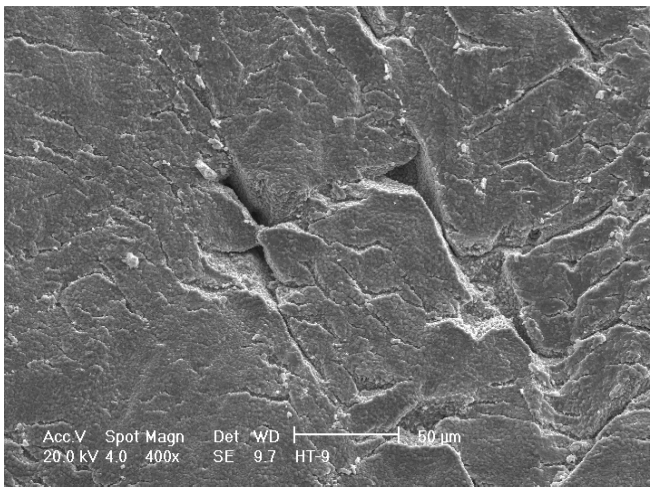

Figure 58 A crack on the HT-9 gage section surface has an intergranular appearance.

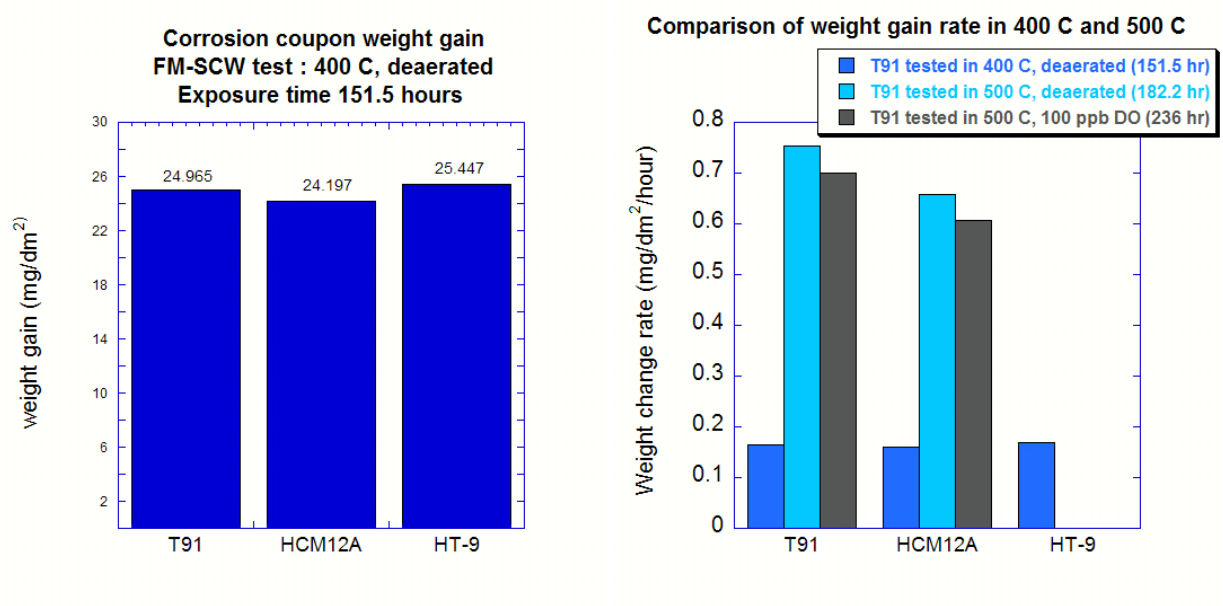

Figure 59 Comparison of weight gain of F-M alloys in supercritical water (a) 3 alloys in deaerated 400°C supercritical water (b) T91 as a function of temperature and oxygen concentration.

3.2.5.1 SCC results

The stress-stain curves of the experiment in 500°C SCW containing 300 ppb dissolved oxygen are shown in Figure 60. All of samples exhibit similar work softening behavior, consistent with the experiments conducted in 500°C deaerated SCW. The HCM12A, T91 and HT-9 sample failed at a strain of 7.95%, 11.70%, and 14.33%, respectively. T91-CSLE had the highest ductility with failure strains of 15.15%.

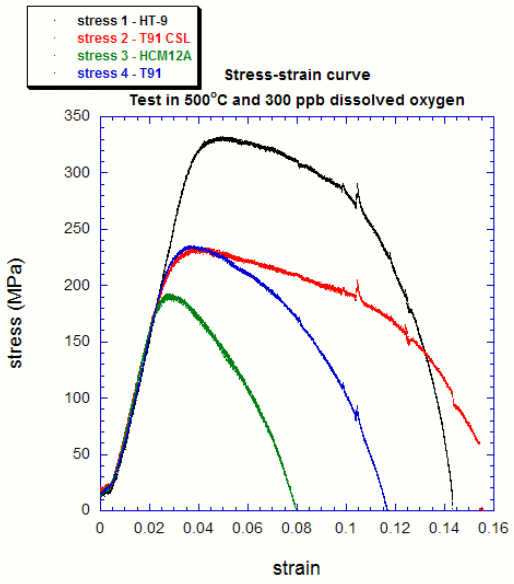

Figure 60 Stress-strain curves of HT-9, HCM12A, T91, and T91-CSLE tested in 500°C SCW containing 300 ppb DO.

The summary of YS, the maximum stress, elongation, reduction of area, and fracture mode is presented in Table 15. The results show that HT-9 exhibited the highest values for both YS and maximum stress, followed by T91, T91-CSLE, and HCM12A, respectively. In terms of elongation, T91-CSLE exhibits the highest percent elongation among the alloys. Compared to the 500°C deaerated SCW test, the yield and maximum stress are lower.

Table 15 Summary of the results obtained from CERT tests in 400°C deaerated SCW and at 500°C in deaerated SCW, 100 ppb DO, and 300 ppb DO SCW.

Test condition	Materials	YS (MPa)	Maximum stress (MPa)	Elongation (%)	RA (%)	Fracture Surface
400°C Deaerated	HT-9	520	600	10.6	45.69	Ductile,IG
	HCM12A	485	560	10.0	47.21	Ductile
	T91	380	425	11.2	68.47	Ductile
	T91 CSLE	400	450	12.8	67.40	Ductile
500°C in Ar	T91	435	470	15.0	84.8	Ductile
500°C Deaerated	HT-9	471	482	10.9	61.6	Ductile,IG
	HCM12A	397	424	12.8	74.9	Ductile
	T91 #1	338	368	16.3	78.4	Ductile
	T91 #2	373	392	12.3	79.6	Ductile
500°C 100 ppb	T91	319	341	12.8	73.2	Ductile
500°C 300 ppb	HT-9	410	430	14.33	74.1	Ductile,IG
	HCM12A	280	292	7.95	77.5	Ductile
	T91	315	335	11.70	83.7	Ductile
	T91 CSLE	317	333	15.15	74.3	Ductile

* Because of the test facility characteristics, ~ 100 MPa was added to these values to get real YS and maximum stress.

The SEM investigation of SCC fracture surfaces shows typical ductile fracture in all samples. The gauge section side surfaces near the fracture surface is shown in Figure 61 and the fracture surface images of samples are shown in Figure 62. SEM investigation shows that some surface cracks on HT-9 are intergranular in nature, as shown in Figure 63 (left). These cracks penetrate deep into alloy substrate and run at 45° to the load axis. The crack length is ~100 μm while HT-9 grain size is ~50 μm as shown in Figure 63 (right). However, since there is a thick oxide layer covering the surface, we could not confirm the intergranular nature of the cracking. Therefore, careful observation of the fracture surface was performed with cross section of gage fracture and is reported in a later section.

Cracking in HT-9 was characterized in terms of the number of cracks on the gauge length and their depth. The number of cracks on the gauge section was measured in regions of the gauge surfaces that fell into areas B and C. Crack depth was determined from cross section images such as those shown in Figure 64. The maximum crack depth was recorded as this is most important in component failure and is the

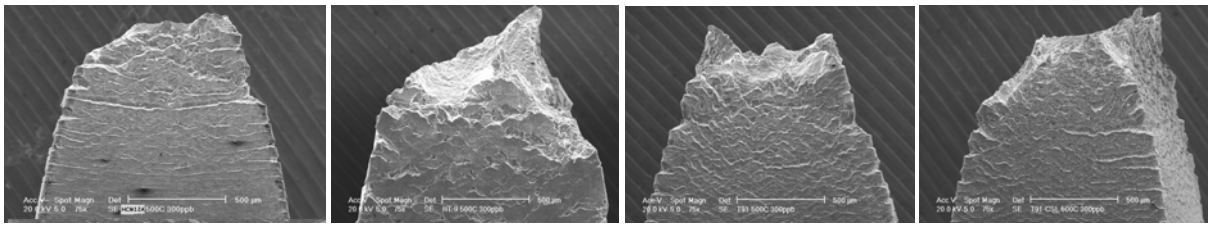

(a) HCM12A (b) HT-9 (c) T91 (d) T91-CSLE

Figure 61 SEM images of the gage section surfaces of HCM12A, HT-9, T91, and T91-CSLE tested in 500°C SCW containing 300 ppb DO.

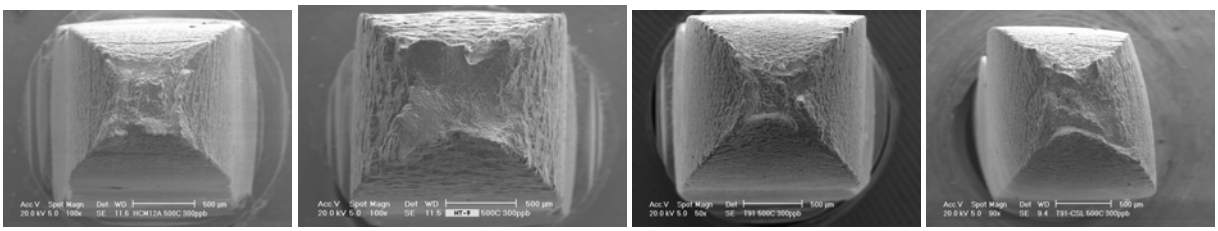

(a) HCM12A (b) HT-9 (c) T91 (d) T91-CSLE

Figure 62 SEM images of the fracture surface of HCM12A, HT-9, T91, and T91-CSLE tested in 500oC SCW containing 300 ppb DO.

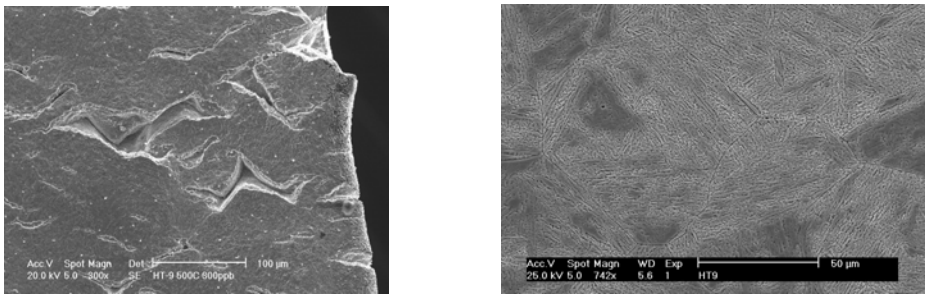

Figure 63 (left) A crack on the HT-9 gage surface (right) microstructure of HT-9.

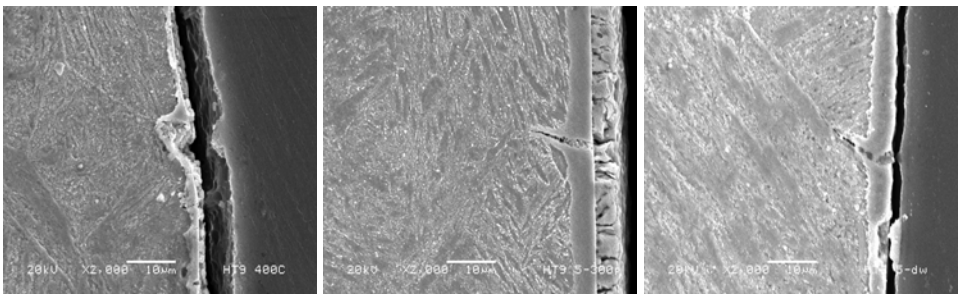

a) b) c)

Figure 64 Intergranular cracks on HT-9 SCC sample in a) 400°C deaerated, b) 500°C deaerated, and c) 500°C and 300 ppb DO.

more meaningful characterization of cracking in a small dataset. Table 16 presents total number of cracks and maximum crack depth on one side of specimen.

The number of cracks on the HT-9 specimen tested in 400°C deaerated SCW is very low (four cracks). More cracks were observed on specimens from both tests at 500°C. The number of cracks in 500°C SCW + 300 ppb DO is greater than that in 500°C deaerated SCW. As shown in Figure 64, cracking is generally intergranular, and the cracks away from the necked region appear as fairly tight cracks. The greatest crack depth was in 500°C SCW + 300 ppb DO and reaches a value of 28 μm, which is a about half the grain size. Note that both the number and depth of cracks increased with temperature and also with the amount of dissolved oxygen in the water. A summary of the SCC results in terms of crack density and depth is provided in Figure 65

Table 16 Crack analysis of unirradiated and irradiated HT-9 from CERT tests in all environments.

Test condition	Irradiation	Number of cracks	Maximum crack depth (μm)	Note
Unirradiated				
400°C DW		4	3.85	
500°C DW		18	13.08	
500°C 300 ppb		35	28.07	
Irradiated				
400°C DW	7 dpa, 500C	7	6.59	Irradiated side
400°C DW	7 dpa, 400C	11	12.7	Irradiated side

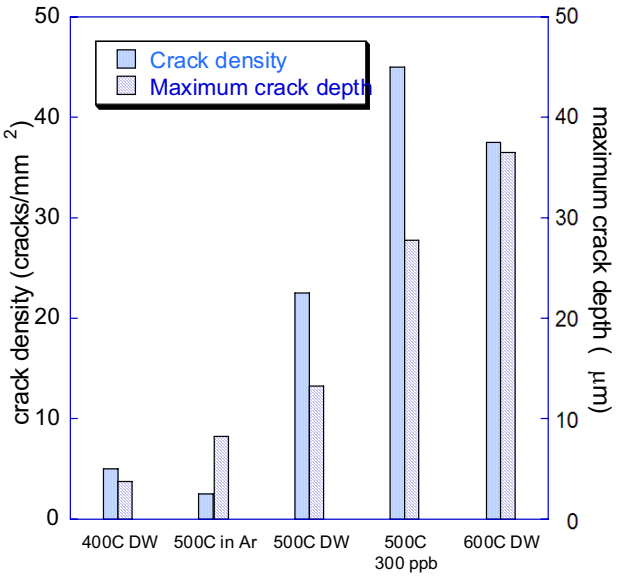

Figure 65 Summary of cracking behavior of HT-9 in supercritical water.

3.2.5.2 Corrosion coupons

Exposure in supercritical water at 500°C with 300 ppb DO for 182 hours resulted in the formation of oxide on corrosion coupons of HT-9, HCM12A, and T91. A summary of the exposure test results is listed in Table 17. Figure 66(a) presents the weight gain from this experiment. The weigh gain is highest in HT-9, followed by T91, and HCM12A. Compared to the 500°C test in deaerated and the 500°C test in SCW containing 100 ppb DO condition, the weight gain rate is highest in the deaerated test (182.2 hours exposure time), followed by the 100 ppb DO test (236 hours), and then the 300 ppb DO test (182 hours) as presented in Figure 66(b).

X-ray diffraction (XRD) analysis was performed with a glancing-angle (3 degree) X-ray diffractrometer to characterize oxide type on surface level. Results from three types of alloys indicate that the oxide in the outer layer of the coupon is magnetite (Fe_3O_4). None of these diffraction patterns

shows alloy substrate or hematite (Fe_2O_3) peaks. However, the EDS cross section analysis of these corrosion coupons will be performed to investigate the structure of the oxide layers.

Table 17 Summary of exposure tests in 400°C deaerated and in 500°C deaerated SCW, containing 100 ppb DO, and 300 ppb DO.

Temperature	DO content (ppb)	Exposure time (hours)	Alloys	Weight change (mg/dm^2)	Weight change rate ($mg/dm^2/hr$)	XRD result
400 °C	< 10 *	151.5	HT9 HCM12A T91	25.45 24.20 24.97	0.168 0.160 0.165	Fe_3O_4, Fe Fe_3O_4, Fe Fe_3O_4, Fe
500 °C	< 10*	182.2	HCM12A T91	119.94 137.30	0.658 0.754	Fe_3O_4 Fe_3O_4
500 °C	100	236	HCM12A T91	143.00 165.00	0.606 0.699	Fe_3O_4 Fe_3O_4
500 °C	300	182	HT9 HCM12A T91	126.41 105.39 115.13	0.715 0.596 0.651	Fe_3O_4 Fe_3O_4 Fe_3O_4

* deaerated condition

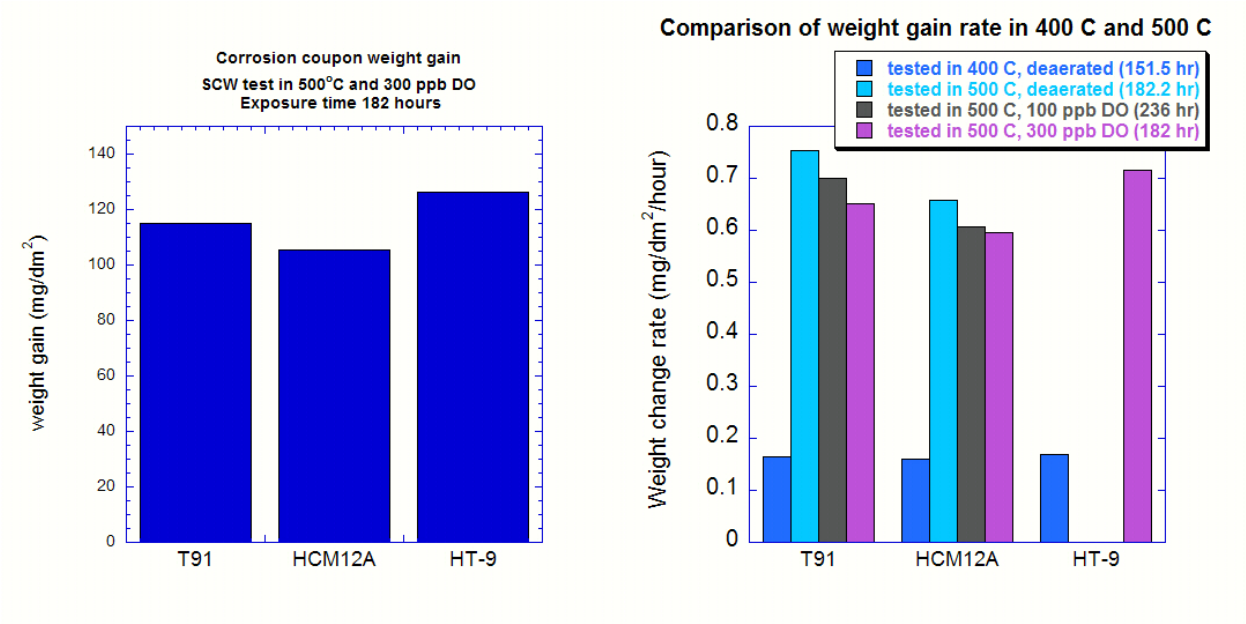

(a) (b)

Figure 66 Comparison of weight gain of F-M alloys in supercritical water (a) 3 alloys in 300ppb 500°C supercritical water (b) as a function of temperature and oxygen concentration.

3.2.6 SCC of Proton Irradiated Candidate F-M Alloys

Two CERT tests were conducted in 400°C deaerated SCW with proton-irradiated T91, HCM12A, and HT-9 samples. Proton irradiations of the F-M alloys were performed at 2 MeV and at temperature of 400°C and 500°C to doses of 3 and 7 dpa. Irradiated tensile samples were tested in the MSCW system at a strain rate of $3x10^{-7}$ s^{-1}. The stress-strain curves show increases in yield strength and maximum strength of irradiated alloys over the unirradiated condition due to the irradiation hardening effect. After the tests, cross sections of gauge fracture were carefully investigated. Results from gauge section observation reveal cracks in HT-9 that appear to be intergranular in nature. In addition, the effect of exposure time on

oxidation of F-M alloys was studied in same SCW experiments. Information of alloy types with irradiation condition and results from stress-strain curves is shown in Table 18.

Table 18 Summary of results from CERT test in 400°C deaerated SCW.

Test	Materials	Irradiation condition		Result				
		Temp (°C)	Dose (dpa)	YS (MPa)	Max. stress (MPa)	Elongation (%)	RA (%)	Fracture surface
400°C DW	T91	500	3	385	450	12.4	72.9	Ductile
	T91-CSLE	500	3	365	425	13.1	75.5	Ductile
	T91	500	7	410	470	12.5	77.5	Ductile
	HT-9	500	7	495	590	11.0	50.1	Ductile IG
400°C DW	T91	400	7	405	475	11	69.1	Ductile
	T91-CSLE	400	7	470	545	10.7	73.6	Ductile
	HCM12A	400	7	515	635	12.4	45.8	Ductile
	HT-9	400	7	520	640	10.1	34.3	Ductile IG

The engineering stress-strain curves for irradiated F-M alloys from both CERT experiments are shown in Figure 67 a) and b). All of alloys show similar work softening behavior. For both irradiation temperatures, HT-9 exhibits the highest yield strength and maximum stress, followed by HCM12A (in the test of 400°C irradiation) and T91. This trend is similar to results from unirradiated F-M alloys in 400°C and 500°C. Note that total elongations are almost the same in all F-M alloys. However HT-9 has slightly lower total elongation than that of HCM12A and T91.

SEM observation of the gauge sections of each alloy shows that fracture occurs by ductile rupture with a relatively high reduction in area (Figure 68). The reduction in area is the highest in T91 (~70-75%) and lowest on HT9 (~34-50%) which is similar to results on 400°C CERT test of unirradiated alloys. These high values of reduction in area imply an absence of stress corrosion cracking in these alloys. However, the RA value of HT-9 irradiated at 400°C (34%) is significantly less than that of unirradiated HT-9 (45%). This may be due to the presence of intergranular cracks on HT-9 that will be discussed next.

For the proton irradiated samples both the irradiated and the unirradiated sides were analyzed. Both the irradiated samples have more cracks on the irradiated side as compared to the unirradiated side thus establishing the effect of irradiation on the cracking susceptibility of HT-9. Also the sample irradiated at a lower temperature of 400°C has more cracks than the sample irradiated to the same dose at 500°C. The sample irradiated to a lower temperature of 400°C has deeper cracks as compared to the sample irradiated to the same dose at 500°C on the irradiated side. The depth of cracks on the unirradiated side for the two samples is similar to each other and to the unirradiated sample, as expected. The enhanced cracking behavior of HT-9 samples irradiated at the lower temperature of 400°C as compared to 500°C might be explained by the increased hardening at the lower irradiation temperature which causes ductility degradation. Figure 69 compares the cracking behavior in the irradiated versus unirradiated samples tested in SCW.

+

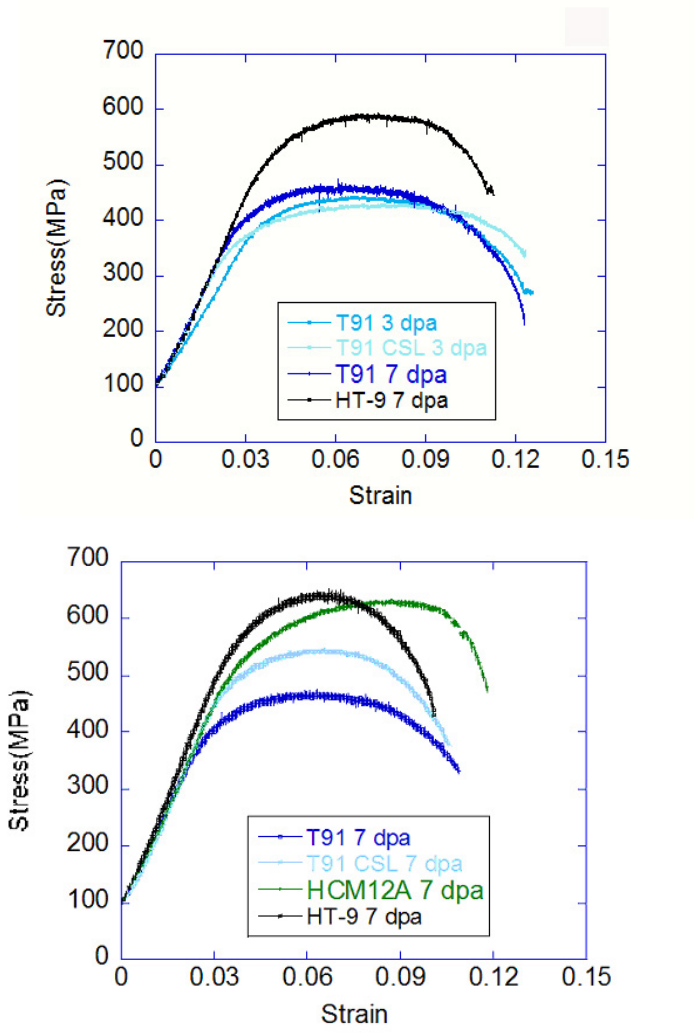

a) b)

Figure 67 Engineering stress-strain curves of irradiated F-M alloys strained in 400°C deaerated SCW, samples irradiated in 500°C with 2 MeV protons b) Engineering stress-strain curves of irradiated F-M alloys strained in 400°C deaerated SCW, samples irradiated in 400°C with 2 MeV protons.

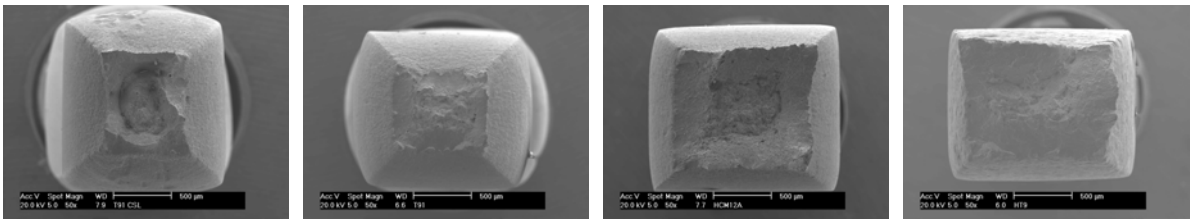

a) T91 CSLE b) T91 c) HCM12A d) HT9

Figure 68 SEM images of the fracture surfaces of F-M alloys irradiated to a dose of 7 dpa at 400°C tested in 400°C deaerated SCW.

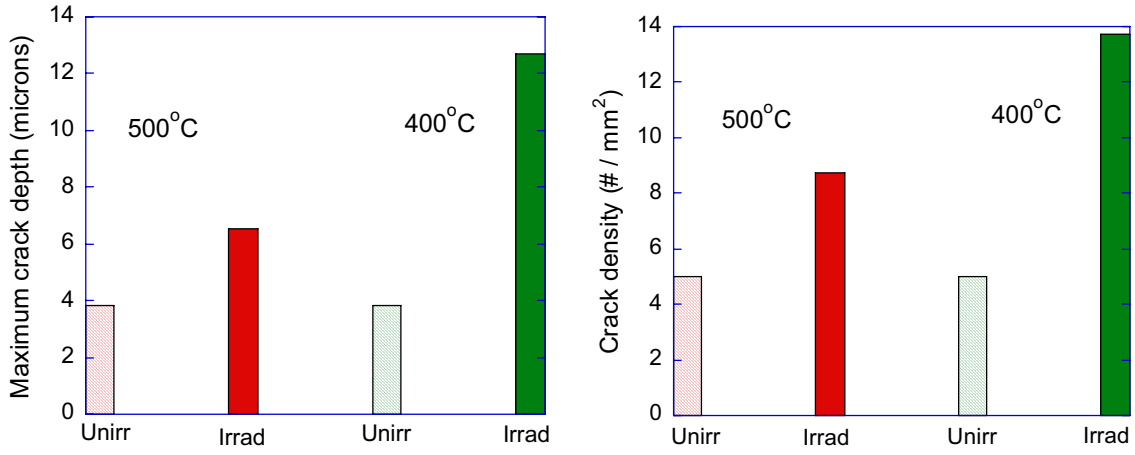

Figure 69 IG cracking in HT-9 irradiated to 7 dpa at 400°C or 500°C and tested in 400°C SCW

3.2.7 Oxide cross-sectional composition profile and surface oxide morphology

The oxidation behavior of F-M alloys in SCW at temperatures of 400 and 500°C were studied by determining the weight gain, oxide crystal structure and oxide thickness, composition and morphology. Surface analysis was performed by scanning electron microscopy (SEM) and glancing angle X-ray diffraction (XRD). The weight gain and XRD results were reported previously in project quarterly reports. Surface morphology and cross-sectional analysis of corrosion coupons are reported here. The results reported here are from tests conducted in SCW (i) at 400°C SCW and (ii) at 500°C in the deaerated condition, and at 500°C with dissolved oxygen concentrations of (iii) 100 ppb DO and (iv) 300 ppb DO. The summary of test environment and results is presented in Table 19.

In order to characterize the oxide layers, corrosion coupons were cut into two pieces, one of which was mounted in conductive filler resin and polished down to 0.05 μm with Al_2O_3 powder for SEM and energy dispersive spectroscopy (EDS) investigation of cross section of the oxide film. The other half of the sample was used for investigation of surface oxide morphology and determination of the crystal structure of the surface oxide by glancing angle XRD.

Planar images of oxides on the surfaces of exposure coupons reveal a rough and porous oxide morphology. Appendix A at the end of the section shows the oxide surfaces of T91, HCM12A and HT-9 following exposure to 400 and 500°C SCW. The morphology of the oxide formed at 500°C is significantly different from that at 400°C. The oxide formed at 400°C is granular in shape, while there is significant porosity in the oxide on specimens tested at 500°C. Note that the porosity appears to be the least in HCM12A and the greatest in HT-9, consistent with the measured weight gains.

Table 19 Summary of exposure tests in 400°C deaerated and in 500°C deaerated SCW, containing 100 ppb DO, and 300 ppb DO.

Temp.	DO (ppb)	Exposure (hours)	Alloys	Oxide layer thickness(μm)			Inner/outer thickness	Surface oxide phase**	O/M ratio***	
				Transition	Inner	Outer			Inner layer	Outer layer
400 °C	< 10*	151.5	HT9	0.65	0.83	1.21	0.69	Fe_3O_4, Fe	0.77	1.09
			HCM12A	0.40	0.85	1.14	0.75	Fe_3O_4, Fe	0.76	0.97
			T91	0.60	0.89	1.39	0.64	Fe_3O_4, Fe	0.78	1.05
500 °C	< 10*	182.2	HCM12A	1.20	4.06	5.31	0.76	Fe_3O_4	1.38	1.26
			T91	1.40	4.35	6.37	0.68	Fe_3O_4	1.33	1.38
500 °C	100	236	HCM12A	1.25	4.35	5.76	0.76	Fe_3O_4	1.44	1.39
			T91	1.50	4.45	6.65	0.67	Fe_3O_4	1.51	1.41
500 °C	300	182	HT9	2.00	3.91	5.59	0.70	Fe_3O_4	1.32	1.37
			HCM12A	1.55	3.32	4.68	0.71	Fe_3O_4	1.27	1.27
			T91	1.83	3.58	5.25	0.68	Fe_3O_4	1.30	1.29

* deaerated condition

** results from XRD [1,2,3]

*** M = Fe+Cr

The cross-section images of T91, HCM12A and HT-9 coupons exposed to 400 and 500°C SCW are presented in Appendix B at the end of the section. The SEM images show that the oxide films generally consisted of two layers, an outer oxide and an inner oxide. A transition region beneath the inner oxide where the metal content increases to bulk values and the oxygen content decreases to nearly zero was noted. The outer layer is characterized by a very rough outer surface and considerable porosity, in agreement with the planar images. The inner layer appears to be much more dense with a relatively smooth interface with the underlying alloy. The transition zone is difficult to image but appears in backscatter mode in the SEM as having a different morphology from that of the bulk metal or the inner layer. Oxide composition was determined on cross-section samples using EDS.

Line scans are shown with the SEM image for each alloy in Appendix B. The composition profiles show the oxide/metal ratios that correspond to the two oxide layers. The oxygen content is similar in both outer and inner oxide layers. The outer oxide is predominantly iron oxide whereas the inner layer contains a significant amount of chromium. The transition zone is characterized by a sharp drop in the oxygen content with distance from the inner oxide. In T91, the Mo content in the inner layer is slightly higher than in the outer layer and is closer to the bulk metal value. The same is true for Cu and W in HCM12A. Sometimes, a peak in the Cr level can be observed at the interface between the inner and outer layers.

Comparing cross-section images and composition profiles at the two temperatures reveals that the oxide layers are thinner at 400°C than at 500°C in any environment as reported in Table 1. Also, the O/M ratio is in the range of 1.33 at 500°C, consistent with a spinel, M_3O_4, but it is significantly smaller at 400°C, indicative of a high metal content in the oxide layers. From XRD results [1-3], the outer oxide layer is determined to be purely magnetite (Fe_3O_4). The O/M ratio is also slightly higher for the 500°C + 100 ppb DO case. Was and Allen [4] found that the oxide structure formed at 2000 ppb DO is similar to that at lower DO. The only difference is that an additional thin layer of hematite (Fe_2O_3) formed at 2000 ppb in addition to magnetite phase.

In summary, oxides formed in a two-layer structure in which the outer layer consisted of magnetite and was very porous with a rough exterior surface. The inner layer had a higher chromium content (metal content was approximately 2Fe:1Cr) and was much more dense than the outer layer. The stoichiometry of both oxide layers was consistent with a spinel structure. The inner layer thickness was slightly greater than the outer layer thickness and the ratio of the inner layer and outer layer thickness was greatest for HCM12A and least for HT-9, or in the same order of resistance to corrosion. Beneath the inner layer was a transition zone in which the oxygen rapidly drops to near zero, and the thickness of the transition zone depended on the temperature and DO concentration in the SCW.

3.2.8 Temperature dependence of oxidation

Figure 70 shows that oxidation in all three alloys is highly dependent on temperature in which the oxidation rate increases sharply with temperature. Figure 71 plots the log of the weight gain against 1/T to arrive at estimates for the activation energy for corrosion. The values of activation energy span the range 172 to 189 kJ/mol. In comparing these values with those for the diffusion of oxygen or iron ions through magnetite we find that they are more in line with measured activation energies for iron diffusion than for oxygen diffusion, but the measured values are still low. It is interesting to note that the activation energies in SCW are similar to those measured in steam in a similar temperature range, indicating that the mechanism of oxidation is similar. Also, the activation energies are close to those for grain boundary diffusion of oxygen in magnetite. Taken together, these results suggest that oxidation likely occurs in the following way. The outer layer forms by outward cation (iron) diffusion to the oxide-water interface. The inner layer forms by inward anion (oxygen) diffusion to the oxide-metal interface. In both cases, diffusion is aided by either porosity (outer layer) or the grain boundaries (inner layer).

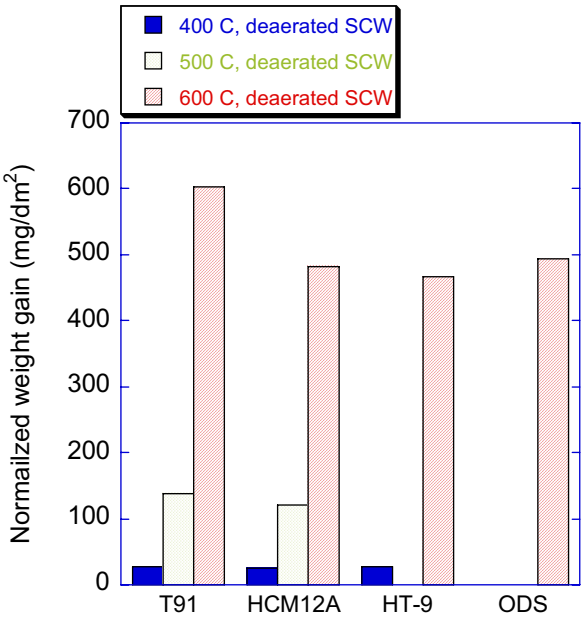

Figure 70 Temperature dependence: in Deaerated SCW for ~ 200 hr.

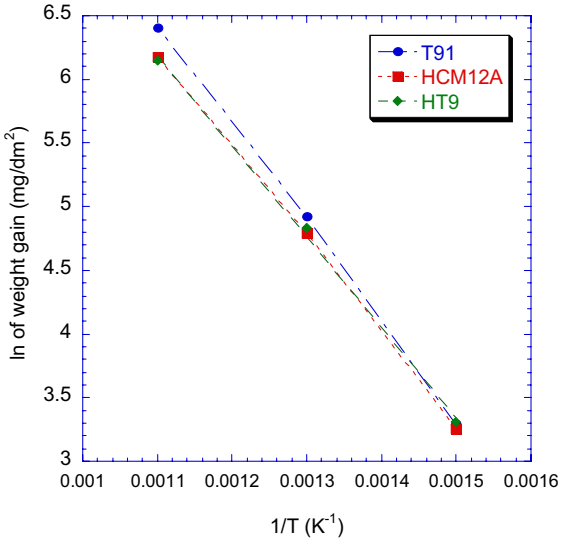

Figure 71 Temperature dependence of weight gain in ferritic-martensitic alloys.

3.2.9 HT-9 test in Ar

A constant extension rate tensile test of HT-9 was performed in Ar at 500°C in order to compare results with those obtained from tests in SCW at the same temperature. The strain rate was $3x10^{-7}$ s^{-1} and the temperature was controlled at 500 ± 2°C. The stress-strain curves from this test and other tests at 500°C show similar work softening behavior, Figure 72. The sample tested in Ar exhibits the highest reduction of area (78.5%) and failed by ductile rupture, Figure 73. The side surface shows a high density of cracks near the fracture, but there are only a few cracks in areas far from the fracture. Only two cracks were observed in the area away from the fracture surface with ~2 mm length, Figure 74. The crack density is 0.5 crack/mm^2 and maximum crack depth is 11.8 μm. In summary, the result shows that HT9 exhibits susceptibility to intergranular cracking at 500°C in an inert environment. However, the crack density is very small compared to that in SCW. [5] Therefore, the SCW environment contributes significantly to the susceptibility to intergranular cracking in HT9.

3.2.10 Summary of F-M Oxidation Behavior

Oxidation of F-M alloys in deaerated supercritical water is rapid and follows an Arrhenius behavior characterized by activation energies for corrosion of the order 172-189 kJ/mol. Addition of oxygen up to 300 ppm causes a slight decrease in the weight gain. Alloy HCM12A shows the lowest weight gain, followed by T91 and then by HT-9. In constant extension rate tensile tests, HCM12A and T91 consistently failed by ductile rupture at all temperatures. Only HT-9 exhibited IGSCC, but IG cracking was noted in all tests. The cracking is relatively shallow (<40 μm), and increased with temperature an with oxygen content of the SCW. Irradiation of the alloys to 7 dpa resulted in hardening and a dislocation loop microstructure. Tests in 400°C and 500°C SCW resulted in no IGSCC in either T91 or HCM12A. However, HT-9 exhibited IG cracking in deaerated SCW. Cracking was worse (as characterized by crack depth and crack density) for irradiations at 400°C vs. those at 500°C (and tested in 400°C water in both cases) and the difference is likely due to the greater amount of hardening at 400°C.

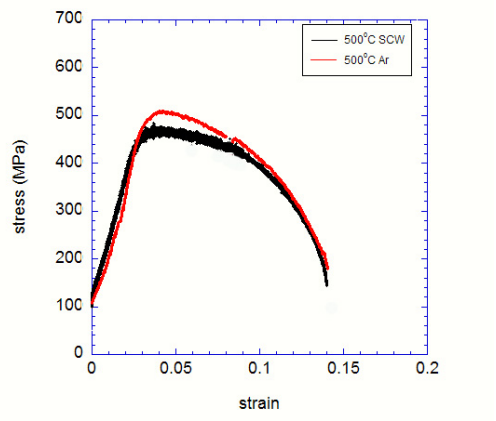

Figure 72 Stress-strain plot of HT-9 tested at 500°C in Ar and SCW.

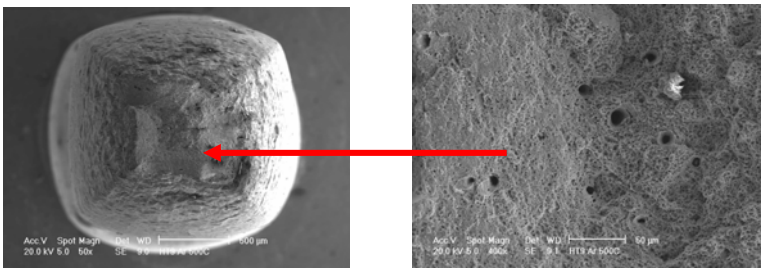

Figure 73 Gage fracture image shows ductile rupture and high reduction of area.

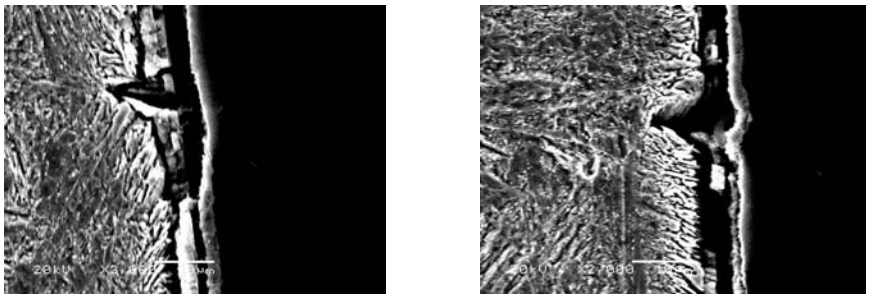

Figure 74 Cross-sectional images of gage fracture show intergranular cracks with crack length 11.6 µm and 8.3 µm.

3.2.11 References

1. Barry Dooley, B. Larkin, L. Webb, F. Pocock, and A. Bursik, "Oxygenated Treatment for Fossil Plants", IWC-92-16, proceeding of 53rd International Water Conference, Pittsburgh, Pennsylvania, Oct. 1992, p 154-161.

2. a. B. Dooley, J. Mathews, R. Pate and J. Taylor, “Optimum Chemistry for All-Ferrous Feedwater Systems: Why use an Oxygen Scavenger?”, Ultrapure Water, July/August 1995, 48-55.

3. B. B. Seth, “US Developments in Advanced Steam Turbine Materials”, Proc. of Advanced Heat Resistant Steels for Power Generation, IOM Communications Ltd., San Sebastian, Spain, 27-29 April, 1998, p.519.

4. R. L. Klueh and D. R. Harries, “Elevated-Temperature Tensile Properties of Irradiated 9Cr-1MoVNb Steel”, J. Nucl. Mater., 132 (1985) 27-31.

5. H. Naoi, M. Ohgami, Y. Hasegawa, H. Mimura, and T. Fujita, “Effects of Tungsten on Mechanical Properties and Microstructures in 9Cr-0.5Mo-W Steels”, Proc. of Advanced Heat Resistant Steels for Power Generation, IOM Communications Ltd., San Sebastian, Spain, 27-29 April, 1998, p.259.

6. Di Gianfrancesco, O. Tassa, S. Matera, and G. Cumino, “High Alloy Ferritic Steel: Mechanical and Creep Properties and its Microstructural Evolution”, Proc. of Advanced Heat Resistant Steels for Power Generation, IOM Communications Ltd., San Sebastian, Spain, 27-29 April, 1998, p.622.

7. R. L. Klueh, D. S. Gelles, S. Jitsukawa, A. Kimura, G. R. Odette, B. van der Schaaf, and M. Victoria, “Ferritic/martensitic steels-overview of recent results”, J. Nucl. Mater., 307-311 (2002) 455-465.

8. P. Fernandez, M. Hernandez-Mayoral, J. Lapena, A. M. Lancha, and G. De Diego, “Correlation between microstructure and mechanical properties of reduced activation modified F-82H ferritic martensitic steel”, Mat. Sci. Tech., Vol. 18 (2002) 1353-1362.

9. Y. Yamamoto, S. Seo, J. Mastumoto, Y. Kadoya, T. Nishimura, and R. Magoshi, “Production and Properties of Modified 9Cr-1Mo Steel Forging (F91) for Valve Bodies”, Proc. of Advanced Heat Resistant Steels for Power Generation, IOM Communications Ltd., San Sebastian, Spain, 27-29 April, 1998, p.560.

10. Dionisio Laverde et al., Continuous and cyclic oxidation of T91 ferritic steel under steam, Corrosion Science 46 (2004) 613-631.

11. K. Kataoka, et al., Proc. of ICAPP’03, Cordoba, Spain, May 4-7, 2003, paper 3258

12. A.F. Rowcliffe, et al., J. of Nucl. Mat., 258-263, 1998, p. 1275-1279

    a. NERI Year 1 annual report, originally from K. Miyata, et al. ISIJ International, 40, 2000, p. 1156

13. G.R. Odette, et al. From http://www.ms.ornl.gov/programs/fusionmatls

14. Y. Yamamoto, et al., Kawasaki Steel Technical Report, No. 25, Sept. 1991

15. R.L. Klueh, et al., “High chromium ferritic and martensitic steels for nuclear applications”, 2001, p. 122-134

16. M.B. Toloczko, et al., J. of Nucl. Mat., 318, 2003, p. 200-206

17. R.L. Klueh, et al., J. of Nucl. Mat., 132, 1985, p. 27-31

Appendix A: Surface oxide morphology

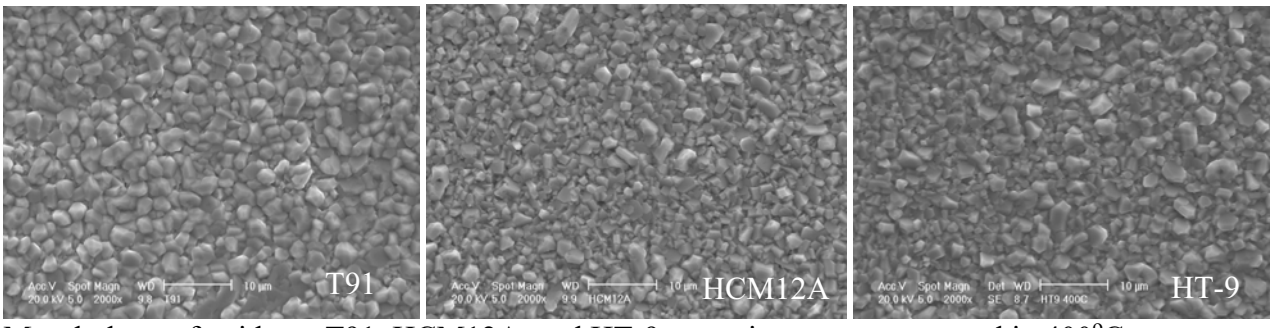

Morphology of oxide on T91, HCM12A, and HT-9 corrosion coupon exposed in 400°C deaerated for 151.5 hours

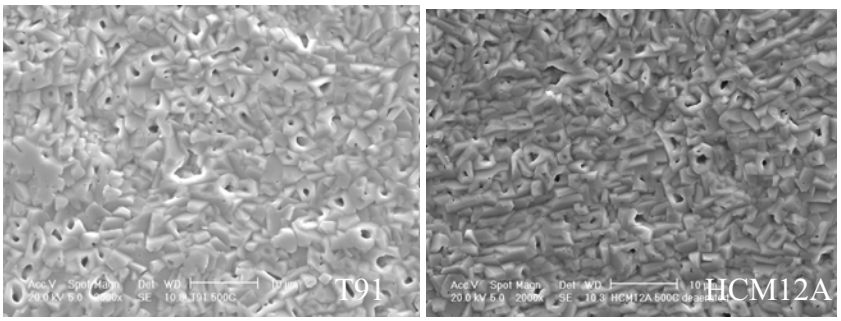

Morphology of oxide on T91 and HCM12A corrosion coupon exposed in 500°C deaerated for 182.2 hours

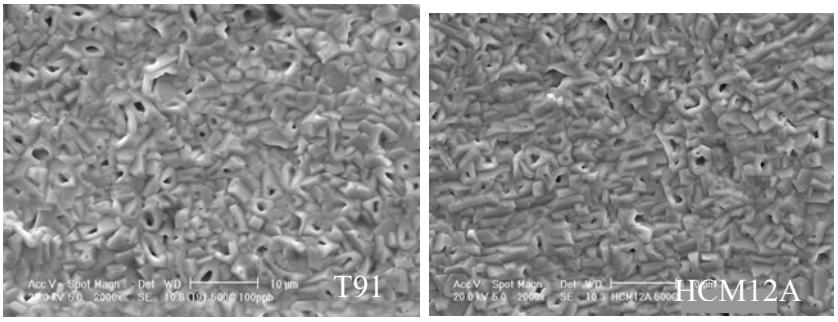

Morphology of oxide on T91, HCM12A, and HT-9 corrosion coupon exposed in 500°C 100 ppb DO for 236 hours

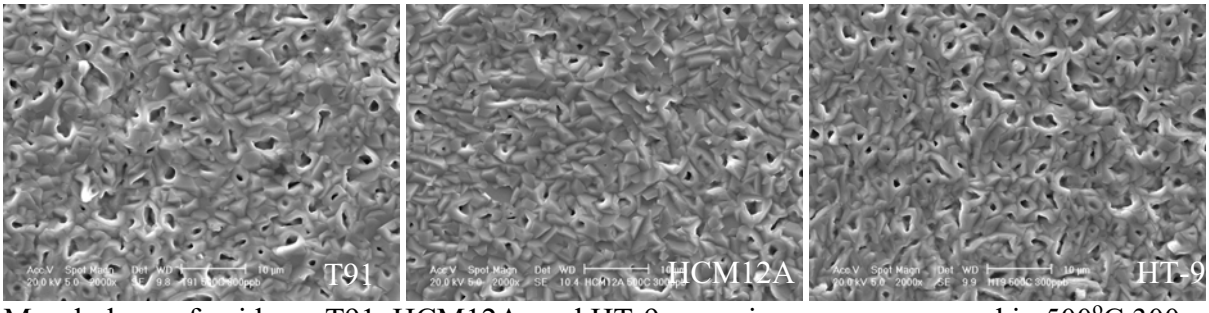

Morphology of oxide on T91, HCM12A, and HT-9 corrosion coupon exposed in 500°C 300 ppb DO for 182 hours

Appendix B : Corrosion coupon cross sectional analysis

I. Test in 400°C deaerated

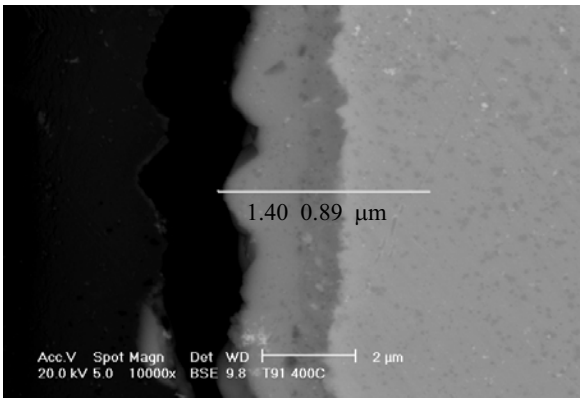

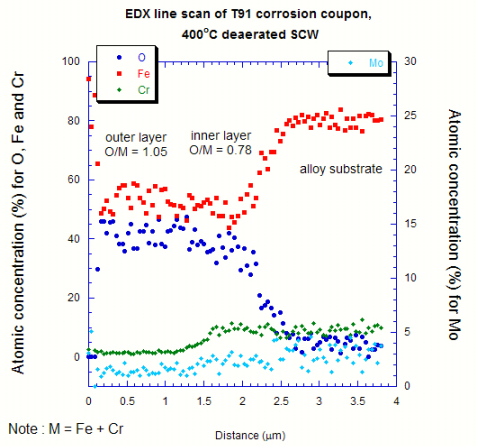

Corrosion coupon cross-section BSE image and composition profile of T91 tested in 400°C deaerated SCW, 151.5 hours.

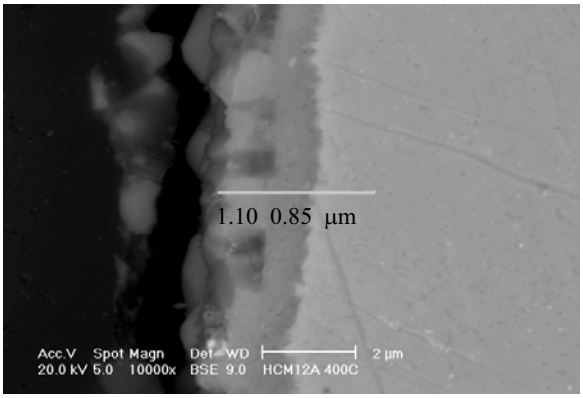

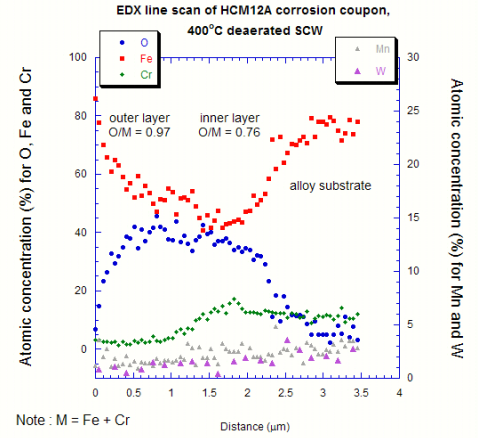

Corrosion coupon cross-section BSE image and composition profile of HCM12A tested in 400°C deaerated SCW, 151.5 hours.

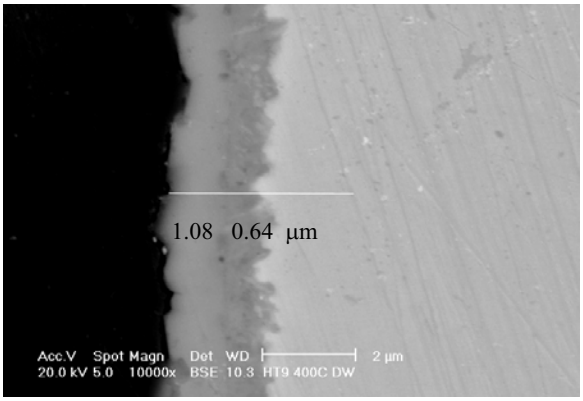

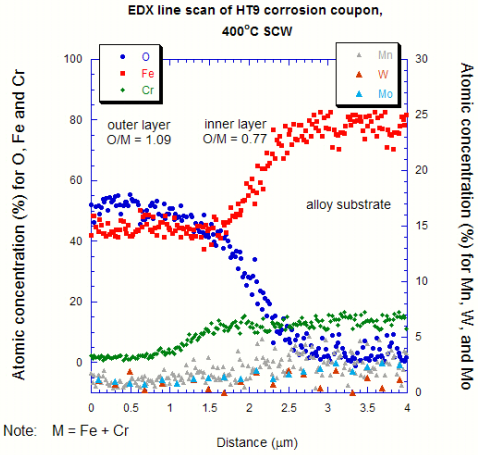

Corrosion coupon cross-section BSE image and composition profile of HT-9 tested in 400°C deaerated SCW, 151.5 hours.

II. Test in 500°C deaerated

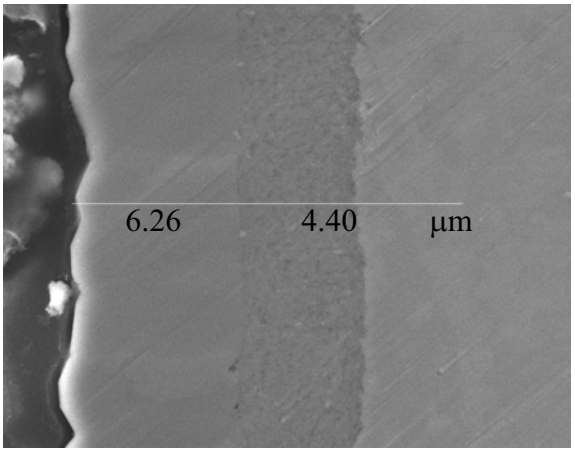

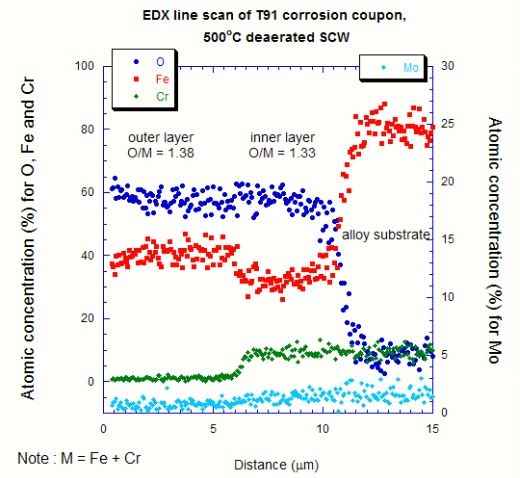

(left) Corrosion coupon cross-section image (T91 in 500°C deaerated SCW, 182.2 hours) shows two different oxide layers. (right) Composition profile from EDS line scan.

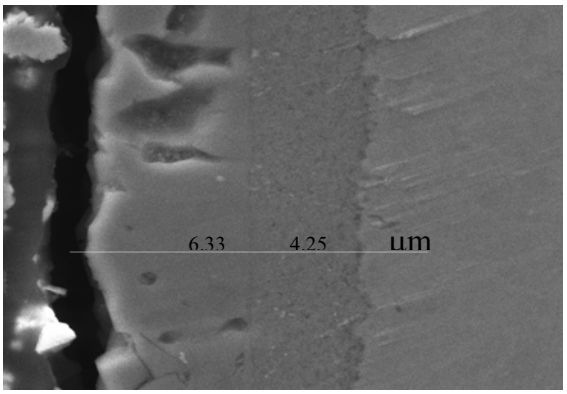

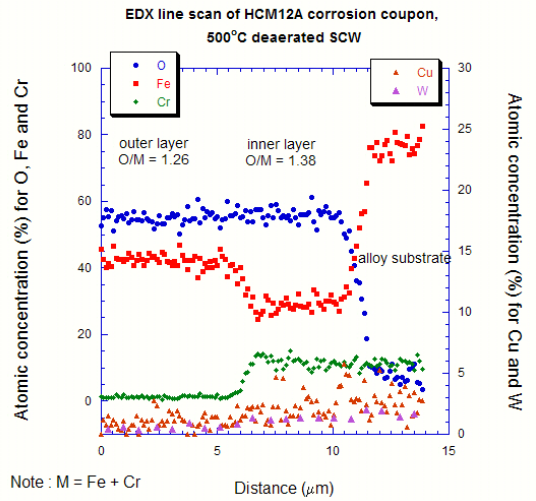

Corrosion coupon cross-section image and composition profile of HCM12A tested in 500°C deaerated SCW, 182.2 hours.

III. Test in 500°C 100 ppb

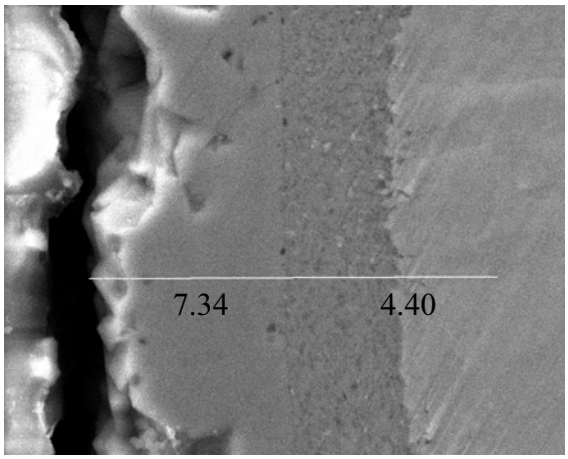

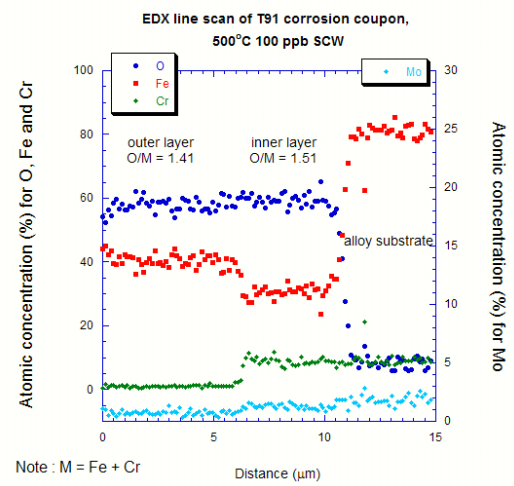

Corrosion coupon cross-section image and composition profile of T91 tested in 500°C and 100 ppb SCW, 236 hours.

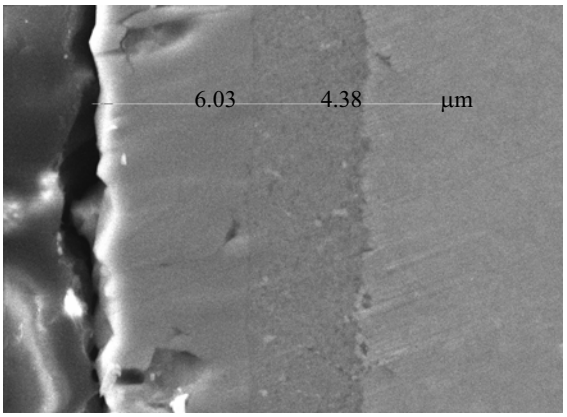

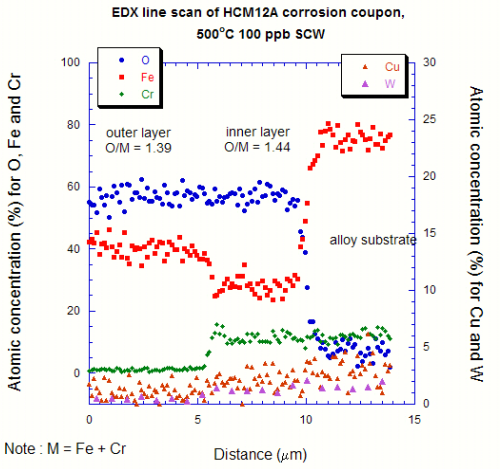

Corrosion coupon cross-section image and composition profile of HCM12A tested in 500°C and 100 ppb SCW, 236 hours.

IV. Test in 500°C 300 ppb

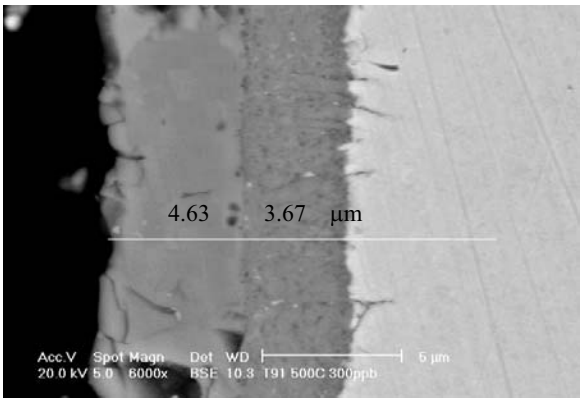

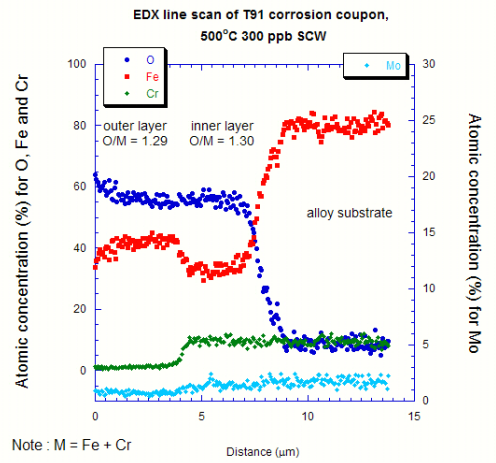

Corrosion coupon cross-section image and composition profile of T91 tested in 500°C and 300 ppb SCW, 182 hours.

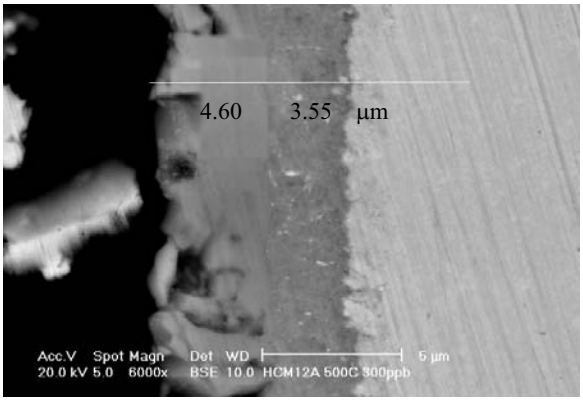

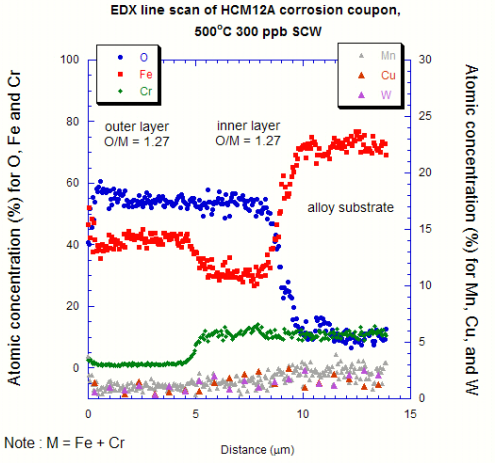

Corrosion coupon cross-section image and composition profile of HCM12A tested in 500°C and 300 ppb SCW, 182 hours.

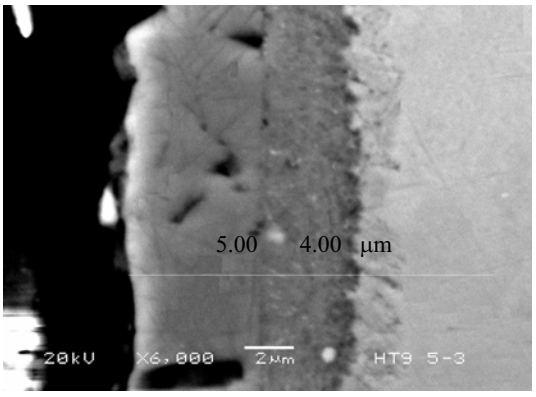

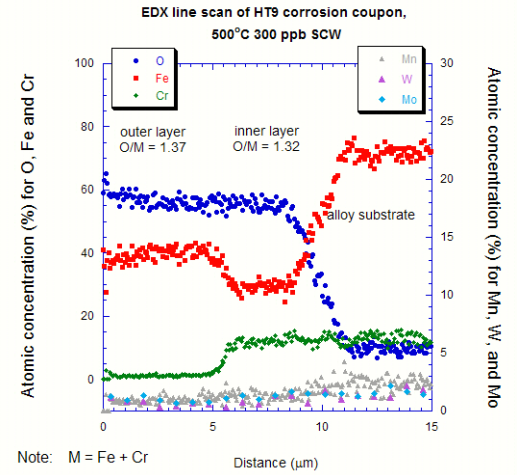

Corrosion coupon cross-section image and composition profile of HT-9 tested in 500°C and 300 ppb SCW, 182 hours.

3.3 Corrosion and SCC Studies on F-M and Ni-based Alloys

Contributor:

Jinsung Jang, KAERI

3.3.1 Supercritical Water Corrosion Test of High Cr Steels

3.3.1.1 Corrosion Oxide Characterization

Commercial grade modified 9Cr-MoVNb steel (T91) and 12CrMoVNbWCu steel HCM12A (T122)) samples were corrosion tested under SCW conditions. Chemical compositions of the specimens are the same as those listed in Table 2. After 200 hours of testing, the specimen surfaces were analyzed with XRD (X-ray Diffractometer), Grazing Incidence XRD (with 2 degree of incidence angle), and SEM (Scanning Electron Microscope) equipped with EDS (Energy Dispersive Spectrometer). Cross sections of the specimens were also investigated with SEM/EDS. Elemental mapping and line profiles were acquired from SEM/EDS and the oxide layers were investigated. Figure 75 shows SEM micrographs of the surface of T91 and HCM12A (T122) after SCW corrosion test and XRD result for the surfaces. After corrosion testing the T91 specimen, a completely different set of peaks (from oxide layer) are shown without any from matrix phase. In the case of HCM12A (T122), however, peaks from oxide layer as well as from matrix phase are shown together. Therefore the oxide layer on HCM12A (T122) specimen is assumed thin enough (at most 10 microns or less) for the x-ray information of the matrix phase to be collected together with those of the oxide layer.

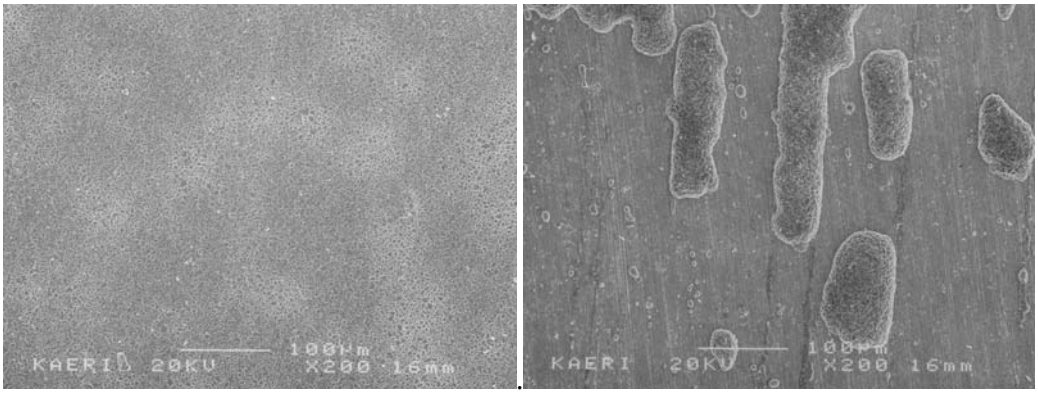

(a) (b)

Figure 75 Specimen surface of (a) T91 and (b) HCM12A (T122) after SCW corrosion test at 627 C (900 K), 25 MPa for 200 hours.

Figure 76 compares the XRD result of the oxide layer of the T91 specimen with spectra from JCPDS data of $FeCr_2O_4$ and Fe_3O_4. As shown in this figure, x-ray spectra of $FeCr_2O_4$and Fe_3O_4 are undistinguishable. From the x-ray spectra of the oxide layer on the T91 specimen it is postulated that the oxide layer on the T91 specimen was grown in a preferential orientation because there are several missing peaks and the relative intensities do not match well with those of the theoretical spectra for random powder samples.

To investigate the oxide layer in more detail the T91 specimen was investigated with Grazing Incidence XRD. The incidence angle was fixed at 2 degrees. Peaks of (220) and (422) were revealed

more clearly in the Grazing Incidence XRD and the relative intensities between two x-ray analyses were different probably due to the preferential growth of the oxide layer.

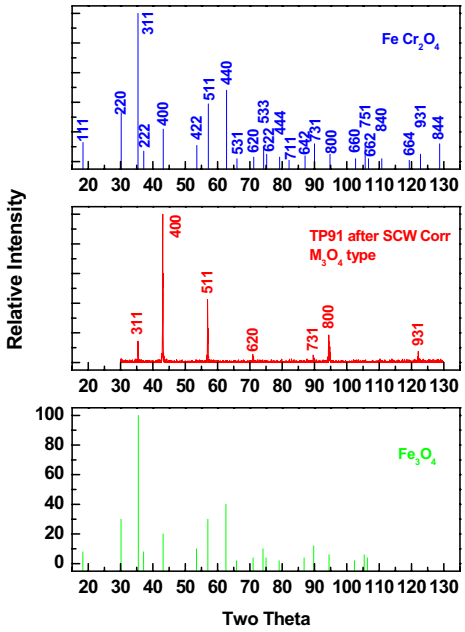

Figure 76 XRD spectra of FeCr2O4 from JCPDS data, of T91 after SCW corrosion test, and of Fe3O4 from JCPDS data.

Figure 77 shows the surface morphology of T91 specimen after corrosion test along with EDS result. The atomic ratio of Fe to O is nearly 3:4, suggesting that the surface is covered with Fe_3O_4. Figure 78 shows the SEM micrograph of HCM12A (T122) surface after corrosion test and reveals that the corrosion on HCM12A (T122) at the test temperature occurred with a nodular type of oxide formation. EDS results show that the nodular type corrosion product (area 2 and 3) matches well with the corrosion surface of T91, i.e. Fe_3O_4. The remaining area on HCM12A (T122) surface (e.g. area 1 and 4) seems to be covered with a relatively thin oxide layer. Therefore the EDS results from those areas seem to reflect the matrix phase underneath the thin oxide layer and show some amount of Cr, Mn and W.

Figure 79 shows the SEM micrographs (SEI: Secondary Electron Image and BEI: Backscattered Electron Image) of the cross section of the oxide layer of T91. Under the outermost 30 micron thick porous oxide layer, about 20 micron thick dense oxide layer is revealed, followed by another thinner (about 10 micron) oxide layer next to the matrix phase. Figure 80 illustrates the line profile of Fe, Cr, and O across the layers. The profile of the outermost porous oxide layer corresponds to that of Fe_3O_4, the profile across the underneath phase to $(Fe, Cr)_3O_4$, and the thinnest layer next to the matrix to (Fe, Cr)O. Figure 81 shows the SEM micrographs (SEI: Secondary Electron Image and BEI: Backscattered Electron Image) of the cross section of the oxide layer of HCM12A (T122). BEI shows more clearly that one micron or thinner oxide layer formed on the surface. A line profile across the layer (Figure 82) shows that it is composed of one phase and corresponds to Fe_3O_4matching with the (Grazing Incidence) XRD results.

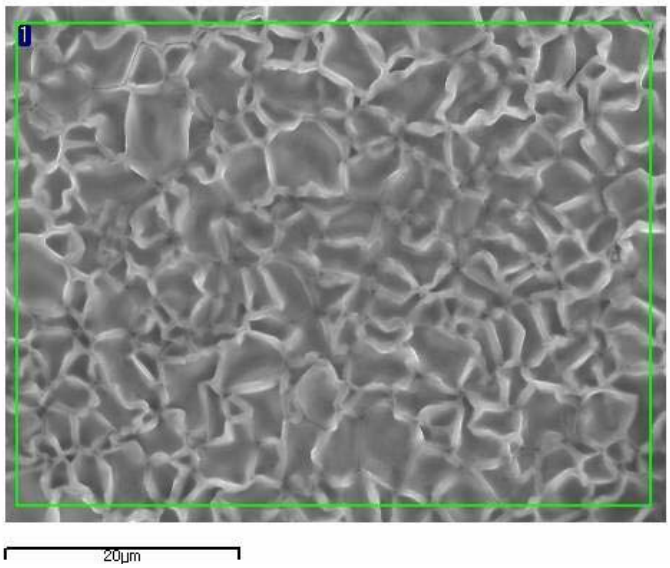

					[at%]
area	Fe	Cr	Mn	W	O
1	43.03	-	0.20	-	56.77

Figure 77 SEM micrograph and EDS result of T91 specimen after corrosion test.

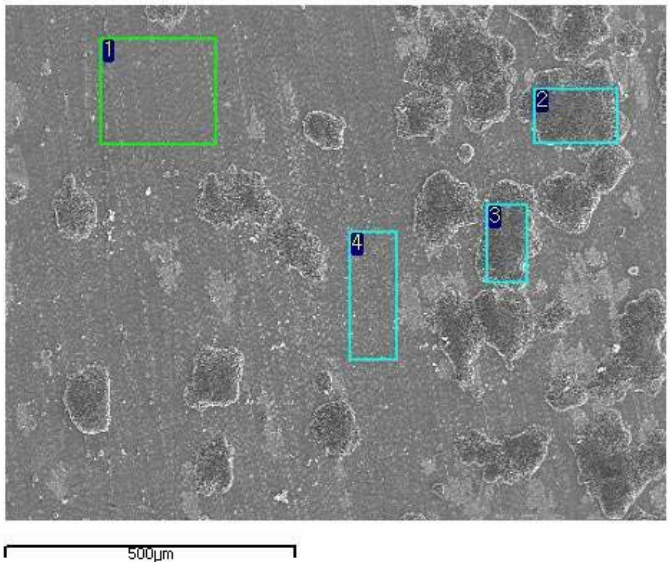

					[at %]
area	Fe	Cr	Mn	W	O
1	51.06	10.59	2.64	0.43	35.27
2	43.62	0.39	0.45	0.05	55.48
3	41.74	0.40	0.42	0.08	57.36
4	49.36	10.67	2.85	0.47	36.65

Figure 78 SEM micrograph and EDS result of HCM12A (T122) specimen after corrosion test.

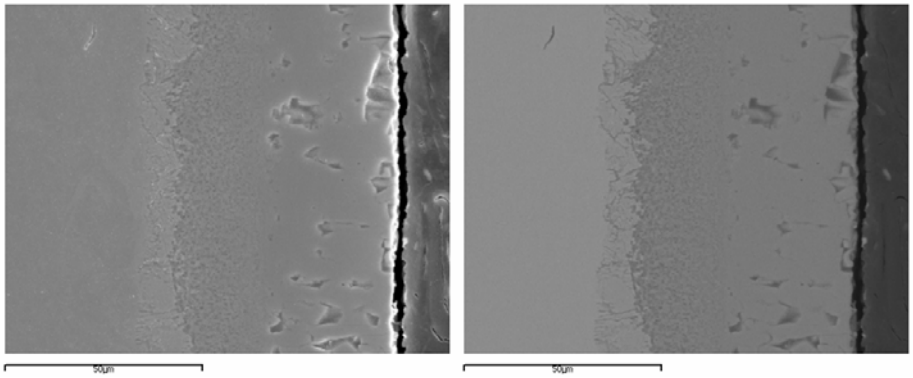

(a) (b)

Figure 79 SEM micrographs of the cross section of T91 specimen after corrosion test (a) SEI (Secondary Electron Image) (b) BEI (Backscattered Electron Image).

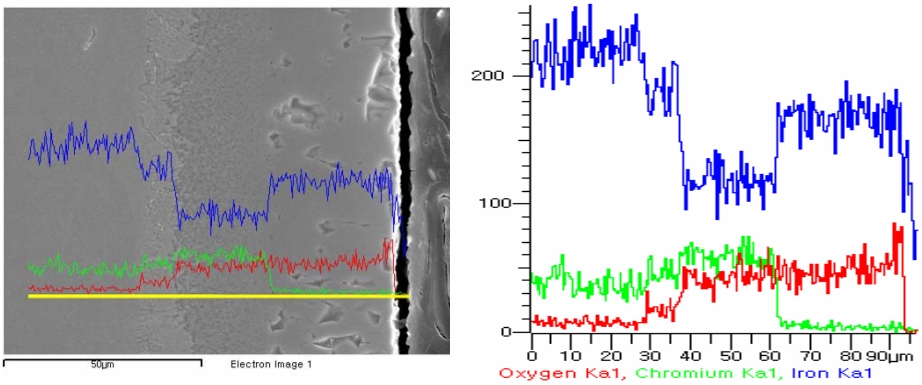

Figure 80 Line profiles of Fe, Cr, and O across the oxide layers on T91 specimen.

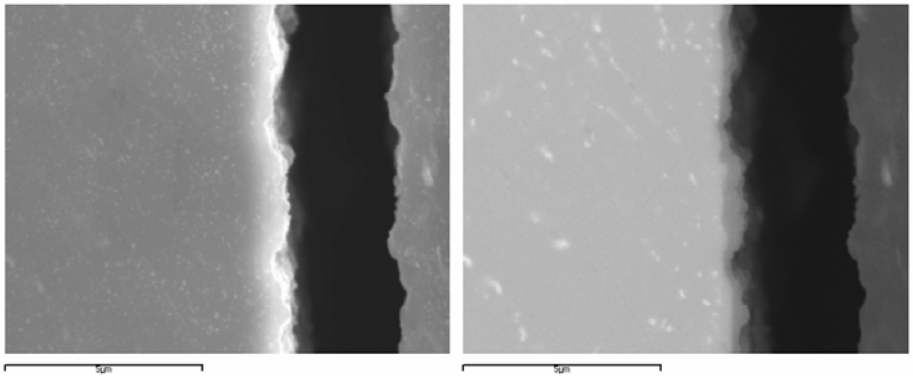

(a) (b)

Figure 81 SEM micrographs of the cross section of HCM12A (T122) specimen after corrosion test (a) SEI (Secondary Electron Image) (b) BEI (Backscattered Electron Image).

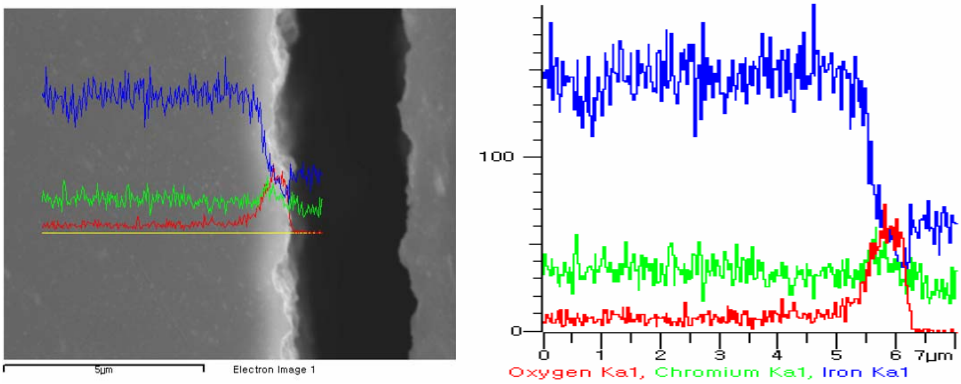

Figure 82 Line profile of Fe, Cr, and O across the oxide layers on HCM12A (T122) specimen.

3.3.1.2 Comparison of Corrosion Behavior of F-M and ODS alloys

Four commercial grade F-M steel specimens and one ODS alloy were corrosion tested in SCW. Test temperatures were 400, 450, 500, 550 and 627°C. Two specimens each with the size of 10*10*0.2 mm were corrosion tested in non-deaerated water (D.O about 8 ppm) for 100, 200, and 500 hr respectively and the results were averaged. Also a preliminary corrosion test was done in a deaerated SCW at 550°C for 217 hr. During the experiments pure nitrogen gas was purged into the water and the D.O. (dissolved oxygen) level was kept as low as 5 ppb or less. Two heats of T 91 (modified 9Cr1MoV steel) from two different manufacturers, one heat of T92, one heat of HCM12A, and one Fe-base ODS alloy (MA956) are among five specimens.

The corrosion behavior of the three 9% Cr steel specimens (two T91 and one T92) seems to be very similar. Figure 83 shows the corrosion test results of F-M steels and ODS alloy specimens in SCW. In general weight gains were increasing with the corrosion test time and the corrosion resistance was kept relatively low through all the test time up to 500 °C. But the corrosion resistance of 9% Cr steel specimens decreased at 550°C, and more severely at 627°C. Also the differences of corrosion behavior among three 9Cr steels seem to be clear and consistent and are attributed to the small variations of Cr contents, although the difference seems to be not very significant in extent. HCM12A showed clearly better corrosion resistance than 9Cr steels. However, the fluctuation of the test results is inferred due to the unstable corrosion product in this test condition. Fe-base ODS alloy containing 20% Cr (MA956) showed very high corrosion resistance in this test condition compared with other specimens.

Figure 84 shows SEM micrographs of a cross section of T91 specimen after corrosion test at 627°C for 500C hours. Three distinctive corrosion layers are distinctively revealed. The outermost layer with about 35 µm thickness has a coarse and columnar structure. The next layer of about 15 µm thickness is revealed to consist of an agglomerate of fine particles. And the innermost layer (next to the matrix) is the internally oxidized layer. Figure 85 (a) shows a cross sectional TEM micrograph of the outermost and the inner next corrosion layers. Structure analyses of SAD patterns and EDS results revealed that the outermost layer is a magnetite type Fe_3O_4, and the inner layer is composed of fine oxide particles of Fe_3O_4.

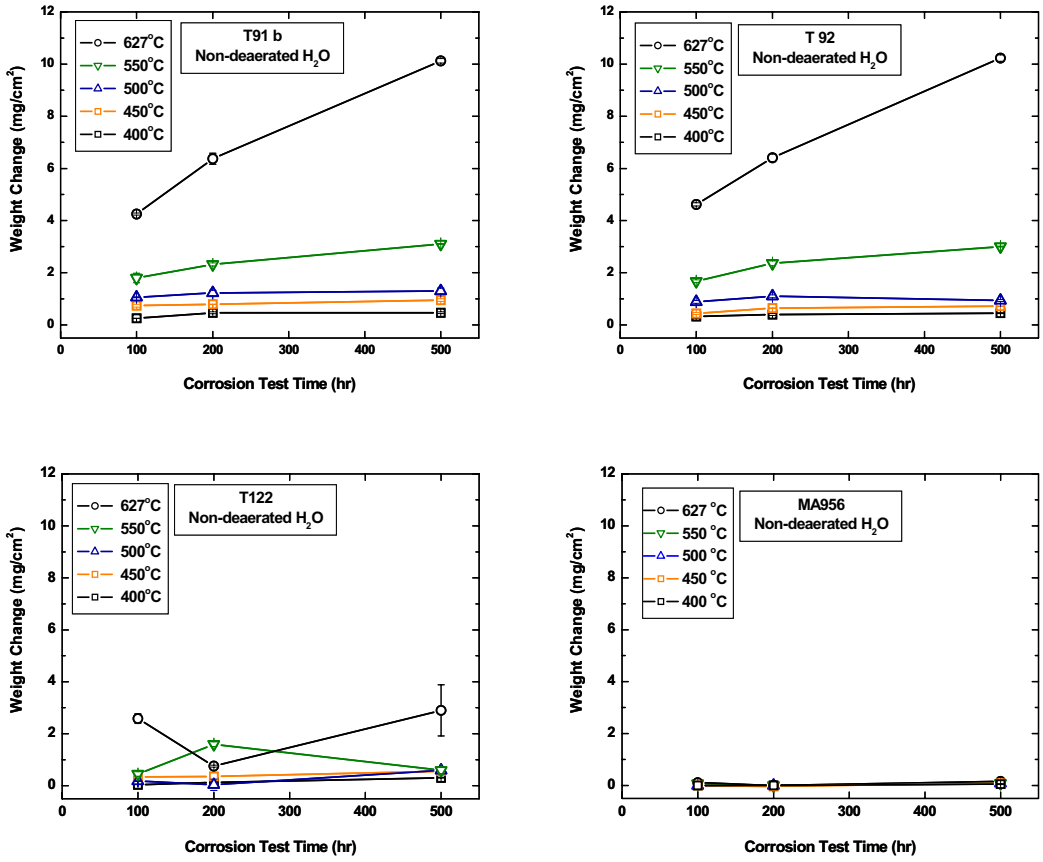

Figure 83 SCW Corrosion Test Result; High Cr Steels (T91, T92, HCM12A & MA 956).

The cross sectional TEM micrograph of the internal oxidation zone (Figure 85(b)) shows that the oxygen atoms preferentially diffused along the prior austenite boundaries and the lath boundaries and formed Fe_2O_3 and/or Fe_3O_4 phases. The internal oxidation zone was about 10 μm thick, and a thin carbide-free (precipitate-free) zone was also observed along the interface between the internal oxidation zone and the matrix phase. This is attributed to the Cr-depletion in the matrix adjacent to the internal oxidation zone and it is confirmed by the EDS analysis (no. 1 region in the Figure 85(b)).

Figure 86 show the cross section of HCM12A after the SCW corrosion test at 627°C for 500 hr. The analyses of the corrosion product by SAD and EDS revealed a magnetite type Fe_3O_4 has formed, rather than chromia phase (Cr_2O_3) that is known to form in the alloys containing more than 11% Cr. Also, the corrosion layer is observed to form locally (not uniformly) on the surface of HCM12A specimen.

3.3.1.3 Ni-base Alloys

Figure 87 shows the corrosion test results of three high Ni alloy specimens. The corrosion resistance of the three Ni-base alloys seems to be much higher, by more than one order of magnitude, than F-M steel specimens. Alloy 690 appears more corrosion resistant than the other two alloys under these test conditions.

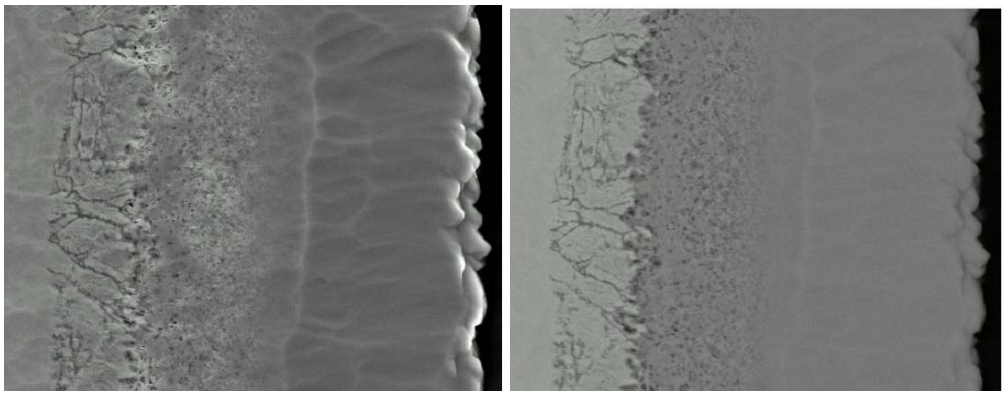

Figure 84 SEM of T91 Cross Section after SCW Corrosion Test (627 °C / 200hr).

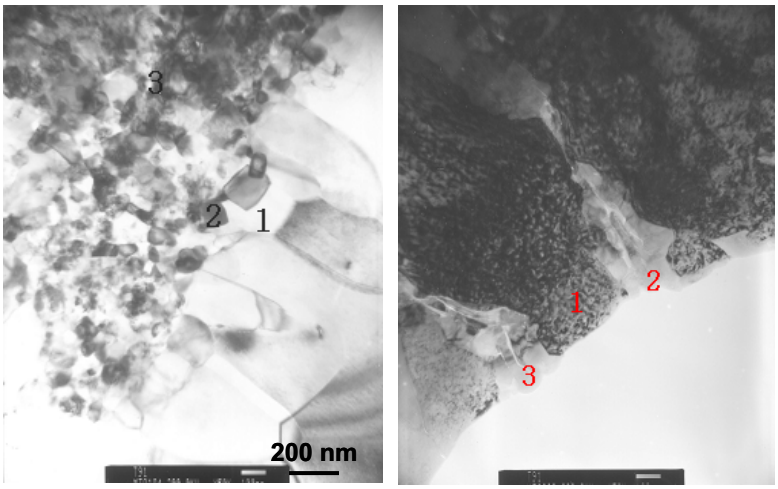

(a) (b)

Figure 85 (a) XTEM of Oxide Layers of T91 after 200 hr at 627 °C / 25MPa. (b) XTEM of Internal Oxidation Zone of T91 after 200 hr at 627 °C / 25MPa .

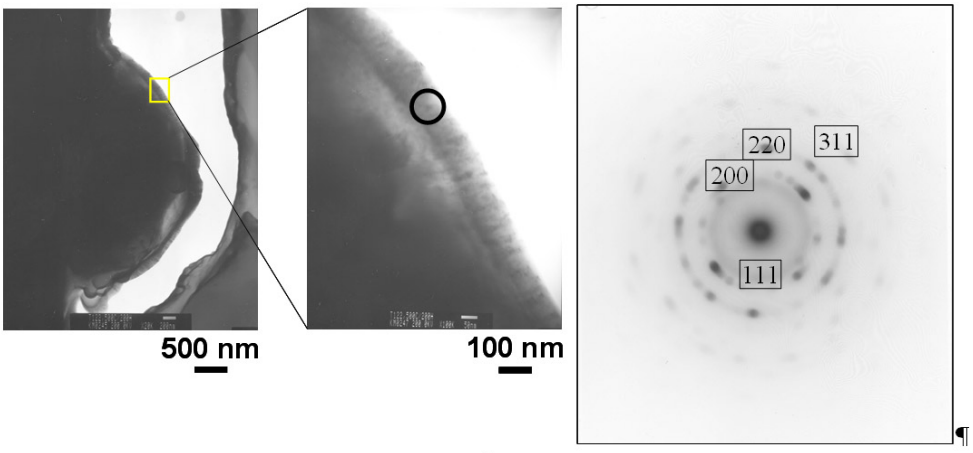

Figure 86 XTEM of Oxide Layers of HCM12A after 200 hr at 627 oC / 25MPa.

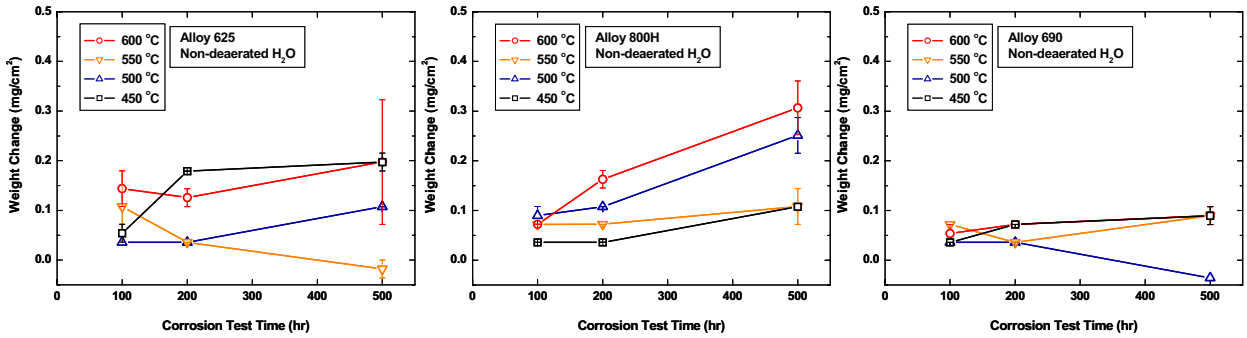

Figure 87 SCW Corrosion Test Result; high Ni Alloys (I 625, 800H, & 690).

The corrosion layers of alloy 625 and alloy 800H were revealed to be mixtures of a magnetite type $(Fe,Cr)_3O_4$ and chromia (Cr_2O_3) by grazing incidence XRD. On the other hand the corrosion layer of alloy 690 is revealed to be chromia phase without magnetite type phase, and this seems to the reason of the better and more stable corrosion behavior.

3.3.1.4 Corrosion Tests in Deaerated water

Corrosion tests with 10 by 20 by 2 mm sized coupons were carried out simultaneously with slow strain-rate tests (SSRT) or fatigue crack growth rate test in deaerated SCW at different temperatures. Inlet dissolved oxygen (D.O.) levels were maintained below 10 ppb and the conductivity levels were less than 0.1 microS. Corrosion rate normalized by test durations (mdd: mg/dm2/day) are illustrated in Figure 88. Three high Ni alloys (alloy 625, 690, and 800H) show much higher resistance to the corrosion at all conditions compared with F/M steels. As test temperature increase the corrosion rate increase (400°C/200hr vs. 500°C/200hr). And the corrosion rates in general decrease as the test times increase(500°C/200hr vs. 500°C/430hr); Corrosion rate usually tends to saturate at some extent as the corrosion duration lasts.

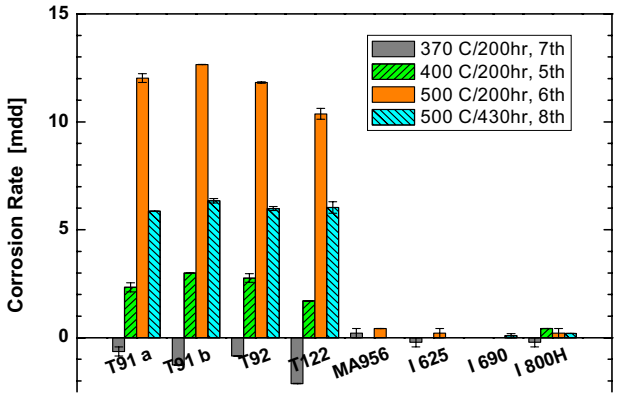

Figure 88 Corrosion test results in deaerated SCW.

However, at the sub-critical temperature (370°C just below the supercritical temperature of 374°C) the corrosion rate become negative, in other words, the specimen loses weight instead of gaining weight. The corrosion mechanism seems to have changed across this temperature range. This could be an important issue since the cladding temperature of SCWR is supposed to vary from 280 to 620 C.

3.3.2 Evaluation of SCW SCC (Stress Corrosion Cracking) of F/M Steels

One set of SCW SCC test facility was fabricated and installed at KAERI. The SCC test vessel was fabricated from Hastelloy C-276 alloy, and the design temperature and pressure are 650°C and 35 MPa respectively and the maximum flow rate is 70 cc/min. Figure 89 illustrates the schematic diagram of the facility that is composed of four parts; SCW loop, SCC test unit, control and data acquisition unit of SCW loop, and control and data acquisition unit of SCC test. Figure 90 contains photographs of the installed SCW SCC test facility under operation. One SSRT (slow strain rate test) specimen and sixteen U-bend specimens can be simultaneously tested in an experiment. Figure 91 shows an example of T91 steel specimen of which the SSRT test at 600°C was accidentally interrupted after 200 hr. Any evidence of SCC (e.g cracks on the specimen side surface) at the test condition of strain rate: $3x10^{-7}$/sec and D.O <5 ppb was not observed.

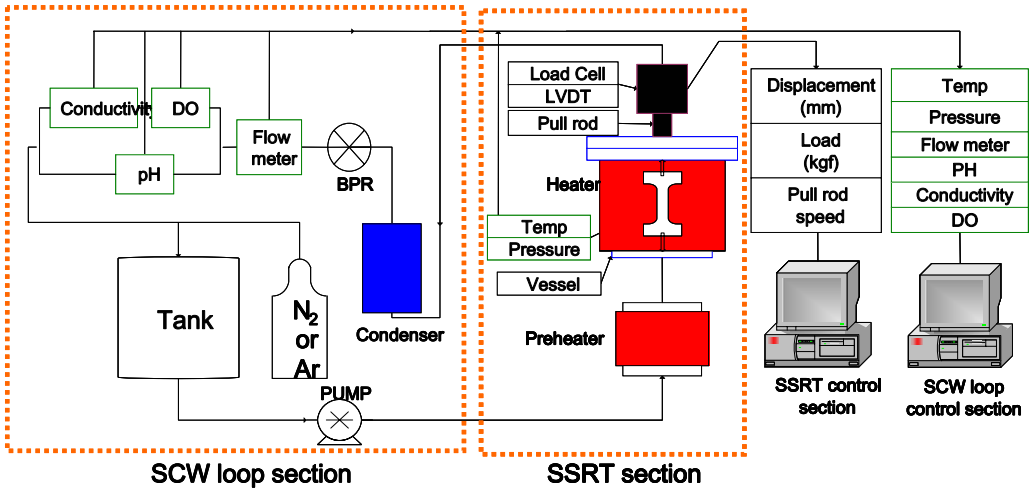

Figure 89 Schematic Diagram of SSRT Facility.

Figure 90 SCW SCC Test Loop at KAERI (1).

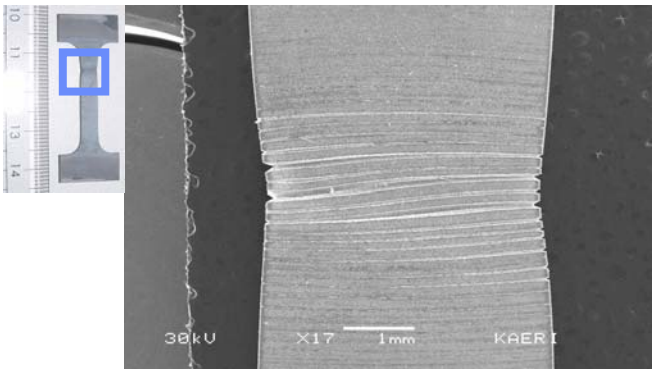

Figure 91 Feature of the T 91 tested.

SCC tests have been conducted on alloy T91 in supercritical water over a range of temperatures. The experimental details are listed in Table 20, while plots of the stress-strain curves are provided in Figure 92.

3.3.2.1 SSRT Test of T92 in SCW

A specimen tube of F-M alloy T92 tube underwent a SSRT test at a strain rate of 1.5 x 10^{-7}/sec with D.O < 10 ppb. The fracture and side surfaces of the failed sample are being investigated, but SCC does not seem to have occurred in T92 steel in the test conditions. (UTS: 398MPa; YS: 353MPa; Elongation: 21%).

3.3.2.2 Corrosion in Subcritical Water

The corrosion rate of F-M steels at 350°C (subcrtical condition) was higher than at 550°C as indicated in Figure 93. The weight change of 9Cr F/M steels in the deaerated SCW was about one half of those in the aerated SCW water. Corrosion products formed on T91 in the deaerated SCW at 500°C was similar with that in the aerated SCW at 627°C. They were composed of three layers; but the outer columnar structure contained Fe_2O rather than Fe_3O_4 in the aerated SWC an agglomerate of fine (about 10 nm in diameter) particles of $(Fe,Cr)_2O$, $(Fe,Cr)_3O_4$, and the same IOZ along the prior austenite grain and the lath boundaries. The corrosion products forming on high Ni alloy specimens in SCW at 500°C were composed of just one Cr oxide layer approximately 160nm in thickness. Compared with the total elongation of T92 at 10 ppb of dissolved oxygen level, those of T92 at 100 & 500 ppb of D.O may exhibit some stress corrosion cracking behavior, however, the fractographs did not exhibit the phenomena strongly. Stress strain curves for these tests are shown in Figure 94.

3.3.3 Corrosion Fatigue Test in Supercritical Water

Corrosion fatigue test on T91 in SCW has been conducted. Using samples with a width of 30 mm and a thickness of 6 mm, fatigue tests were performed in air and water environments according to ASTM E-657-00. Table 21 summarizes the mechanical loading conditions of the fatigue tests. Corrosion fatigue tests were performed in a SCW loop system with a C-276 vessel, where deionized water was circulating. The concentration of dissolved oxygen in the water was controlled to below 10 ppb by bubbling pure nitrogen. The electrical conductivity was held to below 0.1 micro S/cm. Test temperatures in water were 370°C and 500°C and the pressure was maintained at 25 ± 1 MPa. To prevent samples from being galvanically coupled with other metallic parts, alumina insulators were secured between the samples and the grips.

Table 20 Summary of SCC test results on alloy T91.

Test No.	Test Duration (hr)	Temp. (℃)	Strain rate (sec^{-1})	DO (ppb)	Outlet Conductivity (μs/cm)	pH	Flow rate (cc/min)
1	255	600	$3.0*10^{-7}$	< 5	30 – 140	5.3	< 5
2	217	550	$3.0*10^{-7}$	< 10	90 – 170	6.5	20 – 35
3	313	500	$1.5*10^{-7}$	< 10	10 – 40	6.5	30 – 35
4	430	500	$1.5*10^{-7}$	< 10	10 - 20	6.5	30 - 40

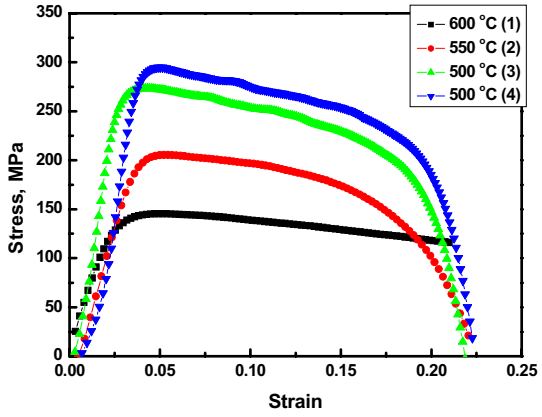

Figure 92 Four SSRT's (Slow Strain Rate Test) of T91 steel samples, one of F/M steels in deaerated SCW at 500, 550, and 600°C showed no evidence of SCC (Stress Corrosion Cracking) in the test conditions.

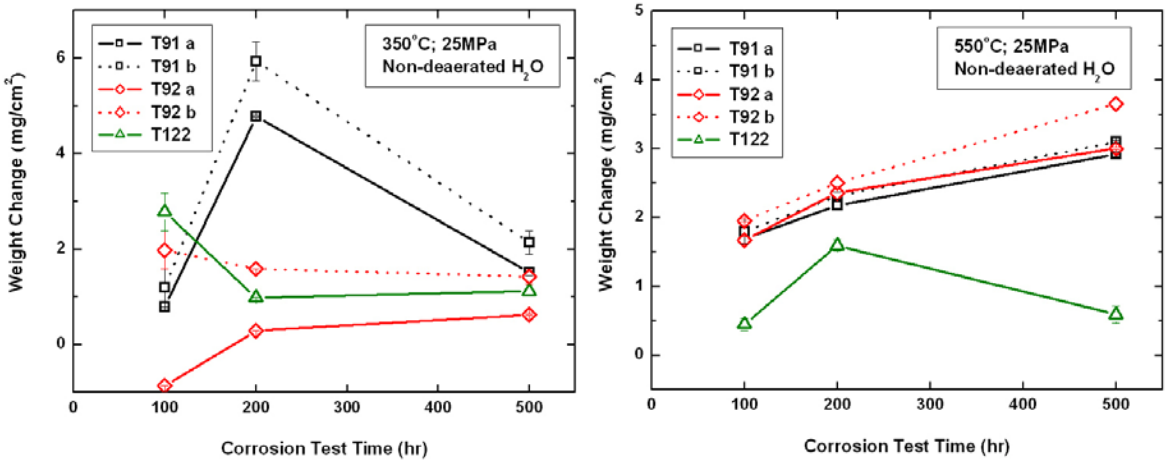

Figure 93 SCW corrosion results comparison at 350 and 550°C.

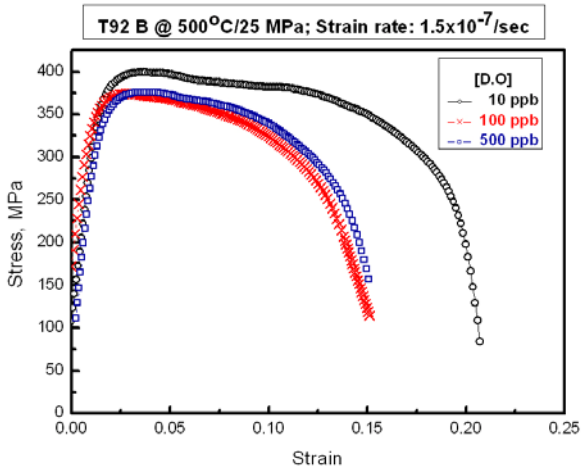

Figure 94 SCC Test Results of T92 in SCW at 500°C with Different D.O Level.Table

Table 21 Fatigue loading conditions in air and water.

Environment	air	Water
Frequency [Hz]	1	0.004 – 0.0045
R-tratio	0.1	0.12
Initial delta K [MPa $m^{1/2}$]	23-24	25

Figure 95 shows the optical micrographs of the fracture surfaces of the samples tested in air at 600°C and in supercritical water at 500°C. Using the micrographs, the fatigue crack growth rates (FCGRs) were determined. Crack lengths at five locations for each sample were measured and averaged. Figure 96, the resulting crack growth rates of T91 at 320, 370, 500, and 600°C, respectively in air were plotted as a function of stress intensity factor range (ΔK) along with those of 9Cr-1Mo steels from a literature [1]. The figure shows that the FCGRs of T91 measured in this study are comparable to the previous data. During the tests in air, the crack length was monitored using a DCPD (Direct current potential drop) technique. The results showed that there was no significant change in the FCGRs with the small ΔK change during the tests.

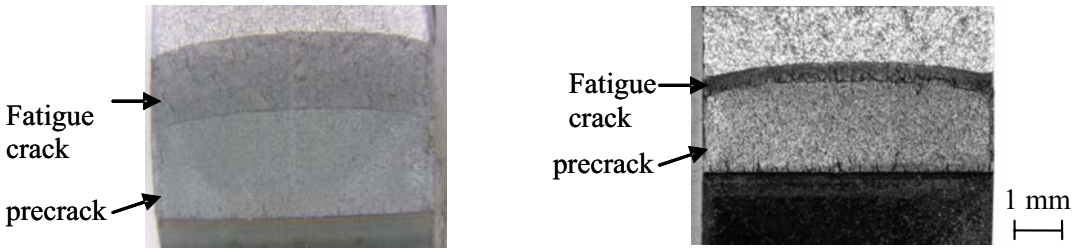

Figure 95 Optical micrographs of fracture surfaces of the samples tested in (a) air at 600°C and (b) the supercritical water at 500°C.

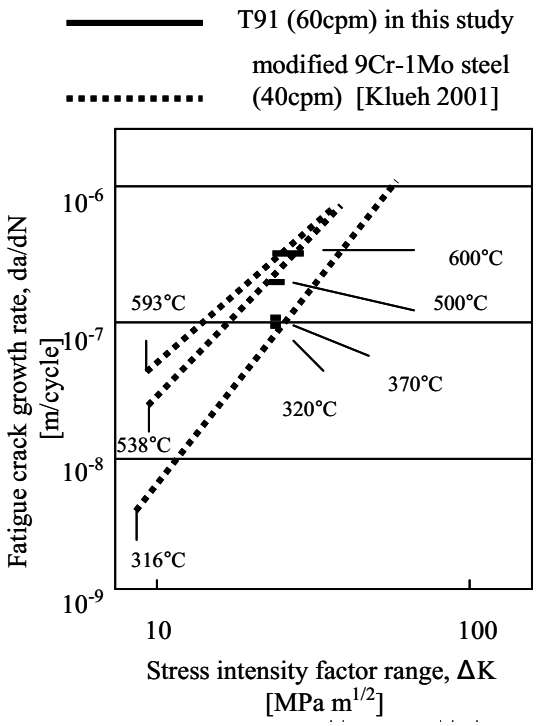

Figure 96 Comparison of fatigue crack growth rates of T91 with those of 9Cr steel from a literature.

In the water environment, corrosion fatigue tests were performed at 370°C and 500°C. It has been known that, at a temperature condition just below the critical point, corrosion rates of materials are the highest. For this reason, besides an SCW condition (500°C), 370°C was selected. During the tests, an abnormal loading, had happened several times. The plots of load versus time showed that during the cyclic loading the actual load had been held at the maximum value for several hours which might cause a pure stress corrosion cracking (SCC) condition. Therefore, the FCGRs were calculated for two cases; i) assuming that the CGRs of the corrosion fatigue and SCC are in the same range and ii) assuming that a crack did not grow by the pure SCC condition. By this, the maximum (by the latter assumption) and minimum (by the former assumption) FCGRs could be determined.

Figure 97 shows the FCGRs estimated for the two cases. In this figure, the FCGRs were plotted as a function of 1/T and compared with those in air. The FCGRs between air and water could not be quantitatively compared due to the loading problem mentioned above. However, it is evident that the FCGR of T91 increased significantly in the water conditions. As summarized by Klueh [1], a cyclic strain rate in fatigue tests has a very small effect on the fatigue behaviors of 9Cr steels below 550°C. This draws a conclusion that the increase in the FCGR in the SCW condition is due to corrosion.

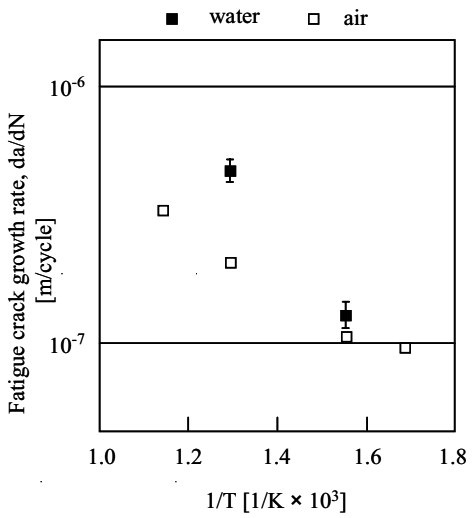

Figure 97 The Arrenius plot of da/dN vs. the reciprocal of temperature 1/T.

3.3.4 References

1. R.L. Klueh, et al., J. of Nucl. Mat., 132, 1985, p. 27-31

3.4 Supercritical Water Corrosion and Surface Modification Studies

Contributors:

Kumar Sridharan, Todd Allen, Michael Corradini, University of Wisconsin, Madison

3.4.1 Objectives

The goals of the University of Wisconsin part of the INERI project were to (i) investigate the effects of surface treatments on corrosion of candidate ferritic steels intended for use in Generation IV supercritical water (SCW) based nuclear reactors, by performing corrosion tests at SCW temperatures for various exposure times (ii) perform surface treatments of stress corrosion cracking (SCC) samples for constant extension rate tests to be performed at University of Michigan and (iii) perform materials characterization studies to understand the evolution, structure, and compositional make-up of the oxide corrosion products that form on the surface of the control and surface modified steels as a result of the SCW exposures.

3.4.2 Steels Tested and Test Conditions

The materials tested in this study were, HT9, T91, HCM12A, NF616, and ODS (oxide dispersion strengthened) ferritic steels. Compositions of these steels are listed in Table 22. Tests were performed at 500°C for exposure times of up to 3 weeks and at 600°C for exposure times of up to 6 weeks in SCW. The SCW pressure was 3650 psi and its dissolved oxygen content was 25 parts per billion (ppb).

Table 22 Composition of the ferritic steels investigated in this study.

Alloy	**Chemical Composition Wt%**																	
	C	Mn	Fe	S	Si	Cu	Ni	Cr	Al	Ti	Mo	Nb	V	W	P	B	O	N
NF616	.109	.45	Bal.	.0032	.102	—	.174	8.82	.005	—	.468	.064	.194	1.87	.012	.0017	.0042	—
T91	.1	.45	Bal.	.003	.28	.17	.21	8.37	.022	—	.9	.076	.216	—	.009	—	—	.048
HT9	.2	.6	Bal.	—	.4	—	.5	12	—	—	1	—	.25	0.5	—	—	—	—
HCM12A	.11	.6	Bal.	—	.1	1	—	12	—	—	.4	.05	.2	2	—	.003	—	.06
ODS*	.14	.05	Bal.	.003	.048	—	.06	8.60	—	.23	—	—	—	1.95	<.005	—	.14	.017

*Y_2O_3 0.28%

3.4.2.1 Surface Treatments

Two types surface treatment approaches were used to induce compositional and structural changes in the near-surface regions of the steels, (i) plasma immersion ion implantation (PIII) and (ii) sputter deposition.

3.4.2.1.1 Plasma Immersion Ion Implantation (PIII)

Plasma Immersion Ion Implantation (PIII), a technique developed at the University of Wisconsin is a non-line-of-site technique for implanting foreign elements into the near-surface regions of a material. In the PIII process, the part to be treated is immersed in a plasma in a vacuum chamber and pulse-biased to a

high negative potential. As a result of this negative voltage pulse bias, the electrons in the plasma are repelled away from the part, leaving behind a conformal ion-rich sheath around the sample surface. The ions are accelerated across this sheath at high velocities, normal towards the surface of the part. At high voltage biases and low pressures (~0.5mTorr), the ions acquire enough energy to get implanted into the near-surface regions of the material. The depth of the implanted region is quite shallow, typically 0.2μm. However, the dramatic changes in the near-surface chemistry and structure resulting from ion implantation have been shown to improve wear and corrosion resistance of materials. While this research was performed on flat test samples and SCC samples, the PIII process is inherently non-line-of-sight in nature and allows for uniform ion implantation of three-dimensional parts as well as simultaneous surface treatment of a number of parts. Figure 98 schematically illustrates the PIII process. All implantations for this study were carried out at about 40 kV to a dose of 3 x 10^{17} ions/cm^2 at room temperature. Figure 99 shows an example of on-line diagnostic display that shows instantaneous voltage, instantaneous current, and integrated current during a single pulse, taken during a surface modification run for this project. O^+ species was selected as the implant species, based on promising results from initial studies.

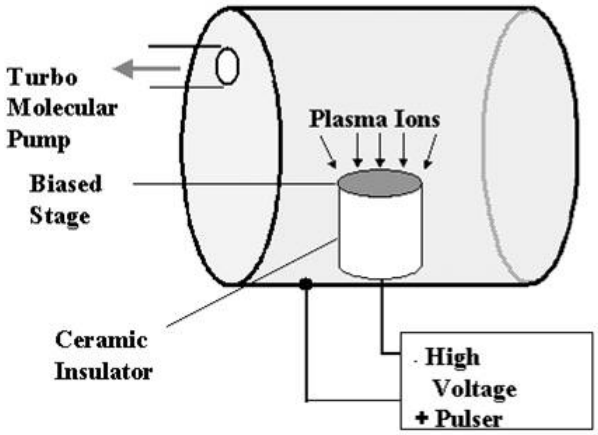

Figure 98 Schematic illustration of the plasma immersion ion implantation (PIII) process used at the University of Wisconsin for surface modification of steels.

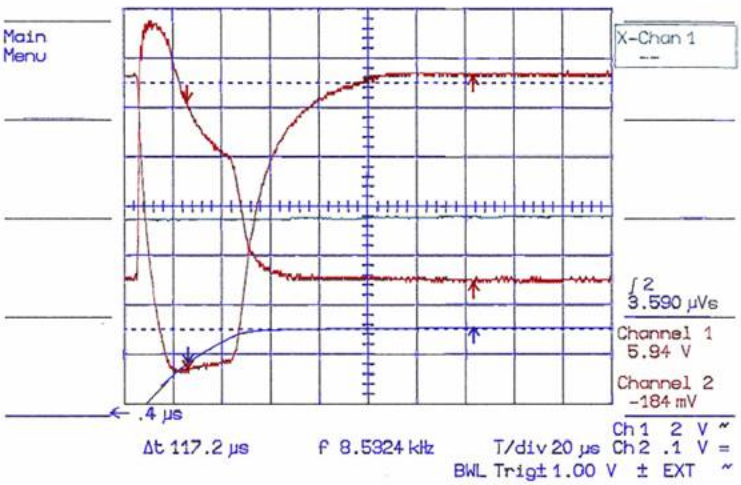

Figure 99 Typical instantaneous voltage and current and integrated current during a single pulse taken during the oxygen ion implantation run of ferritic steels.

3.4.2.1.2 Sputter Deposition:

In addition to the above implantations, sputter deposition of a thin film of oxidation resistant material was also investigated as a method for changing the near-surface chemistry of the steels. Sputter deposition was carried out in a commercial Denton sputter system and the thickness of the films deposited was about 1μm. Yttrium was selected as film material of choice based upon its ability to form a stable, tenacious oxide on the surface. In addition, a combination of sputter deposition and ion bombardment was also investigated. Here sputter deposited films were subjected to a separate ion bombardment step with Xe^{+} ions using the PIII process. The objective of this bombardment step was to induce mixing between the film and the underlying substrate in order to improve film adhesion and, if possible, achieve alloying between the yttrium film and the underlying alloy substrate. The expectation here was that immediately upon exposure to elevated temperatures, yttrium would form its own stable protective oxide, which would be eventually incorporated into the growing Fe-Cr oxide during longer exposures. Both these effects are expected to be beneficial to oxidation resistance.

3.4.2.2 Supercritical Water Testing:

Supercritical water testing was performed in two facilities at the University of Wisconsin. During the first phase (500°C tests) of this INERI project, tests were performed in the SCW corrosion loop with a supercritical water maximum velocity of about 1m/s. Since this facility was also used for thermal hydraulics and heat transfer research, a separate SCW corrosion test cell dedicated to materials and corrosion research was built. The second phase of testing (600°C tests) was performed in this corrosion cell. Both systems are equipped for continuous on-line monitoring of temperature, pressure, conductivity, and oxygen content during the supercritical water tests. Figure 100 shows a photograph of the SCW corrosion test facility used for the second phase of this project. Figure 101 shows the fixturing of the samples in the Inconel 625 holder with the test steel samples.

Figure 100 Supercritical water corrosion cell at the University of Wisconsin, used for the 600oC SCW corrosion tests.

Figure 101 Inconel 625 holder used for fixturing the samples in the SCW corrosion cell. The test samples were 1.25" in length, 0.5" in width, and about 0.02" in thickness.

Figure 102, Figure 103, Figure 104, and Figure 105 show the typical output for temperature, oxygen content, pressure, and conductivity taken during the 192 hours test carried out at 500°C. The exposure time was taken as the time of residence at the operating temperature and pressure.

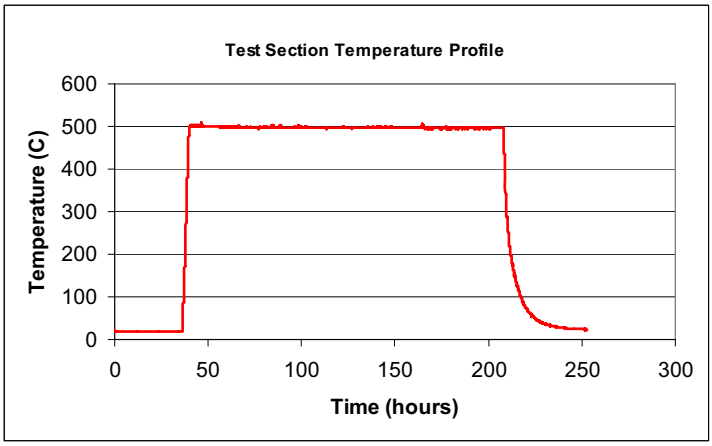

Figure 102 Temperature profile during the 192 hours supercritical water corrosion test at 500°C.

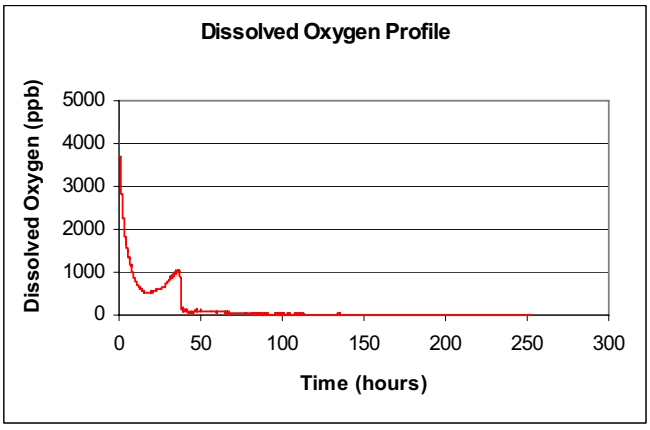

Figure 103 Dissolved oxygen content during the 192 hours supercritical water corrosion test at 500°C.

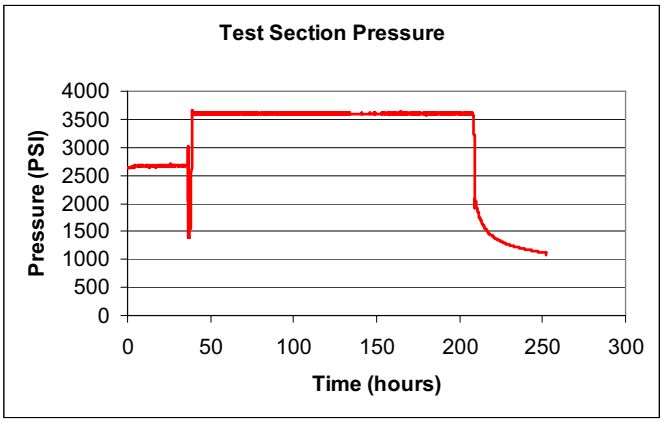

Figure 104 Test section pressure during supercritical water corrosion test at 500°C. The loop was operating with room temperature water at about 2600 psi to pump through the oxygen control system to condition the water prior to heating. The dip in the curve at about 50 hours corresponds to the start of heat up and the increase in pressure due to the density change.

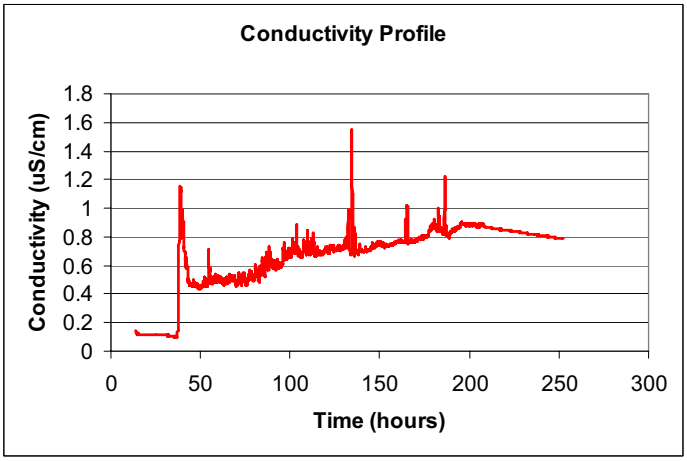

Figure 105 Test section conductivity during the 192 hours during supercritical water corrosion test at 500°C.

3.4.3 Materials Preparation and Characterization:

All test samples were rectangular in shape, 1.25" long and 0.5" wide and about 0.02" in thickness. Surface modification was performed on both sides of the samples, in order to enhance the resolution in weight change measurements after corrosion tests. The samples were progressively ground on both sides with silicon-carbide paper with grit sizes ranging from 320 grit to 1200 grit sizes, and final polished with a 1μm diamond paste to achieve a mirror-like surface finish. The samples were ultrasonically cleaned with acetone and ethanol prior to both surface treatments as well as prior to supercritical water corrosion tests.

Post corrosion, materials characterization was performed using the following techniques:

(i) weight change measurements were performed using a sensitive balance (0.1mg resolution) to evaluate weight change due to the growth of the oxide corrosion product (as expressed per unit area of the sample exposed).

(ii) scanning electron microscopy both in plan view and cross-section were used to examine the morphology and thickness of the oxide.
(iii) SEM-EDS (Energy Dispersive Spectroscopy) analysis of the oxide layer in cross-section was used to determine compositional gradients in the growing oxide layer.
(iv) Electron Back Scattered Diffraction (EBSD) was used to evaluate the various oxide phases (in combination with high magnification imaging) across the oxide layer.
(v) X-ray Diffraction (XRD) was used to identify the phases in the oxide and the crystallographic orientation of the growing oxide.
(vi) X-ray Photoelectron Spectroscopy (XPS) was used for determining the near-surface composition and phases in the as-surface modified and oxidized samples

A sample of the supercritical water was siphoned from one of the SCW runs for analysis of elements (particularly Fe, Ni, and Cr) at the University of Wisconsin's Water Chemistry Laboratory. However, the concentrations of the elements were below the detection limits of the spectrometer.

3.4.4 Materials Evaluation

First phase of the tests were performed on HT9, HCM12A, and T91 ferritic steels in the as-received and O^+ ion implanted conditions, in 500°C SCW with oxygen content of 25ppb, for exposure periods 1, 2, and 3 weeks. In the second phase, tests were performed in 600°C SCW with oxygen content of 25ppb, for exposure periods 2, 4, and 6 weeks. Samples tested in the second phase were NF616, HCM12A, and ODS steel in the as-received, O^+ ion implanted, and yttrium surface treated conditions. Post-supercritical water test evaluations were performed by the techniques discussed in the previous section. All samples tested developed a well-defined oxide layer (ranging from 4 to 70 μm in thickness depending upon the steel, surface treatment and test conditions) on the surface due to corrosion after exposure to supercritical water. Furthermore, for all alloys, SEM cross-sectional analysis examination showed the oxide corrosion product layer to be made of two regions with distinct morphologies. The outer layer was generally porous whereas the inner layer closer to the substrate steel was denser. EDS analysis showed the outer porous layer to be largely pure Fe-oxide, magnetite. The inner dense layer contained appreciable amounts of Cr and has been identified as a Fe-Cr spinel ($FeCr_2O_4$) compound.

3.4.4.1 500°C SCW Tests

3.4.4.1.1 HT9 steel

The results of weight gain measurements of HT9 steel in the as-received and oxygen ion implanted conditions are shown in Figure 106. For comparison. weight gain measurements of corrosion-resistant Ni-containing alloys D9 and IN 625 are also shown. It may be observed in Figure 106 that while the initial (1 week) weight gain is higher for the oxygen ion implanted samples, its weight gain is lower after 3 weeks of exposure compared to the untreated HT9 samples. It is speculated that this may be due to the formation of a higher density of oxide particulates (as shown in SEM images in Figure 107) during the initial stages of exposure, which may contribute to making the oxide more impervious to ion-transport processes during the later stages.

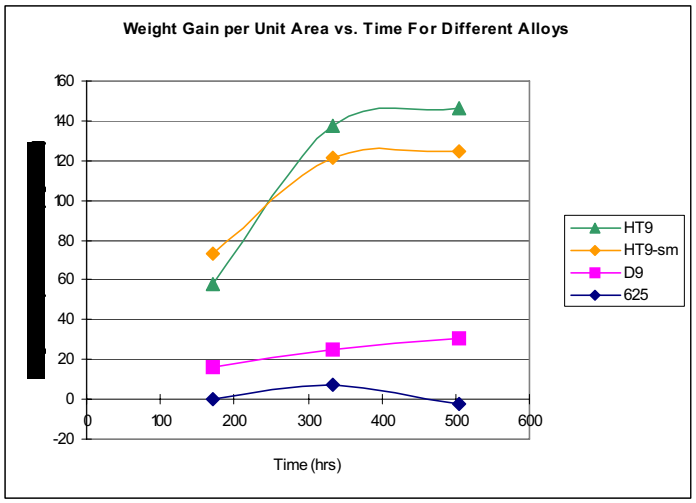

Figure 106 Weight gain measurements of HT9 steel in the as-received and oxygen ion implanted conditions after exposure to supercritical water at 500°C for periods of 1, 2, and 3 weeks. For comparison similar measurements of Ni-bearing, high Cr alloys, D9 and Inconel 625 are also shown.

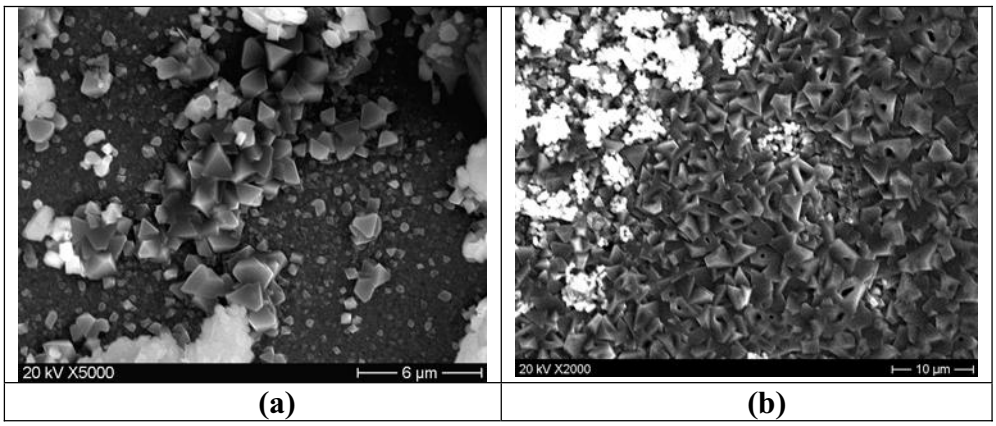

Figure 107 SEM surface plan view of the HT9 steel showing corrosion due to oxide particulate formation after exposure to supercritical water at 500°C for 1 week (a) as-received condition and (b) oxygen ion implanted condition. Higher density of oxide particulates is observed in the surface modified alloy.

Figure 108 shows the SEM images of the surface (in plan and cross-sectional view) of the oxide layer formed on HT9 steel after exposure to supercritical water at 500°C for 3 weeks. As evidenced by the plan views, both untreated and oxygen ion implanted samples exhibit a granular and porous structure with a grain size of about 2 to 4µm. The cross-sectional views of the oxide layer show a slightly lower thickness for the oxygen ion implanted sample.

To ascertain the phases present in the oxide layer a relatively new technique, Electron Backscatter Diffraction (EBSD) was performed using LEO 1530 Field Emission Scanning Electron Microscope. The technique allows for the identification of phases in the oxide layer while imaging the surface morphology of the oxide at high magnifications. Analogous to the TEM, this technique uses using electron diffraction for phase analysis; however this can be performed on the entire cross-section of the oxide, with no sample thinning requirements. Figure 109 shows the phase distribution across the oxide scale for the untreated and oxygen ion implanted samples, as determined using the Electron Backscattered Diffraction (EBSD)

technique. The outer region (in green) of the oxide was identified to be magnetite phase. The inner layer (red/yellow shade) between the outer oxide layer and the alloy substrate could not be identified in its entirety because it was composed largely of very fine grains. However, EBSD of selected grains (indicated in yellow) and EDS cross-sectional analysis indicate that this inner layer is predominantly a Fe-Cr spinel oxide compound. It may again be noted here that the total oxide layer thickness is lower for the oxygen ion implanted condition compared to the untreated condition, consistent with lower weight gain values for the oxygen ion implanted samples.

3.4.4.1.2 T91 Steel

Figure 110 shows the weight gain measurements for T91 steel in the as-received and oxygen ion implanted conditions after exposure to supercritical water at 500°C for 1, 2, and 3 weeks. For comparison purposes, the weight gain for untreated T91 exposed to SCW at the same temperature, but with 2ppm dissolved oxygen content (from a companion experiment) is also shown. The general trend for T91 is similar to that of HT9, in that the weight gain is similar for lower duration exposures; but after the 3 weeks exposure, the oxygen ion implanted steel samples exhibit a lower weight gain. The limited data set indicates the exponent of time dependence of corrosion 'n' is about 0.3 approaching a cubic growth law for oxygen ion implanted samples, whereas it exhibits a behavior in between cubic and parabolic (n=0.4) growth rates for the untreated samples. Cross-sectional SEM image of T91 alloy after exposure to supercritical water at 500°C for 3 weeks is shown in Figure 111. The accompanying EDS analysis clearly shows that the oxide layer is made up of two chemically distinct regions, pure Fe-oxide outer region and an inner region that is enriched in Cr.

In order to investigate the crystallographic orientation of the oxide layer on the surface, x-ray diffraction (CuKα radiation) was performed on the oxide layer that formed on the unimplanted and oxygen ion implanted T91 samples (Figure 112). It may be noted from the relative intensities of the peaks that for the 1 and 2 weeks exposure surface modification by oxygen ion implantation changes the growth orientation of the oxide on the surface. For the 3 weeks exposure, the relative intensities of the peaks appear more similar for the surface modified and as-received samples. This leads to the interesting conclusion that oxide particulate density and oxide growth crystallography crystallography can be affected by the pre-implantation treatment.

To further our understanding of the near-surface structural changes resulting from oxygen ion implantation, the surfaces of the T-91 steels were examined after oxygen ion implantation at 40 kV and a dose of $3x10^{17}$ ions/cm^2, prior to SCW exposure. Examination of the surface structure was made using an advanced JEOL-SEM, which provided a view of the structure on a nanometer size scale level that until recently was possible using only the TEM. Figure 113 shows the presence of extremely fine-grained nano-crystallites, which formed during ion implantation. In addition, presence of fine craters, few tens of nanometers in size, is observed and this forms as a result of differential sputtering (atom removal as a result of ion bombardment) between the matrix and islands of compositional segregation a few nanometers in size. More importantly, these micrographs show fine particulates of oxide, less than 10nm in size that formed as a result of ion implantation. It is these particulates that set the stage for the nucleation of the oxide layer upon exposure to high temperature supercritical water.

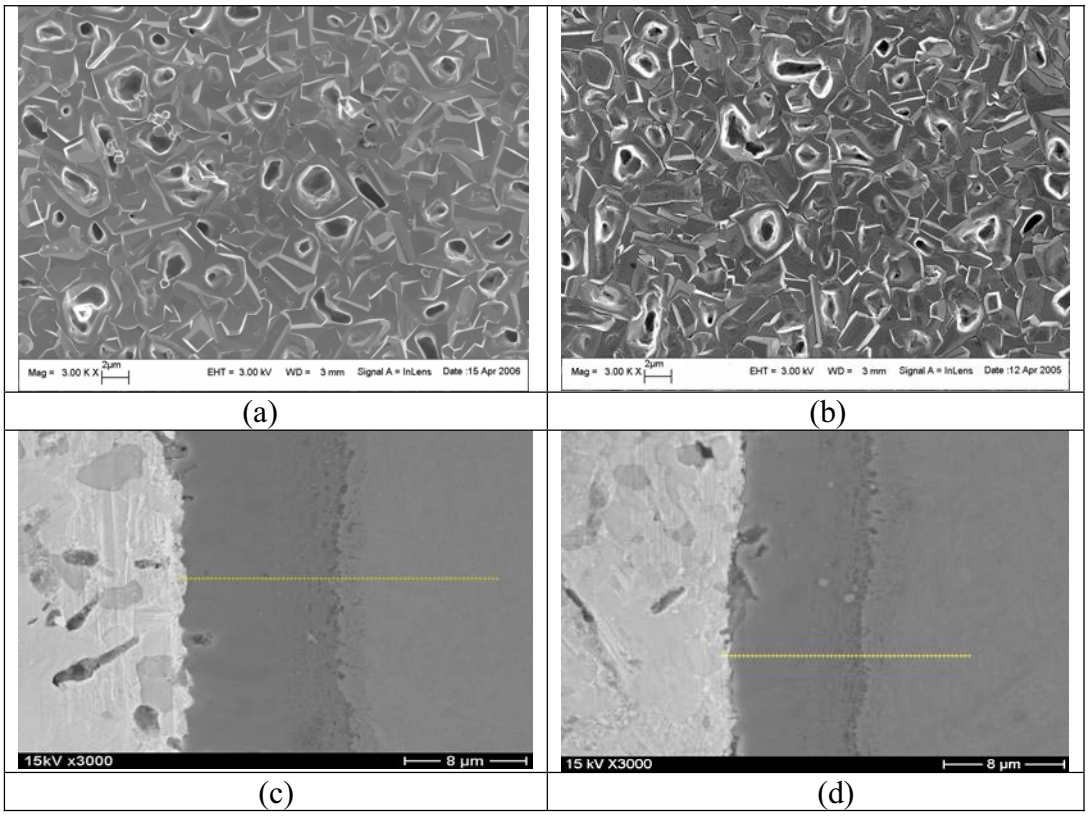

Figure 108 SEM images of the oxide corrosion product formed on steel HT9 after exposure to SCW at 500°C for 3 weeks, (a) untreated plan view, (b) O^+ ion implanted plan view, (c) untreated cross-sectional view, and (d) O^+ ion implanted cross-sectional view, and (d) O^+ ion implanted cross-sectional view.

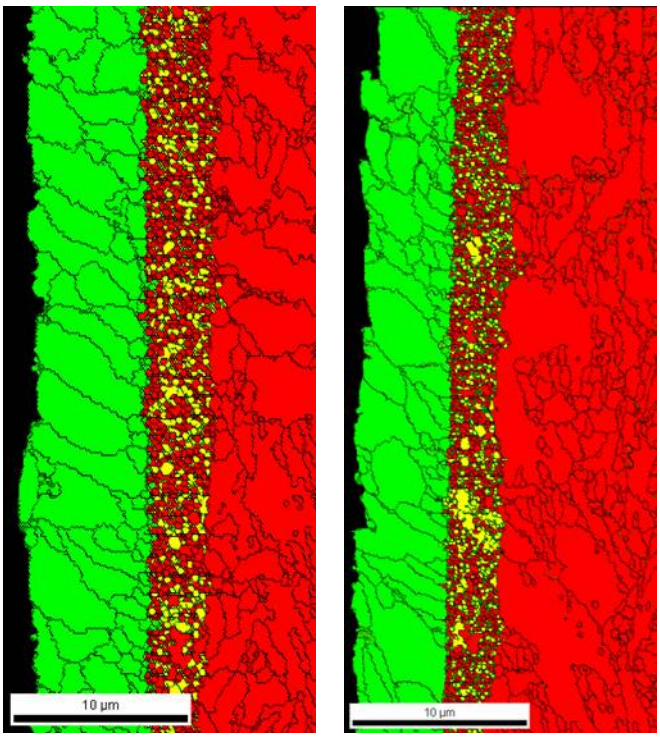

Figure 109 Electron Back Scattered Diffraction (EBSD) images of the cross-section of the oxide formed on HT9 steel after exposure to SCW at 500°C for 3 weeks, (a) as-received and (b) O+ implanted. Layer indicated by green is magnetite, whereas the inner yellow/red layer was identified to be a Fe-Cr spinel compound.

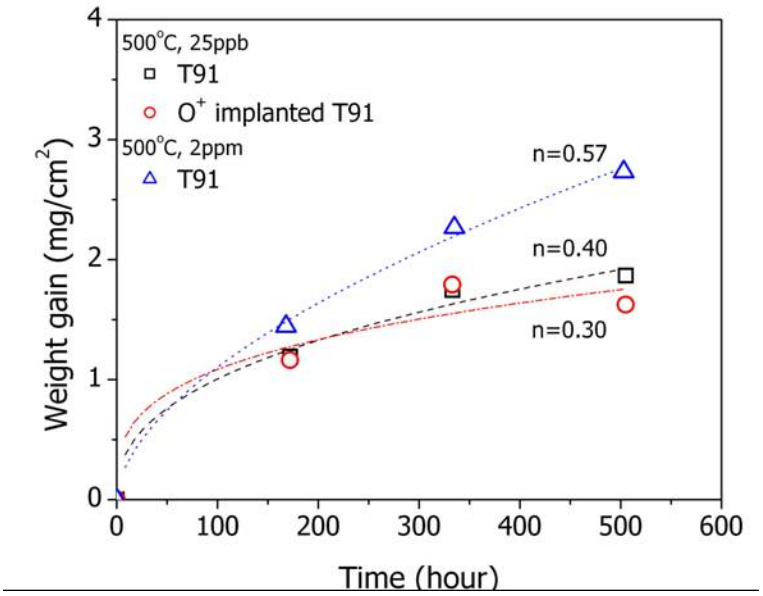

Figure 110 Weight gain measurements of T91 alloy in the as-received and oxygen ion implanted conditions after exposure to supercritical water at 500°C (25 ppb oxygen) for periods of 1, 2, and 3 weeks. For comparison results of weight gain for exposure in supercritical water at 500°C (2ppm oxygen) is also shown.

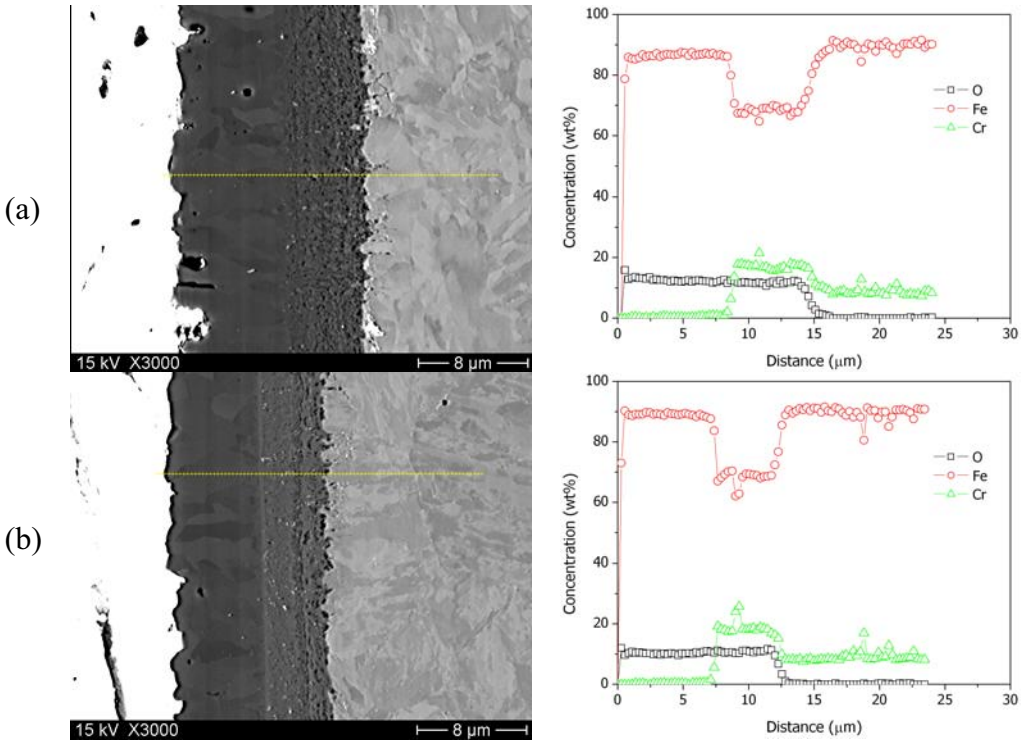

Figure 111 SEM cross-sectional image and corresponding EDS analysis of the oxide layer formed on T91 steel after exposure to supercritical water at 500°C for 3 weeks. (a) as-received and (b) O+ ion implanted conditions.

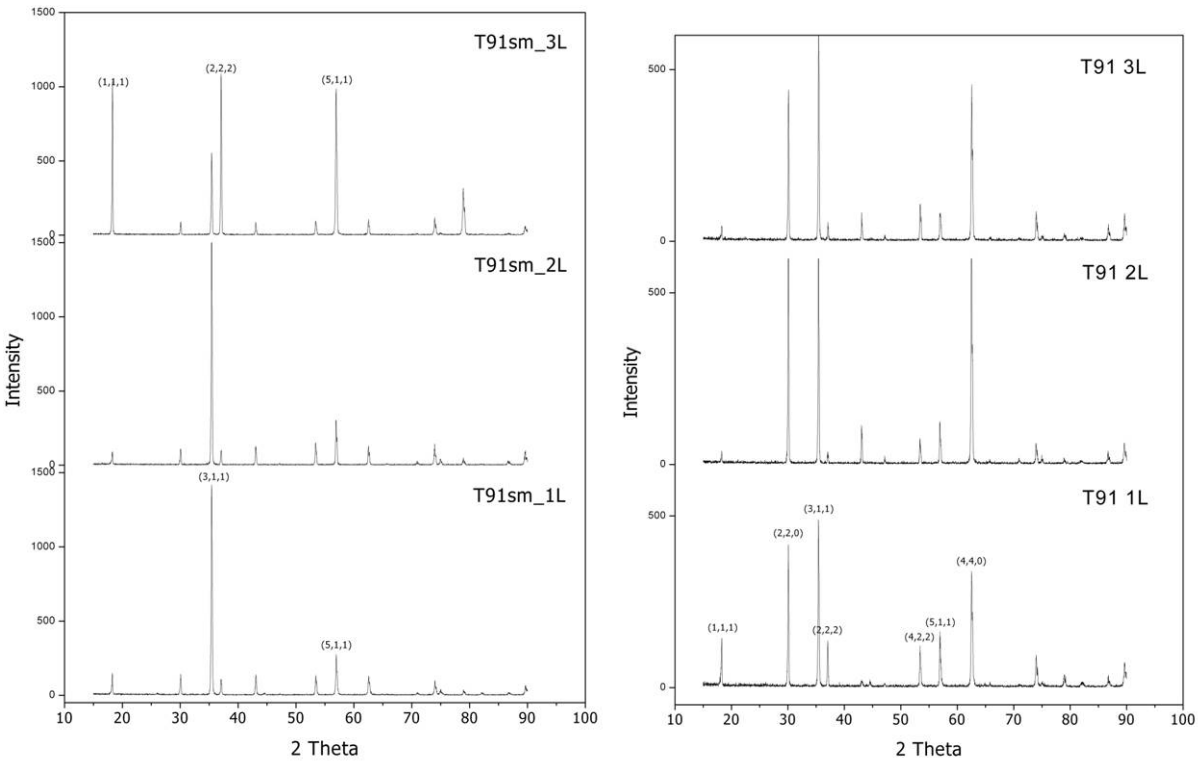

(a) (b)

Figure 112 X-ray diffraction patterns for T91 steel after exposure to supercritical water at 500oC for 1, 2, and 3 weeks (a) as-received and (b) after surface modification by oxygen ion implantation.

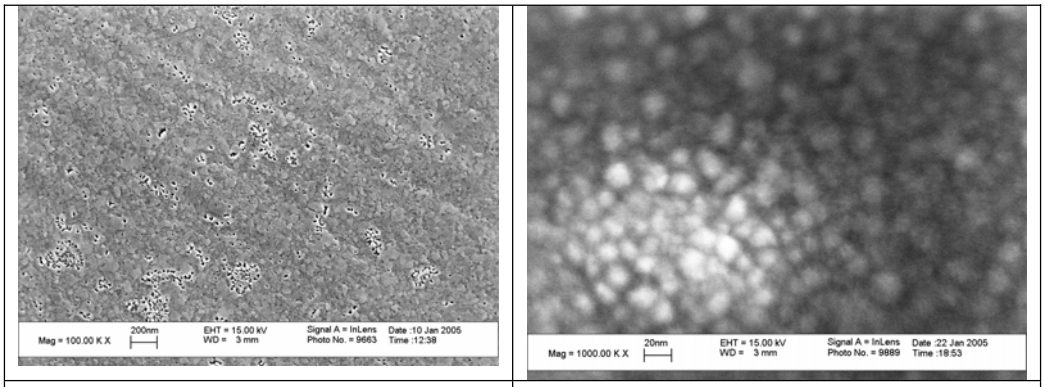

(a) (b)

Figure 113 (a) Evolution of fine-grained nano-crystallites and sputter craters in T-91 ferritic steel that formed as a result of oxygen ion implantation and (b) very fine oxide particulates, less than 20nm in size on the surface of this steel as a result of oxygen ion implantation.

To verify the formation of nanometer sized oxide particulates due to oxygen ion implantation and the modified depth, x-ray photoelectron spectroscopy (XPS) was performed. Analysis was performed both at the surface and after sputtering incrementally to various depths. The elemental chemical states of the oxygen ion implanted T91 as a function of depth below the surface of the samples were analyzed using XPS multiplex scans combined with Ar^+ sputtering. The results of this analysis for Fe 2p and Cr 2p

core levels are shown in Figure 114. The results reveal that after ion implantation the samples' surface was covered by an oxide film approximately 150nm in thickness. The sputter time in these figures is proportional to the depth below the surface at which the analysis was performed. Only oxidized Fe is observed at the surface and its characteristic peaks are located at ~710 eV for $2p_{3/2}$ and ~723.6 eV for $2p_{1/2}$, indicating Fe is present as FeO and Fe_2O_3. These Fe-oxides persist up to depths of about 30 nm and no Cr is observed in this region. Between depths of 30 nm and 60 nm from the surface, Cr is observed as evidenced by the presence of the characteristic peaks located at ~577 eV, which corresponds to Cr in the 3^+ oxidation state. After 55 min sputtering (about 165 nm depth), both Fe and Cr are present as metallic Fe and Cr, indicative of the unmodified substrate steel.

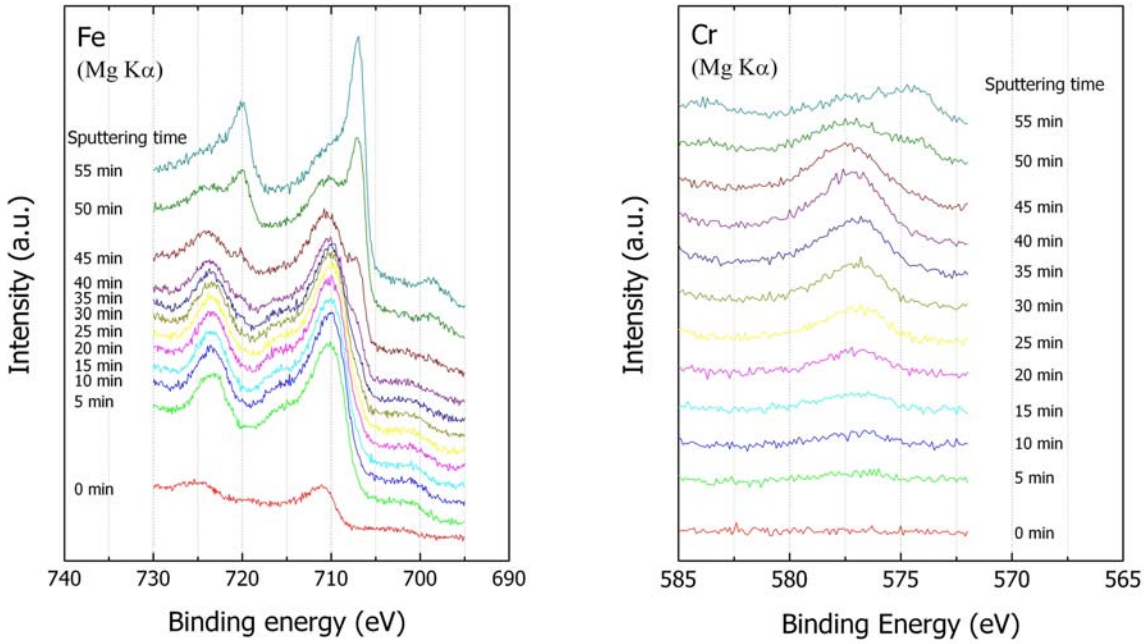

(a) Fe 2p (b) Cr 2p

Figure 114 Fe 2p and Cr 2p core level XPS spectra of the oxygen ion implanted T91 as a function of depth below the surface. Sputter time is proportional to the depth below the surface at which the analysis was performed. Sputter rate was 3nm/minute.

3.4.4.1.3 HCM12A Steel

Figure 115 shows the weight gain measurements for HCM12A steel after exposure to supercritical water at 500°C for 1, 2, and 3 weeks.

SEM examination of the oxide surface by imaging the plan view did not show any significant difference in oxide morphology between the untreated and oxygen ion implanted samples. However cross-sectional SEM of the oxide (Figure 116) did reveal a slightly lower thickness for the oxide layer, however, there were no appreciable differences in the composition of the oxide across its thickness for the two conditions,

3.4.4.2 Summary of the 500°C, 3 week run for HT9, T91, and HCM12A steels

Figure 117 summarizes the weight gains for the three steels in the untreated and oxygen ion implanted conditions after exposure to SCW at 500°C for 3 weeks. The performance rating (based on weight gain per unit area), in the order of decreasing performance was

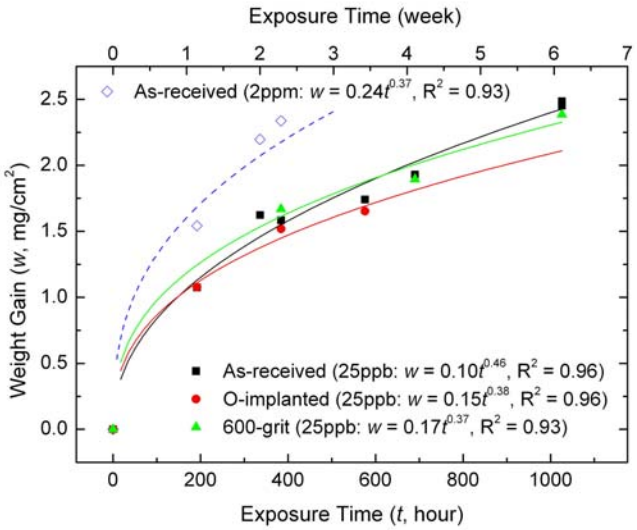

Figure 115 Weight gain for various exposure times for steel HCM12A after exposure to supercritical water at 500oC for 1, 2, and 3 weeks. Some data for the effects of surface roughness and oxygen content of supercritical water from companion experiments are also shown.

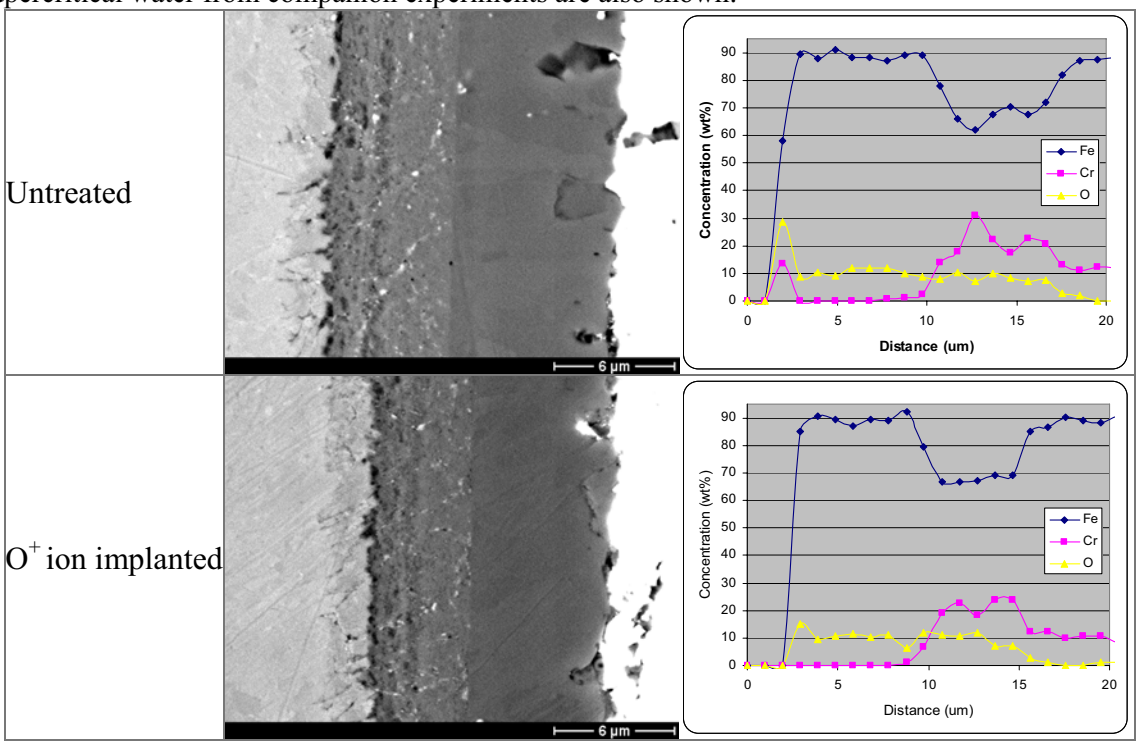

Figure 116 Cross-section of the oxide layer developed on HCM12A steel in the untreated and oxygen ion implanted conditions after exposure to SCW at 500oC for 3 weeks and corresponding EDS line scan compositional analysis across the oxide layer.

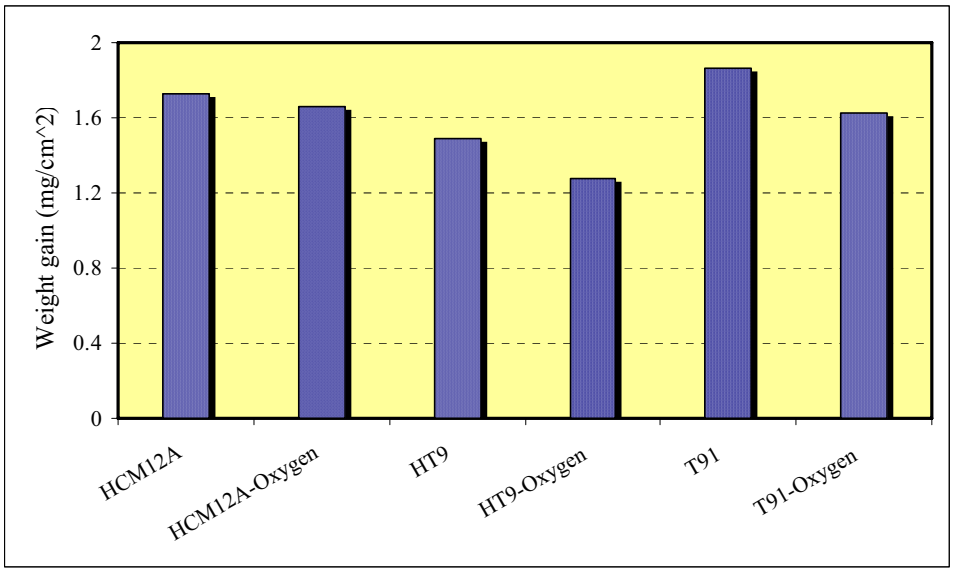

Figure 117 Results of weight gain measurements (per unit area) of the as-received and oxygen ion implanted steels after 3 weeks exposure to supercritical water at 500°C.

HT9 > T122 > T91. Oxygen ion implantation resulted in a slightly higher initial weight gain, but exhibited lower weight gain for longer exposures.

3.4.4.3 600°C SCW Tests

HCM12A and NF616 ferritic steel in the as-received (control), oxygen ion implanted and yttrium-surface treated conditions were exposed to supercritical water at 600°C (25 ppb dissolved oxygen) for exposure durations of 2, 4, and 6 weeks. In addition, samples of ODS steel in the untreated (control) and oxygen ion implanted conditions were also tested under these conditions. Weight gain measurements (expressed as weight gain per unit area) for each of these samples after exposure for 2, 4, and 6 weeks are shown in Figure 118, Figure 119 and Figure 120, respectively.

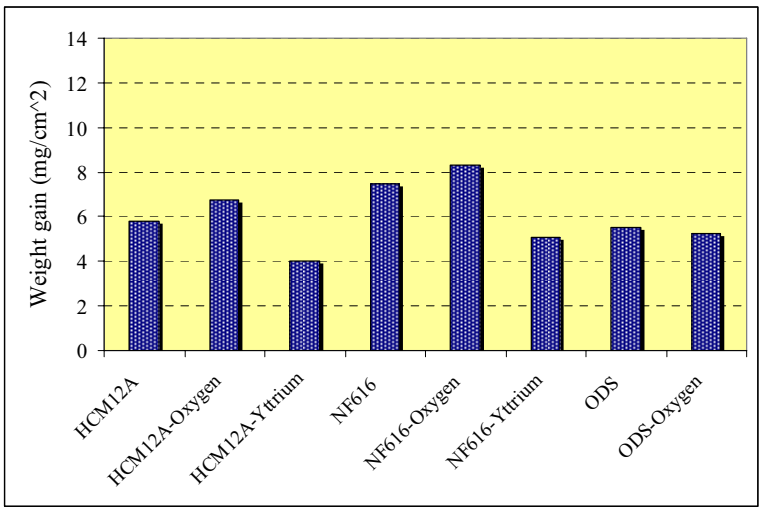

Figure 118 Results of weight gain measurements of ferrtic steel samples in various surface conditions after exposure to SCW at 600°C and with an oxygen content of 25ppb for 2 weeks.

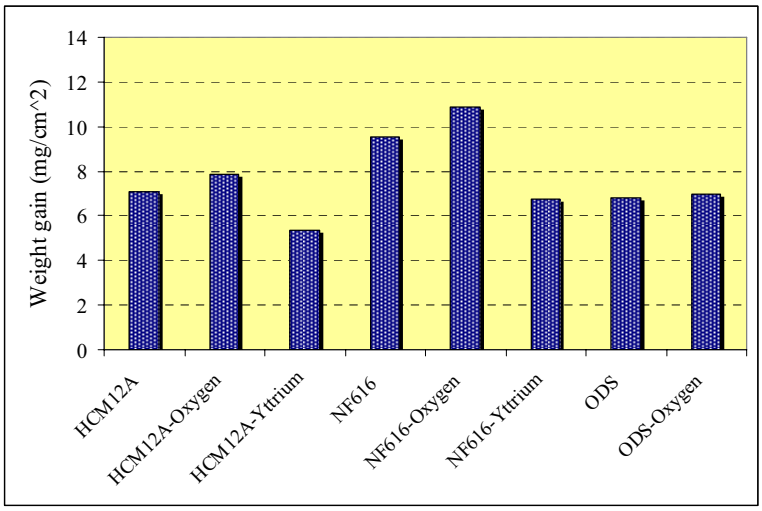

Figure 119 Results of weight gain measurements of ferrtic steel samples in various surface conditions after exposure to SCW at 600°C and with an oxygen content of 25ppb for 4weeks.

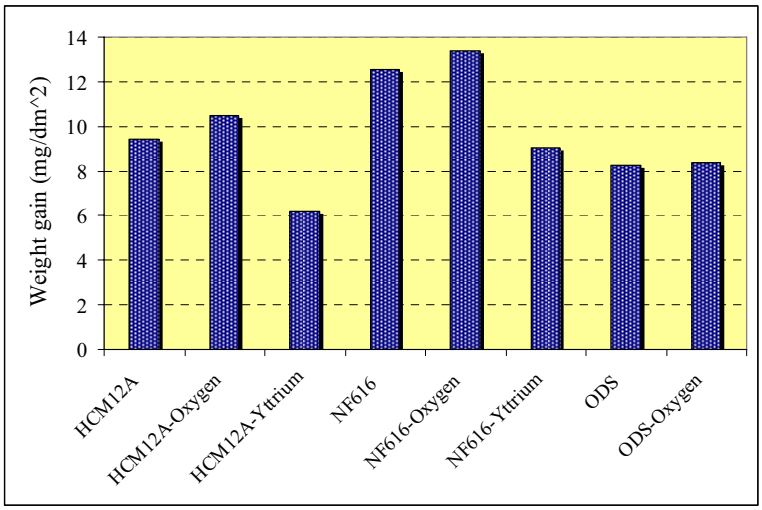

Figure 120 Results of weight gain measurements of ferrtic steel samples in various surface conditions after exposure to SCW at 600°C and with an oxygen content of 25ppb for 6 weeks.

As may be seen in Figure 118, Figure 119 and Figure 120 the oxygen ion implantation surface treatment results in a slight but consistently higher weight gain compared to the control samples, for steels HCM12A and NF616 for all exposure times. For the ODS steel, the oxygen ion implantation surface treatment results in no significant difference compared to the control sample. This is in contrast to the 500°C, where oxygen ion implantation surface treatment resulted in a lower weight gain for the three ferritic steels studied.

However, the yttrium surface treatment resulted in a significant improvement in oxidation resistance (i.e., lower weight gain) compared to untreated control samples after exposure to SCW at 600°C, for steels HCM12A and NF616. Figure 121, Figure 122 and Figure 123 show the oxide growth kinetics for the three steels in the oxygen ion implanted and yttrium surface treated conditions. All samples exhibit a parabolic oxide growth rate, however, time dependence exponent of oxidation, 'n', is lower for the yttrium surface treated samples, which is desirable from the stand-point of long-term oxidation resistance.

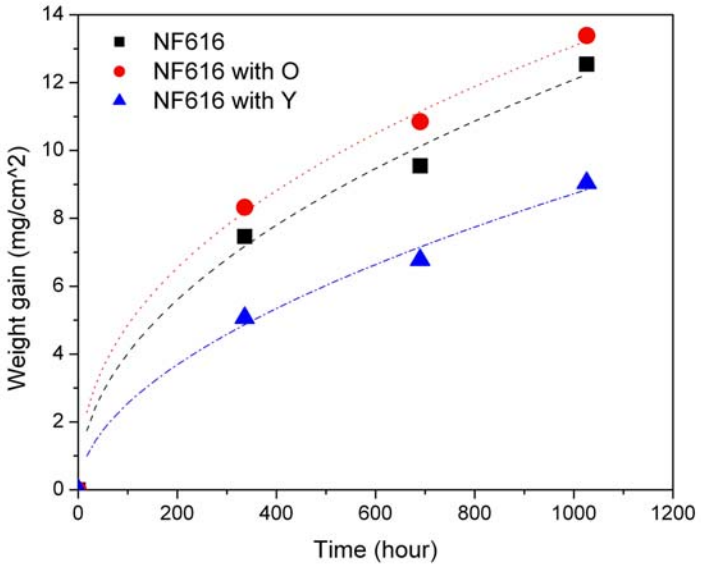

Figure 121 Results of weight gain measurements of ferrtic steel NF616 in various surface treated conditions after exposure to SCW at 600°C and with an oxygen content of 25ppb as a function of exposure time.

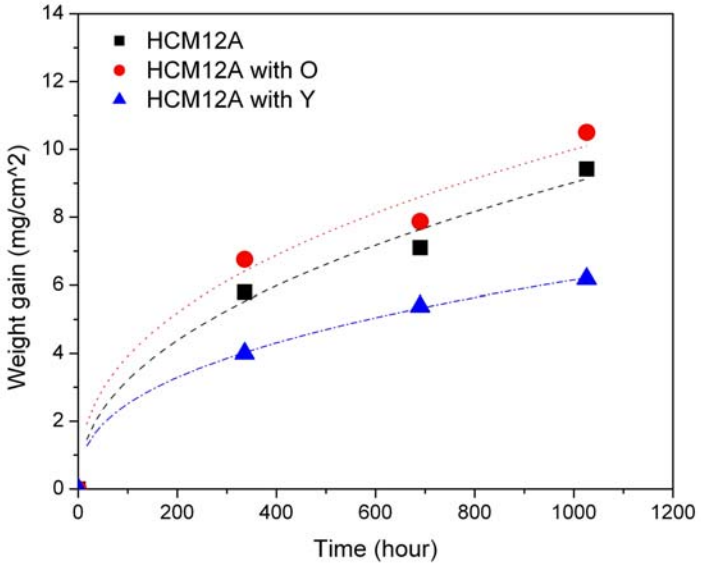

Figure 122 Results of weight gain measurements of ferrtic steel HCM12A in various surface treated conditions after exposure to SCW at 600°C and with an oxygen content of 25ppb as a function of exposure time.

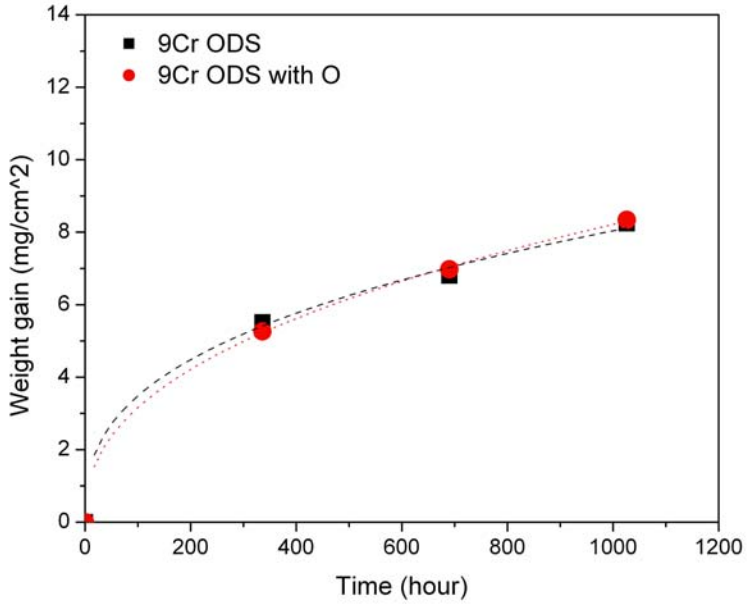

Figure 123 Results of weight gain measurements of ODS ferritic steel in various surface treated conditions after exposure to SCW at 600oC and with an oxygen content of 25ppb as a function of exposure time.

Results of SEM imaging (plan and cross-sectional view) and EDS compositional analysis of the oxide formed on HCM12A after exposure to SCW at 600°C for 6 weeks are shown in Figure 124. As in the case of the 500°C exposure, the oxide layer generally exhibits two distinct regions, an outer porous layer and a dense inner layer. This is particularly the case for the as-received and oxygen ion implanted steels. However, for the yttrium surface treated samples, both the overall oxide thickness and the extent of the porous layer are lower than the other two surface conditions. Figure 125 shows a SEM cross-sectional image of the oxide layer that developed on HCM12A after exposure to SCW at 600°C for 2 weeks and EDS compositional analysis taken at the band in the center of the oxide layer. The EDS analysis validates the presence of yttrium in oxide layer indicating that the original yttrium film oxidized and got incorporated in the growing oxide of the steel.

SEM examination both in plan and cross-sectional view were performed of the oxide layer that formed on steel NF616 in various surface treated conditions after exposure to super critical water at 600°C for 2, 4, and 6 weeks. As in the case of previous steels the plan view of the oxide revealed the oxide to be of a polyhedral, granular morphology. One observation rather unique to NF616 was the sporadic presence of intergranular cracks in the oxide and this was observed for all surface conditions. Figure 126 shows plan view images of the oxide layer developed on NF616 steel after exposure to SCW at 600°C for 2 weeks and 6 weeks. The grain size is about 2μm for the 2 weeks exposure and grows to about 5μm between 4 and 6 weeks exposure. Figure 127 shows the SEM images of the cross-sections of the oxide layer after exposure to supercritical water at 600°C for 6 weeks and the corresponding EDS line scan compositional analysis. As in the case of HCM12A, NF616 exhibits an oxide layer composed of two distinct regions, an outer porous layer and an inner dense layer. As may be observed in Figure 127, this is the case for the as-received NF616 and oxygen ion implanted NF616 samples. The yttrium surface treated samples however show a much more uniform overall oxide layer, with very little porous layer visible. The oxide thickness for the yttrium surface treated sample is substantially lower compared to either the untreated or the oxygen ion implanted samples.

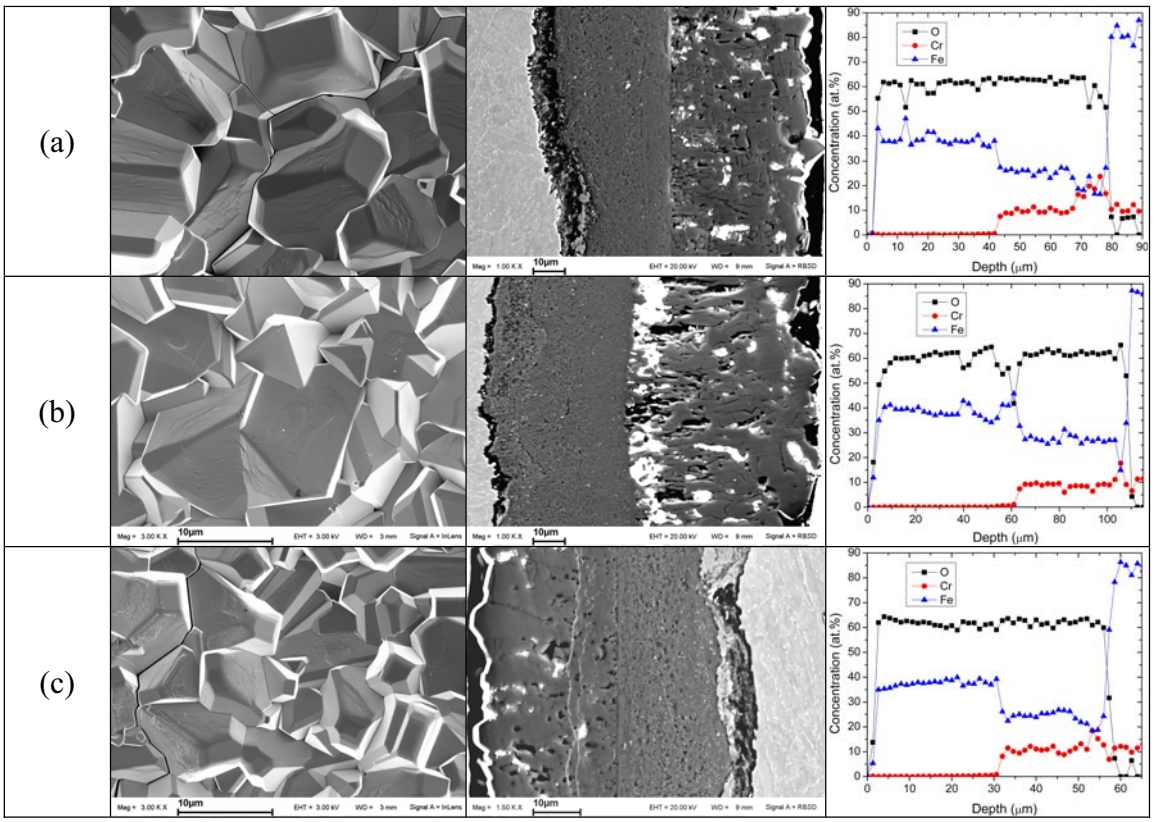

Figure 124 SEM images of the oxide formed on steel HCM12A in various surface conditions after exposure to SCW at 600°C for 6 weeks and the corresponding compositional line-scan across the oxide layer (a) as-received, control, (b) oxygen ion implanted, and (c) yttrium surface treated conditions.

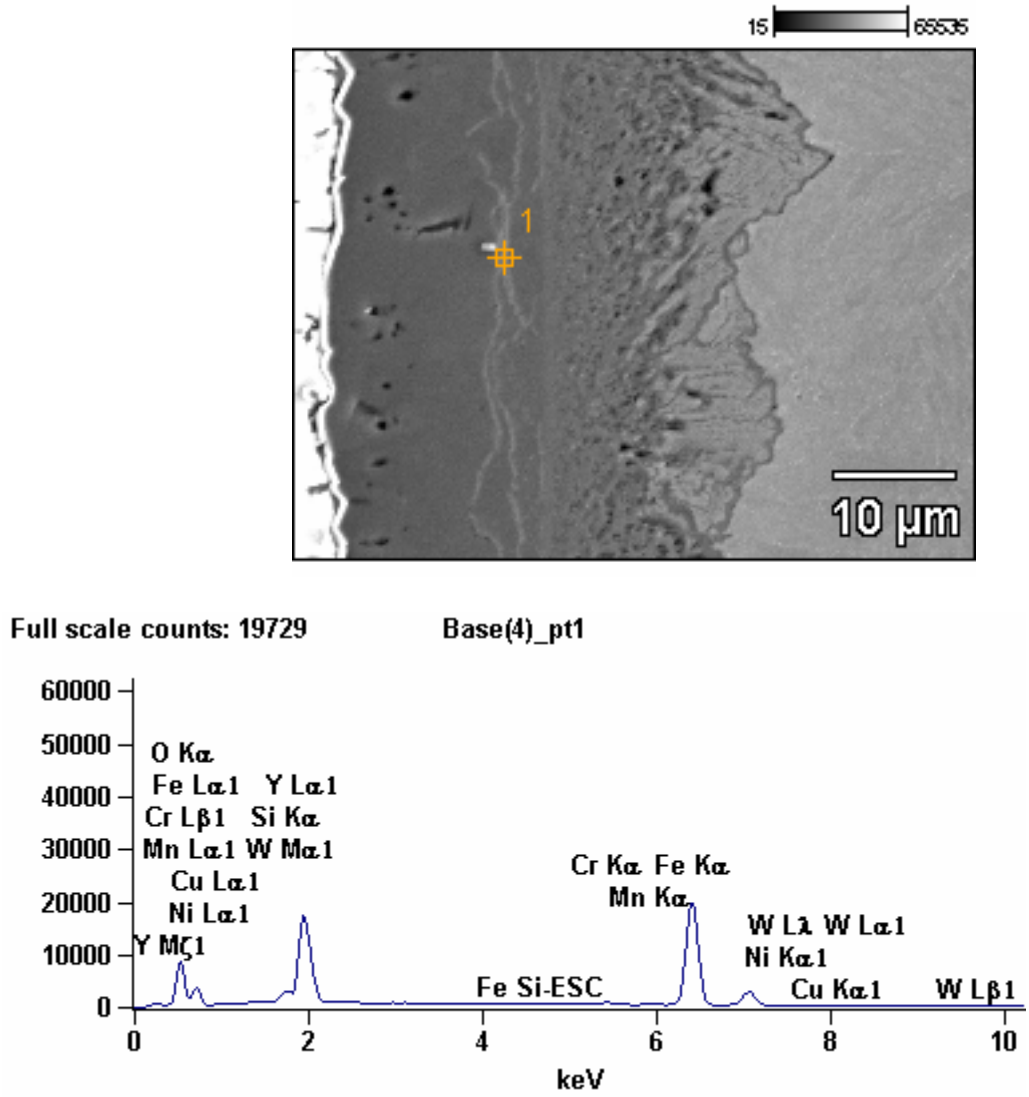

Figure 125 SEM image of the oxide formed on yttrium surface treated steel HCM12A after exposure to SCW at 600°C for 2 weeks and the EDS compositional spectrum (at region marked 1in the photograph) validating the presence of yttrium in the oxide layer.

(a)

(b)

(c)

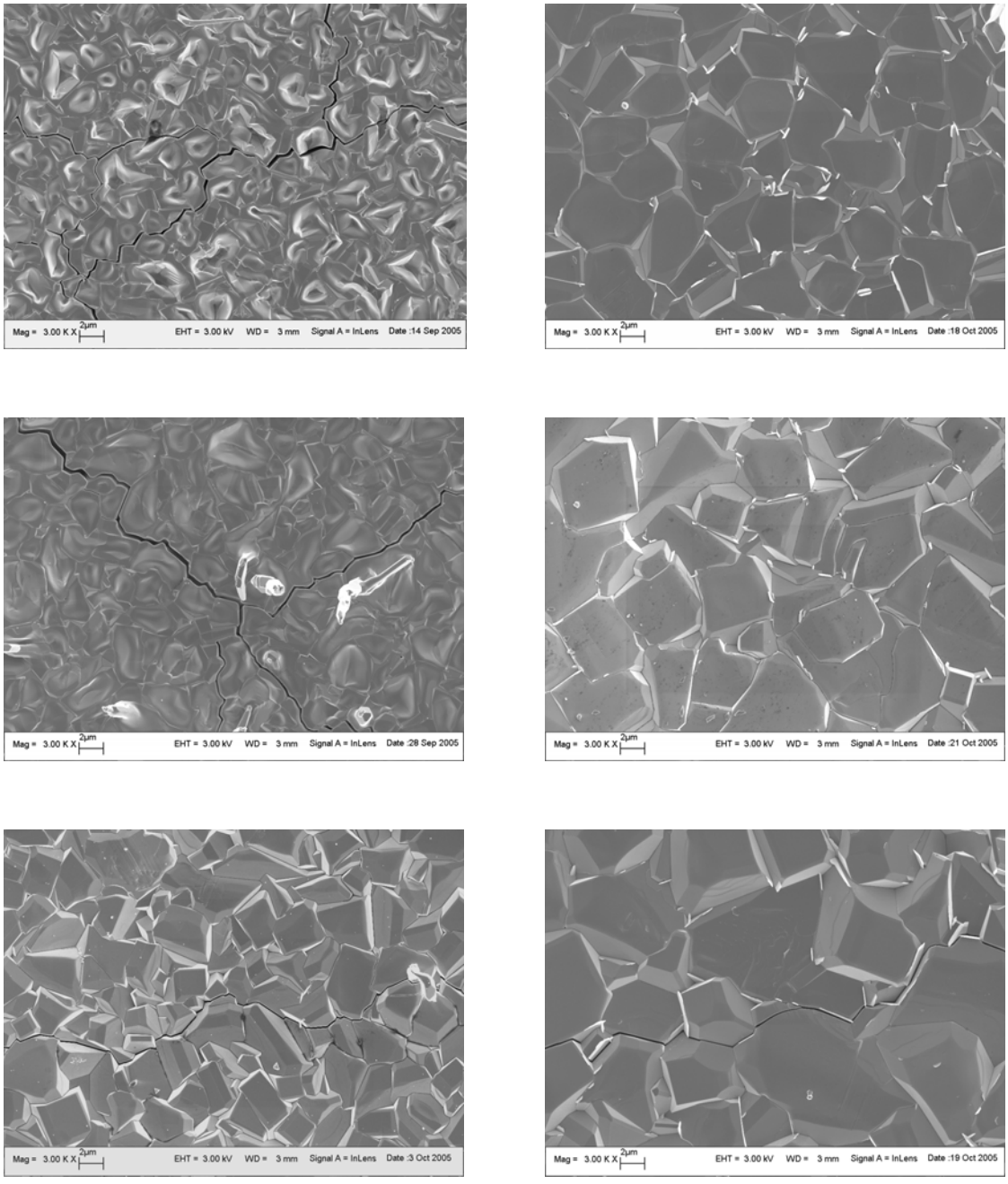

2 weeks 6 weeks

Figure 126 Plan view images of the surface of the oxide layer formed on NF616 steel showing a polyhedral, granular morphology after exposure to SCW at 600°C for 2 weeks and 6 weeks, (a) as-received, (b) oxygen ion implanted, and (c) yttrium surface treated.

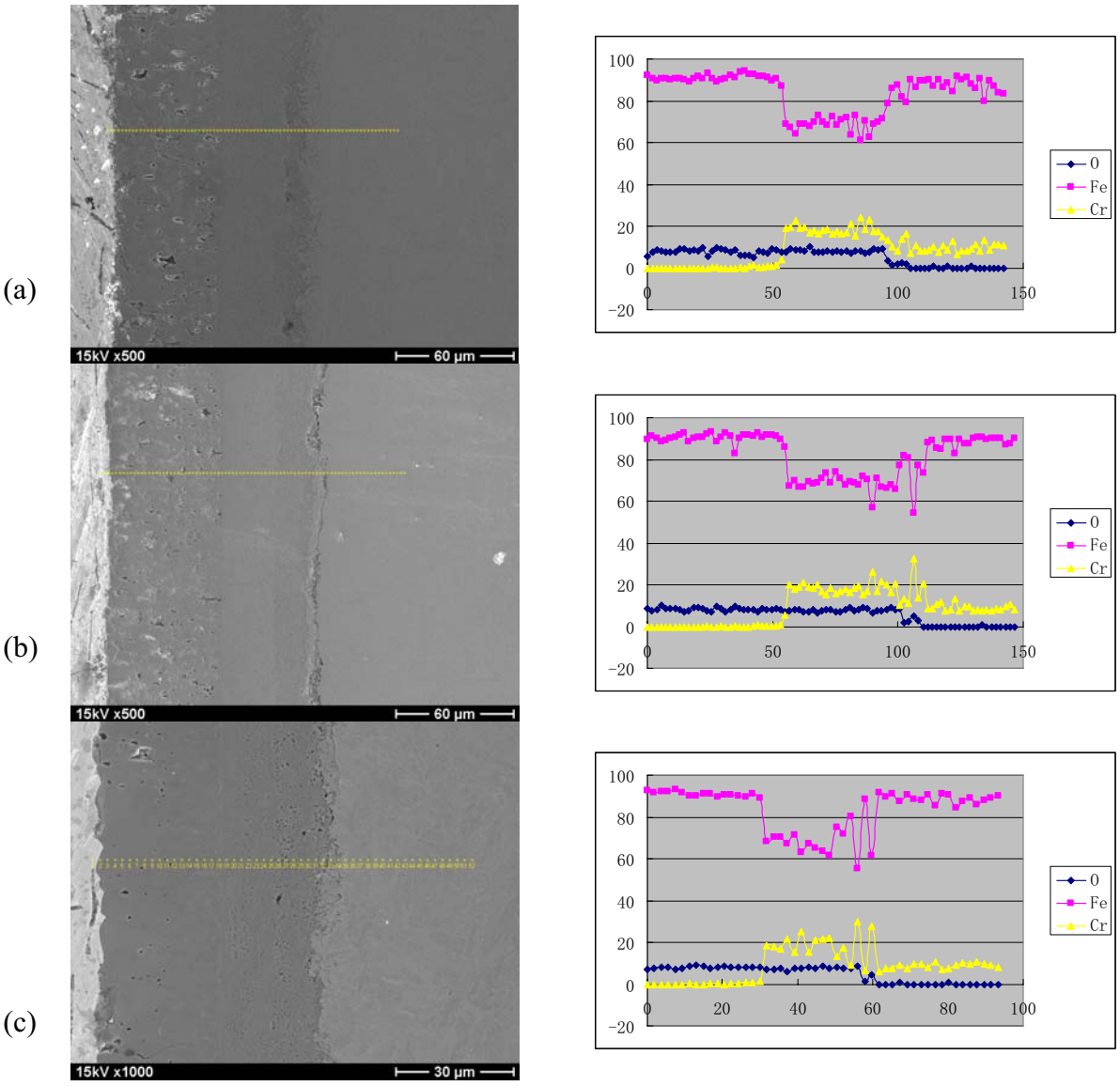

Figure 127 Oxide cross-sectional SEM images of the oxide layer formed on NF616 steel after exposure to SCW at 600°C for 6 weeks and corresponding EDS line scan compositional analysis , (a) as-received, (b) oxygen ion implanted, and (c) yttrium surface treated.

3.4.5 Surface Modification of SCC (stress corrosion cracking) Samples for Testing at University of Michigan SCW Facility

Nine SCC samples, three each of HT9, HCM12A, and T91 ferrtic steels, supplied to us by the University of Michigan were oxygen ion implanted on one side (with two other side receiving implantation dose as well, but the back side facing the stage was not implanted) and sent back to University of Michigan for stress corrosion cracking tests. At the University of Michigan they will be tested using the constant extension rate tests in order to evaluate the effect of oxygen ion implantation on crack initiation and growth. It is anticipated that three physical effects of oxygen ion implantation may affect SCC performance, (i) formation of a high concentration of nanometer sized oxide particles in the

near surface regions of the steels, (ii) compressive stresses at the surface that may delay crack initiation, and (iii) the ballistics of the ion implantation process may alter the microstructure at the surface through homogenization effects. Figure 128 shows the SCC samples of the three steels just after removing from the plasma immersion ion implantation chamber after oxygen ion implantation. Oxygen ion implantation was performed at an energy of 40kV to a dose of $3x10^{17}$ ions/cm^2.

Figure 128 SCC samples of the three steels, HT9, HCM12A and T91 steels just after removing from the plasma immersion ion implantation chamber after oxygen ion implantation.

3.4.6 Conclusions

Five candidate ferritic steels HT9, HCM12A, T91, NF616, and ODS steel were tested for corrosion resistance in supercritical water at 3650 psi and 25 ppb dissolved oxygen content. Steels HT9, HCM12A, and T91 in the untreated and oxygen ion implanted conditions were tested at 500°C for exposure durations of up to 3 weeks. Steels HCM12A, NF616 in the untreated as well as oxygen ion implanted and yttrium surface treated conditions were tested at 600°C for exposure durations of up to 6 weeks. ODS steel in the untreated and oxygen ion implanted conditions were also tested at 600°C for exposure durations of up to 6 weeks.

For the base steels (not surface treated) tested at 500°C (up to 3 weeks), the rating of the steels in the *decreasing order of oxidation resistance* was as follows: HT9 > HCM12A > T91. For the base steels (not surface treated) tested at 600°C (up to 6 weeks), the rating of the steels in the *decreasing order of oxidation resistance* was as follows: ODS > HCM12A > NF616. For all base steels the oxide layer exhibited two distinct regions, an outer porous region which was identified to be Fe-oxide, magnetite and an inner dense region that was enriched in Cr (up to about 20% Cr) and identified to be a spinel compound. For the range of steels and test conditions studied, the thickness of the oxide scale ranged from about 4μm to about 70μm.

Surface modification was noted to have an effect of the total oxide thickness, oxide growth kinetics, and the morphology of the oxide layer. Oxygen ion implantation of the steels led to a lower oxide thickness and growth rate when exposed to SCW at 500°C for up to 3 weeks. It was demonstrated by electron microscopy (and confirmed by XPS) that the oxygen ion implantation results in a fine (~ 10nm) distribution of spherical oxide precipitates in the near-surface regions of the steels. It is speculated that these oxide particles, increase the nucleation and particulate density of the thermal oxide that forms

during initial stages of exposure to SCW, thereby making it more impervious during later stages of growth. X-ray diffraction of the oxidized surface also showed that the texture of the oxide (its growth direction) is altered by the oxygen ion implantation.

For steels tested at 600°C SCW, oxygen ion implantation had no effect on the oxidation of ODS and in fact had a slight deleterious effect on the oxidation of steels NF616 and HCM12A. However, *yttrium surface treatment had a pronounced beneficial effect* on steels NF616 and HCM12A for the 600°C. HCM12A steel exhibited about 40% and NF616 steel exhibited about 25% less weight gain after exposure to SCW at 600°C for 6 weeks, compared to their respective untreated counterparts. Yttrium surface treatment also influenced the oxidation characteristics of these two steels in two practically beneficial ways, (i) the growth kinetics of the oxide was lowered by the incorporation of yttrium in the growing oxide layer and (ii) the oxide layer is rendered markedly more dense which is desirable from the standpoints of the long term mechanical stability of the oxide, in addition to making it more impervious to ion transport.

Figure 129 summarizes the key results of this study and shows that *hierarchy in the performance rating of the steels can be altered by surface modification*. Nine SCC (stress corrosion cracking) samples, three each of HT9, HCM12A, and T91 ferrtic steels have been oxygen ion implanted at an energy of 40kV to a dose of $3x10^{17}$ ions/cm^2 and sent the University of Michigan for SCC evaluation at 500°C.

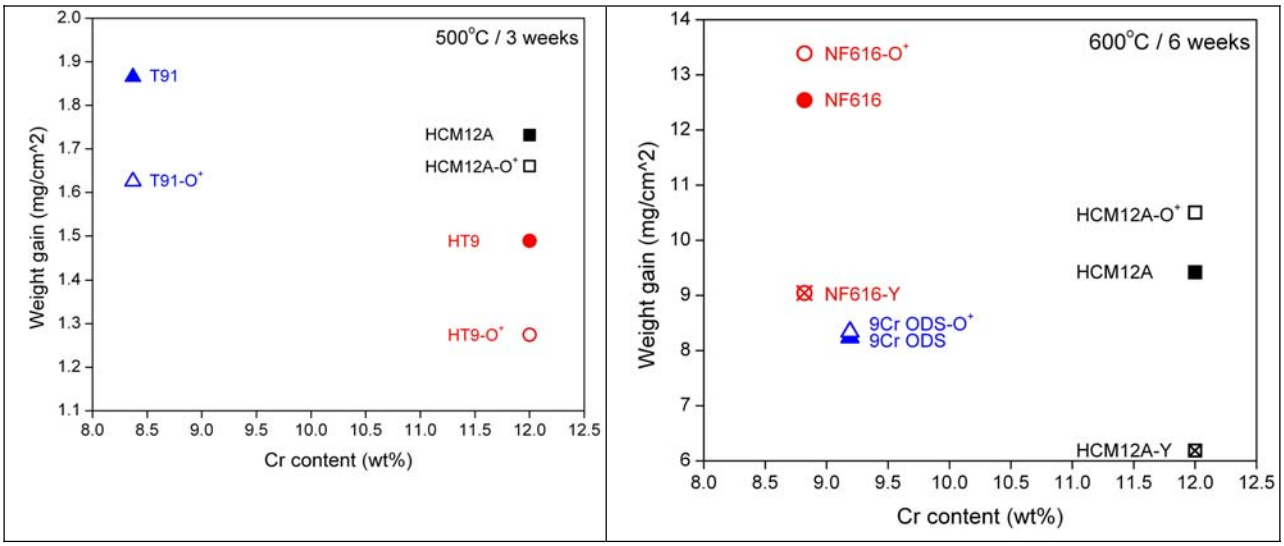

Figure 129 Performance of various steels and surface treatments in SCW at 500°C and 600°C (25 ppb oxygen). Note that performance rating of the steels can be altered by surface modification.

4. Task 4 - Radiation Stability Studies

4.1 Task Summary

Swelling, bubble formation, precipitation, segregation, and hardening can all occur under irradiation in the temperature and dose range proposed for the supercritical water reactor. Alloys are required that are either resistant to these processes or can accommodate these processes without compromising their structural integrity. Proton and heavy-ion irradiation in the dose range 5 - 50 dpa and in the temperature range 400-500°C were conducted to evaluate the susceptibility of the candidate alloys to these potentially life-limiting processes. Three different irradiation studies were conducted in the task. In the first study, Ni ion irradiation up to 50 dpa was used to evaluate the radiation response of 12 Cr F-M HCM12A and high Ni 800H alloys. In the second study, microstructures of proton-irradiated samples irradiated up to 7 dpa were examined. The same samples were used in the previously described SCC tests. Finally, hardness and cross-section microscopy measurements were used to compare the relative radiation response of F-M and ODS alloys irradiated with heavy-ions.

4.2 Heavy Ni-Ion Irradiations of Alloys HCM12A and 800H

Contributors:

James Cole, Jian Gan, INL

4.2.1 Material

The composition for alloy HCM12A is listed in Table 2, while 800H is listed in Table 23. Both alloys are commercial grade and used in the as-received condition. No thermal mechanical treatment was given. The manufacturer of the alloy 800H specified a final heat treatment at temperature of 1177ºC for 2.25 hours. The supplier of HCM12A specified a final heat treatment of normalization at 1050ºC + air cool and tempered at 770ºC + air cool.

Table 23 The Composition for alloy 800H.

Alloy	Fe	C	Mn	P	S	Si	Ni	Cr	Mo	Other
800H	Bal.	0.069	0.76	0.014	0.001	0.13	31.59	20.42	Not measured	Ti_0.57, Cu_0.42 Al_0.50

4.2.2 Alloy HCM12A

In addition to this INERI project, another DOE-NE project, NERI project 02-110, has a shared interest in understanding the potential impact of long term radiation effects in high temperature alloys previously not considered for radiation service. As a result two alloys of common interest were selected for conducting a joint transmission electron microscopy (TEM) study of two samples that were Ni-ion irradiated at the accelerator facility at PNNL.

Alloy HCM12A was irradiated with 5 MeV Ni ion to 5 and 50 dpa at a temperature of 500ºC with a damage rate of 5dpa/hr. The irradiated microstructure was characterized at a depth of 0.5 μm from the irradiated surface. The microstructure of unirradiated HCM12A mainly consisted of precipitates that distributed both at grain boundaries and in the matrix. The dislocation density is not uniform from grain to grain. The diffraction pattern and EDS analysis of the precipitates revealed nearly all the precipitates in the unirradiated case are $M_{23}C_6$ with a FCC lattice parameter of 1.06 nm and a typical composition of approximately (in wt%) 65%Cr, 30%Fe, 3%W, 1.5%Mo in addition to carbon. Dislocation density varied dramatically, ranging from dislocation free to the dense areas with tangled and complex dislocation configuration. The general views of unirradiated microstructure and the detail arrangement of dislocations are shown in Figure 130 and Figure 131.

For the sample irradiated to 5 dpa, there is no significant change in microstructure photos, shown in Figure 130(b) and Figure 131(b). No cavities were found and no dislocation loops were identified. The precipitates examined were still dominated by $M_{23}C_6$, but few vanadium-niobium precipitates identified from EDS analysis, with a typical composition of approximately 50%V, 17%Cr, 17%, 12%Nb. Figure 132 shows various precipitates suspended on a film formed accidentally during jet-polishing, giving an opportunity for improved measurement for precipitate composition than EDS of precipitates in the matrix. Among the precipitates in the picture, those marked p04, p08 and p11 are V-Nb precipitates and the rest are mostly $M_{23}C_6$ precipitates. The inserts in Figure 132shows the EDS spectrum of M23C6 and V-Nb

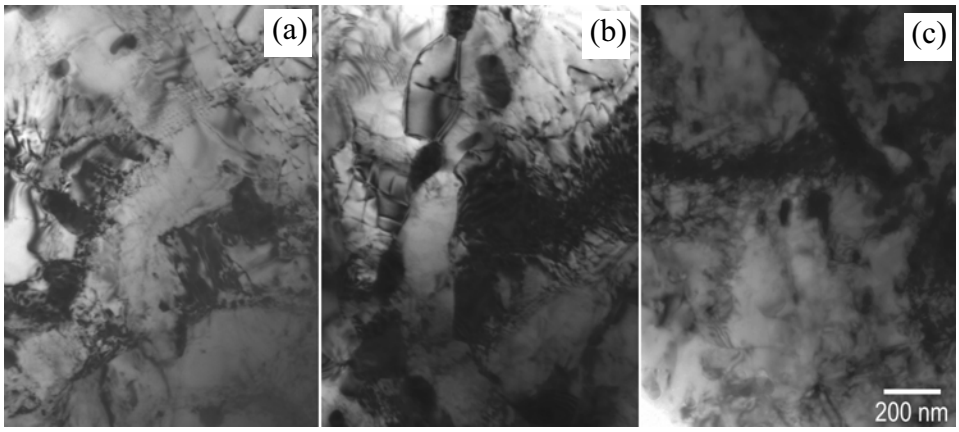

Figure 130 Low magnification overview of microstructure for alloy HCM12A irradiated with Ni ion at 500ºC to (a) unirradiated, (b) 5 dpa and (c) 50 dpa.

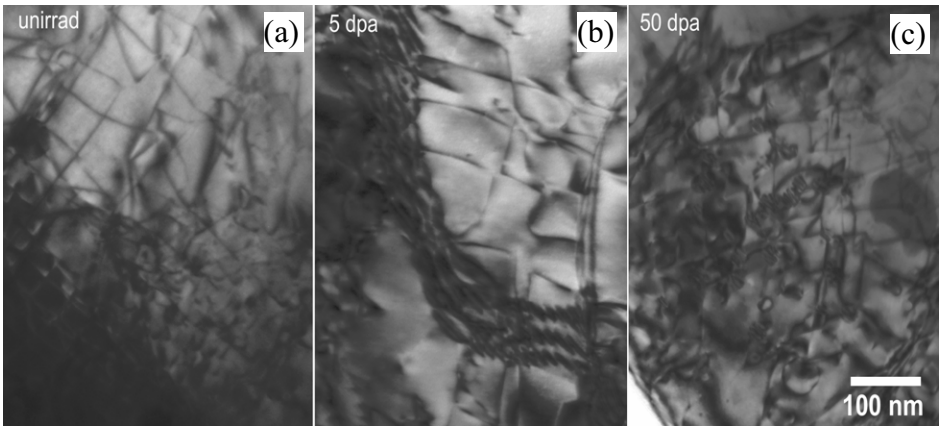

Figure 131 Dislocation microstructure for alloy HCM12A irradiated with Ni ion at 500ºC to (a) unirradiated, (b) 5 dpa and (c) 50 dpa.

precipitates. The overall dislocation density appeared slightly increased as shown in Figure 130 and Figure 131. No quantitative measurement on dislocation density was attempted due to its non-uniform distribution and extremely high density in the dense dislocation areas. The presence of V-Nb precipitates and the increase in dislocation density may be responsible for the radiation hardening in alloy HCM12A.

The microstructure of HCM12A irradiated to 50 dpa is similar to that at 5 dpa as demonstrated in Figure 131 (c) and Figure 131 (c). Again, no voids were found in this condition. However some dislocation loops were found in the dense dislocation areas, no significant changes in dislocation configuration although the overall dislocation density appeared further increased comparing to the case of 5 dpa. The microstructure at 50 dpa is still dominated by dense dislocation network and $M_{23}C_6$ precipitates.

4.2.3 Alloy 800H

The unirradiated microstructure of alloy 800H is shown in Figure 133. The picture showed a relatively high dislocation density (~ $4x10^{13}$ m^{-2}) for the alloy heat treated at 1177ºC for 2.25 hours. There are no precipitates found in the unirradiated condition. It was found that the sample was slightly magnetized as the electron beam in the microscope drifted slightly during the sample tilting.

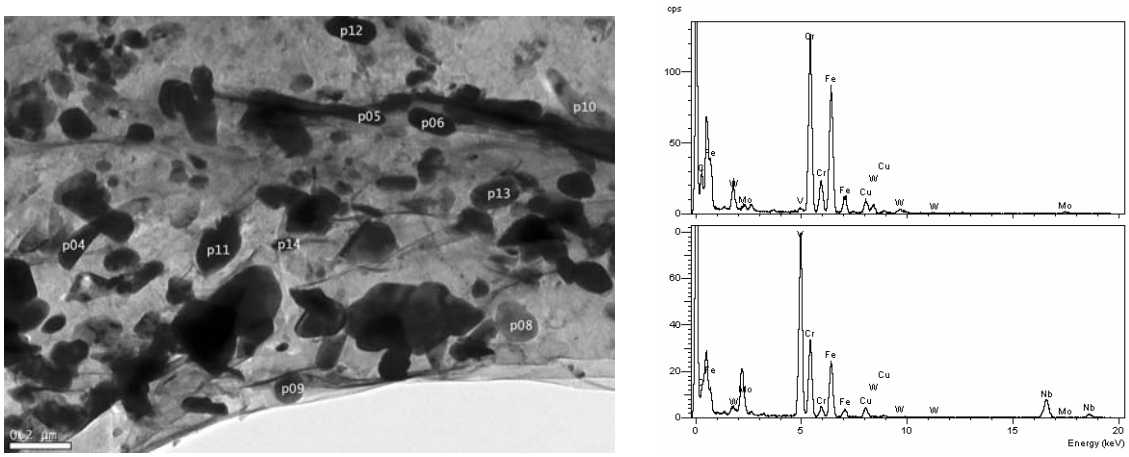

Figure 132 in HCM12A irradiated with Ni ions at 500ºC to 5 dpa. Those marked p04, p08 and p11 are V-Nb precipitates. The rest are mostly M23C6 type precipitates.

For the 800H irradiated with Ni ion at 500ºC to dose of 5 dpa, the microstructure was altered by the formation of faulted dislocation loops. No voids were found at 5 dpa. The irradiated microstructure is dominated by the dislocation loops shown in Figure 134. The average size of the faulted loops is 12.5 nm with a loop density of 1.2×10^{16} cm^{-3}. Although no radiation-induced precipitates were found in the matrix, precipitates were found in a piece of suspension film attached around the edge of the perforation. This suspension film was formed accidentally during the jet-polishing and provides an opportunity to reveal the possible precipitates in the materials. Figure 135 shows precipitates caught on the suspension film and the EDS spectrum comparison between the matrix and the precipitates on the film. These precipitates have an average size of approximately 9 nm. The EDS spectrum shows that these precipitates are rich in Cr (40~56%), Si (4~14%), Al (5~10%) and Ti (1.5~2.5%). The crystal structure of the precipitates could not be determined due to the small size and the presence of multiple types of precipitates. Since a 5 dpa irradiation only took 60 min to complete, it is difficult to believe all these precipitates were formed due to irradiation. It appears that most of these precipitates were existed in the unirradiated materials but at a very low density, therefore difficult to detect.

For the 800H irradiated to 50 dpa at 500ºC, the irradiated microstructure is dominated by the faulted loops and the small precipitates uniformly distributed through out the sample. No cavities were detected under this irradiation condition. The bright field image (g=200) and the rel-rod dark filed image of the faulted loops are shown in Figure 136. The average size of faulted loops is 8.4 nm with a loop density of 2.3x1016 cm-3. While an increase by nearly a factor of 2 in loop density is expected when comparing to a 5 dpa sample, the decrease in loop size was a surprise. The decrease in loop size may be due to the presence of finely distributed small precipitates developed at high dose. The finely distributed precipitates, shown in Figure 137, were not seen in 5 dpa and the unirradiated samples. The average size of these precipitates is 5.9 nm, about 50% smaller than the precipitates observed in 5 dpa sample shown in Figure 137. Since the dark filed image of the precipitates in Figure 137 was taken using the diffraction from the precipitates, not all the precipitates were present in the picture. The estimated precipitate number density is greater than 9.1×10^{15} cm^{-3}, at least more than two orders of magnitude higher than the precipitates in 5 dpa sample. Both composition analysis and the crystal structure determination for these small precipitates were not successful due to their small sizes. These uniformly distributed small precipitates are expected to play an important role in material mechanical properties. Once formed, these precipitates will act as extensive sinks for point defects, alter the microstructural evolution under

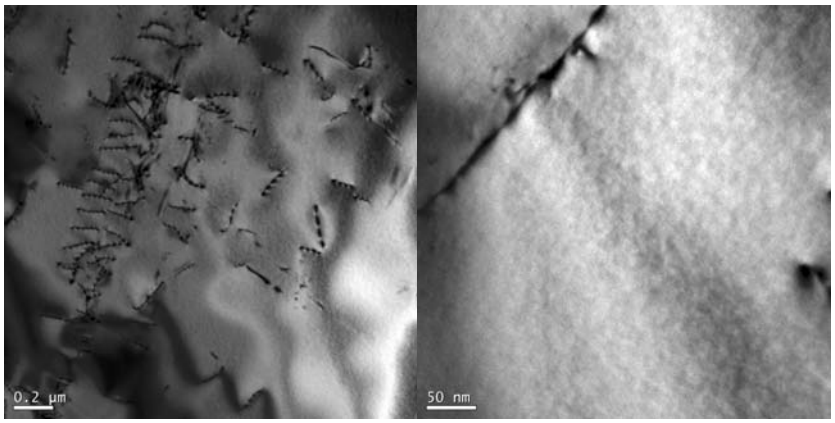

Figure 133 Unirradiated microstructure of alloy 800H (imaged with g=200 diffraction) reveals dislocations in low magnification (left) and high magnification (rght). The alloy has a relatively high dislocation density considering it was heat-treated at 1177ºC for 2.25 hours.

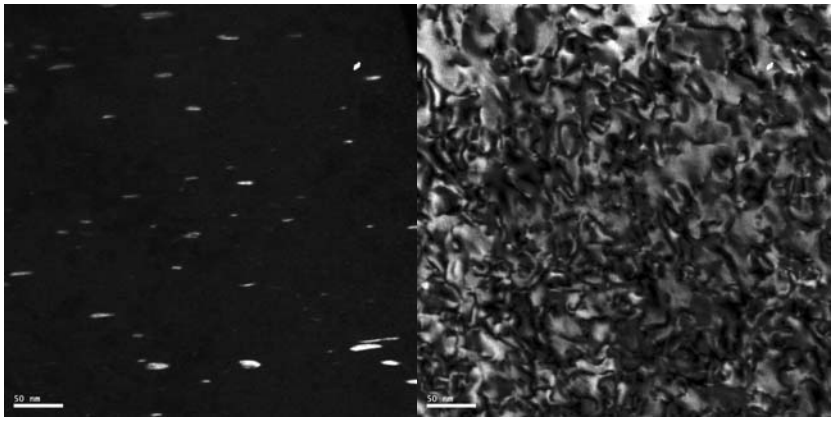

Figure 134 Microstructure in alloy 800H irradiated with Ni ion at 500ºC to dose of 5 dpa. Bright filed image (left) showing dislocation loops under g=200 and the rel-rod dark filed image (right) showing ¼ of the faulted dislocation loops.

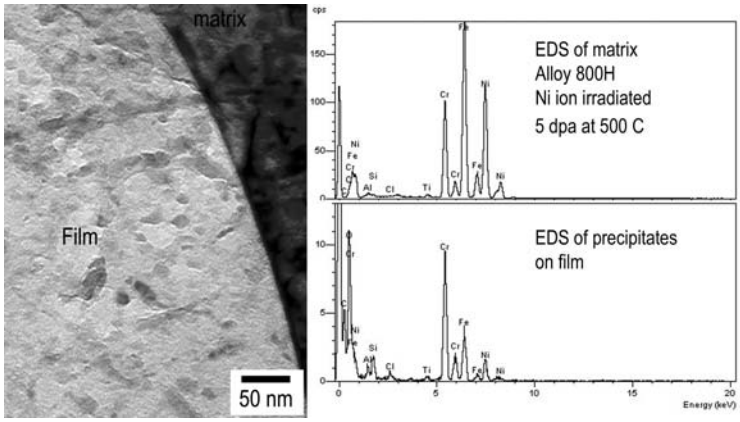

Figure 135 Precipitates caught on a suspension film near the edge of the perforation (left) in 800H irradiated at 500ºC to 5 dpa. The EDS comparison between the matrix and precipitates on film showing the precipitates are rich in Cr, Si, Al and Ti.

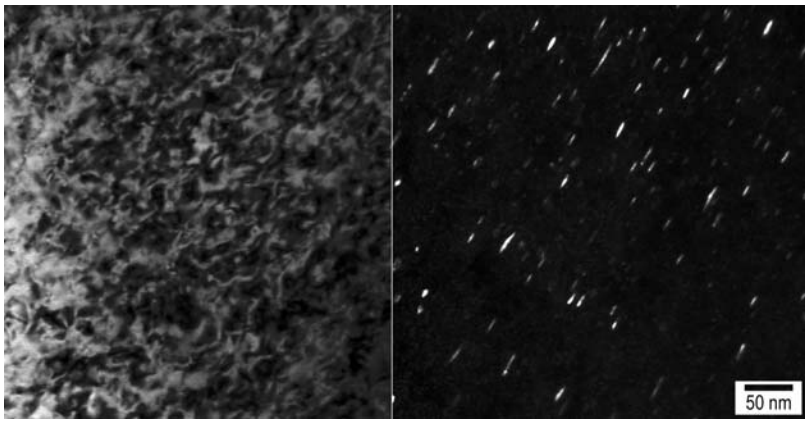

Figure 136 Dark file image of finely distributed precipitates in 800H irradiated with Ni ions at 500ºC to 50 dpa. The image was taken using the diffraction from the precipitates.

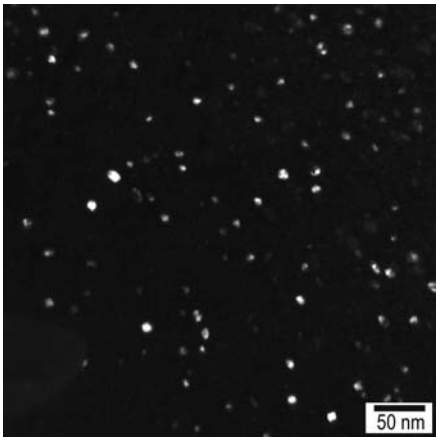

Figure 137 Dark file image of finely distributed precipitates in 800H irradiated with Ni ions at 500ºC to 50 dpa. The image was taken using the diffraction from the precipitates.

irradiation such as loop formation and growth. It is believed the presence of finely distributed precipitates may be responsible for the decrease in loop size at high dose comparing to 5 dpa sample.

4.3 Proton irradiation Studies of F-M Alloys

Contributor:

Gary Was, University of Michigan

Proton irradiation of F-M samples was conducted with 2.0 MeV protons at Michigan Ion Beam Laboratory. The protons beam was started up with stage current 30 μA then gradually increased to 50 μA. The dose rate was about 0.039 dpa/hr and the total dose of 7 dpa was reached in about 180 hr. During irradiation the temperature was controlled at 500±10°C by a combination of heating and cooling. It was found that irradiation temperature was maintained within the specified 10°C window about the target temperature. The average temperature over all eight samples is 500.6±4.28°C.

The hardness of TEM samples was measured by Vickers hardness indentation before and after irradiation. After irradiation the hardness of all samples is increased due to irradiation hardening. The hardness following irradiation is highest in HT9 (289.19 kg/mm^2), followed by HCM12A (246.85 kg/mm^2, average from 2 samples), and T91 (249.78 kg/mm^2). For the change in hardness, T91 has the largest increase, followed by HT9 and HCM12A. The hardness measurement and changes in hardness are shown in Figure 138.

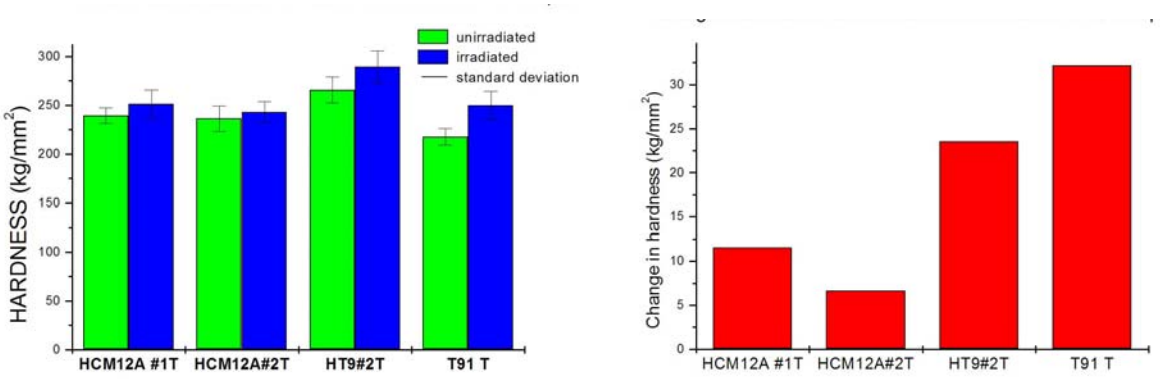

(a) (b)

Figure 138 (a) Hardness of unirradiated and 7 dpa irradiated sample (b) Hardness changes in samples irradiated to 7 dpa.

Figure 139 and Figure 140 illustrate the microstructures of these samples following irradiation. The microstructure of the irradiated alloy 591 contained dislocation loops, black dot damage and precipitates, while, in addition to these features alloy HCM12A contained a population of voids in the material. In addition to the microstructural analysis, grain boundary chemistry measurements were conducted on alloy T91. These measurements indicate strong enrichment of chromium and depletion of iron at the grain boundary as indicated in Figure 141.

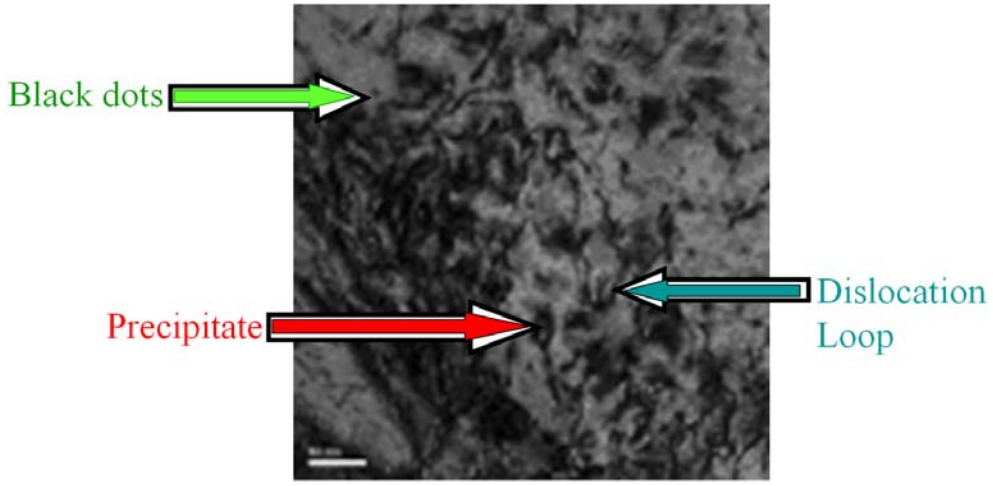

2MeV at 400°C to 7 dpa

Figure 139 Dislocation and precipitate structure in proton irradiated alloy T91.

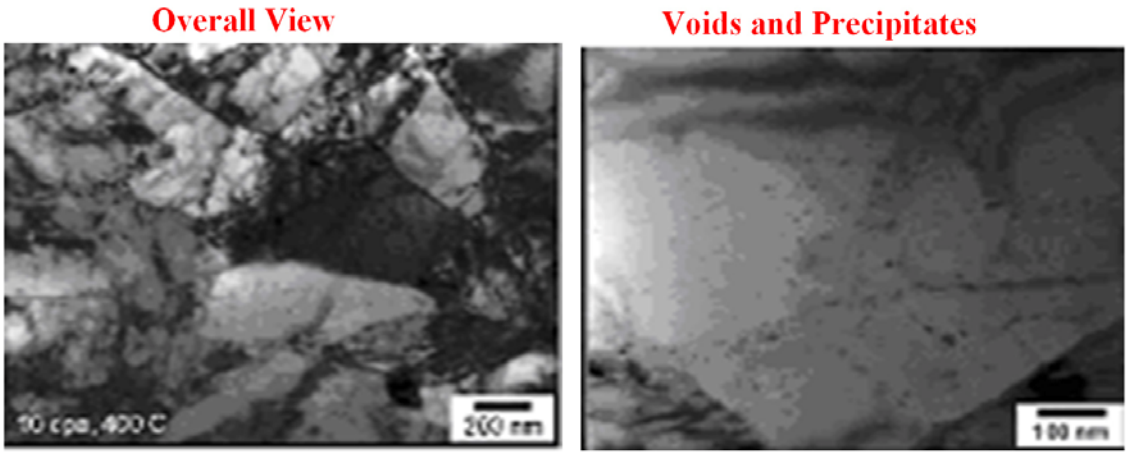

2MeV at 400°C to 10 dpa

Figure 140 Dislocation and void and precipitates in proton irradiated HCM12A.

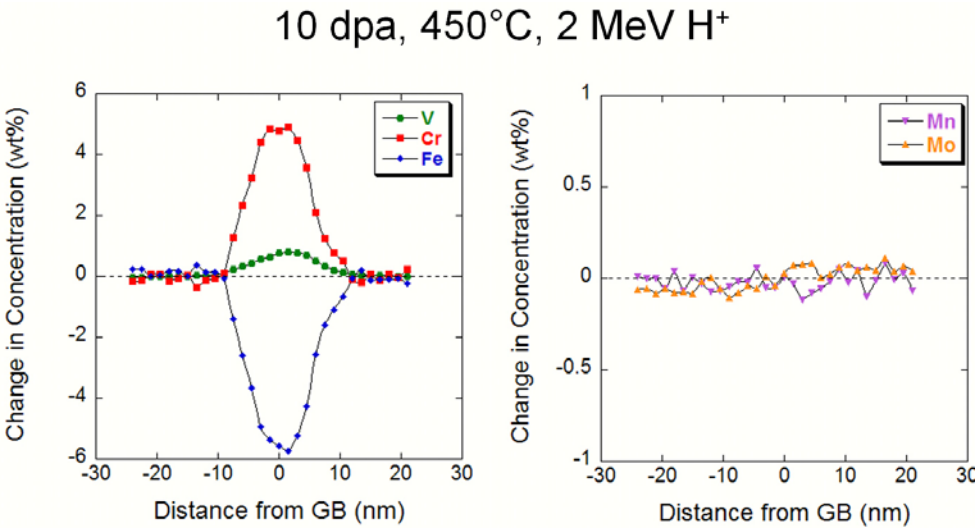

Figure 141 Grain boundary chemistry profiles of alloy T91 irradiated with protons.

4.4 Irradiation Damage of F-M and ODS Alloys

Contributors:

Jinsung Jang, KAERI

Soon Hyung, KAIST

4.4.1 Overview

For the simulation of irradiation effect, high energy ion irradiation experiments were performed on samples of recrystallized MA956, T91 and T92.

4.4.2 Hardness of Irradiated Commercial ODS Alloys

Alloy samples with dimension of 10×10×2 mm were prepared for irradiation and their surfaces were mirror-polished by diamond paste for further evaluation. Ion accelerator(Tandem Van de Graaff Accelerator, NEC 5SDH-2) was used. 8MeV Fe^{4+} ions made by SNICS ion source were used to irradiate the specimens. The MA956 and T91 samples were irradiated at room temperature with fluence of $7.6\times10^{16}/cm^2$ and $7.1\times10^{16}/cm^2$ for each and a total dose of 1.0dpa.

To know the dependence of hardness on indentation load, nanoindentation experiments with various loads were performed. Figure 142(a) shows the loading-unloading curves during indentation in MA956 specimen. As the indentation load increases the depth increases and constant hardness is obtained at load over 2000μN as shown in Figure 142(b). Therefore, the load for hardness measurement is determined to be 3000μN. Figure 143(a) shows the hardness results measured at irradiated and unirradiated area in MA956 specimen. Irradiated area has higher hardness and less depth than unirradiated area at the same load. This means that irradiated area has been damaged by high energy ion so that many defects such as vacancy, dislocation and void are formed. Microstructure observation is scheduled for further research. Figure 143(b) is the hardness result of T91 alloy and shows the same results. The hardness increase of MA956 is more or less higher than T91. Generally, it is known that ODS alloy has better irradiation resistance than conventional alloy due to stable dispersoid. This result doesn't show any better irradiation resistance of ODS alloy. However, irradiation resistance highly depends on temperature. If irradiation is performed at high temperature, where ODS alloy shows better high temperature stability, it is predicted that better irradiation resistance of ODS alloy will be evident.

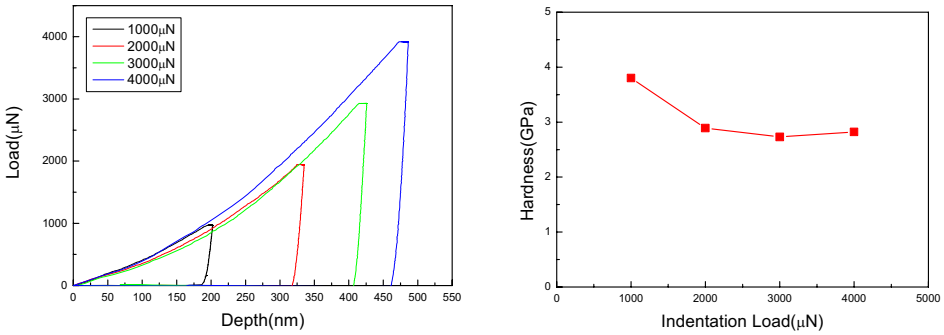

(a) (b)

Figure 142 (a) Loading-unloading curve during indentation and (b) hardness-load relationship at various indentation loads in MA956 alloy.

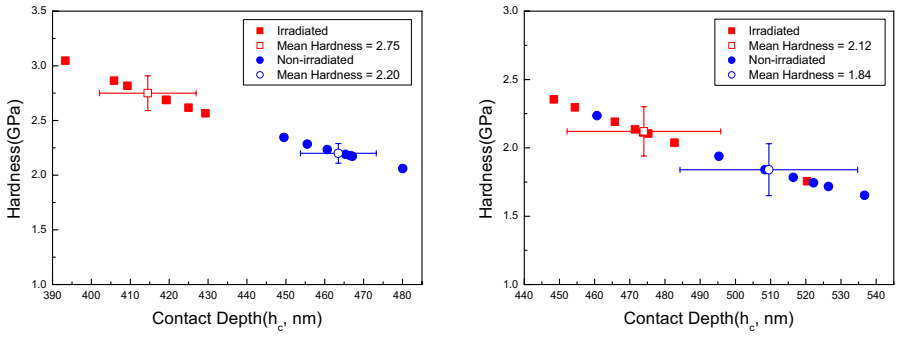

(a) (b)

Figure 143 (a) Hardness of irradiated and unirridated MA956 alloy (b) hardness of irradiated an unirridated T91 alloy.

In another experiment, alloys T92 and MA956 specimens were irradiated with 122 MeV Ne ions alloy. The irradiation temperatures were 440 and 575°C, and the doses were 1, 2 and 10 dpa. The damage profile estimated using SRiM 96 code is illustrated in Figure 144, and the peak damage range was found to be at around 30 micron. One optical cross sectional micrograph (Figure 145) shows that some cavities are produced along the depth of 31 micron, exactly at the predicted peak damage range. As the center region of the irradiated area is approached the cavity size increases and a bulge was observed. In contrast to T92, ODS alloy MA956 specimens did not show any cavities. In this study the peak damage range estimated using the code has been found to be quite accurate and ODS alloys were again confirmed to be more resistant to the beam irradiation than F-M steel.

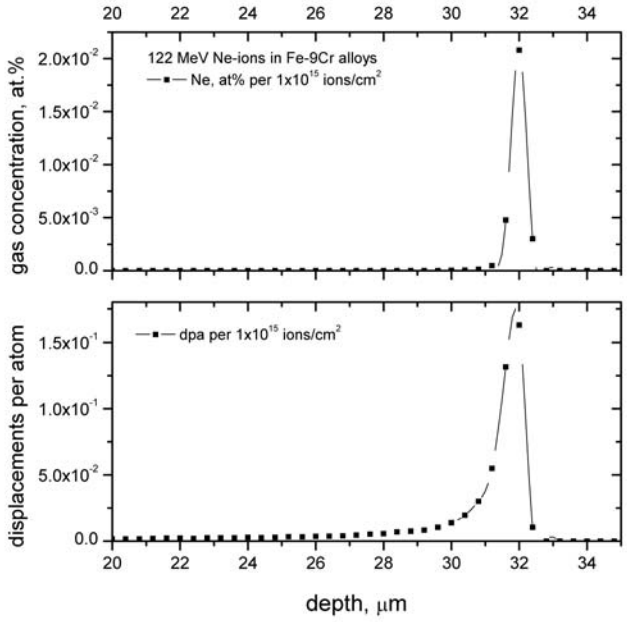

Figure 144 Damage profile of Fe-9Cr steel when irradiated with 122 MeV Ne ions; peak damage range at about 32 micron.

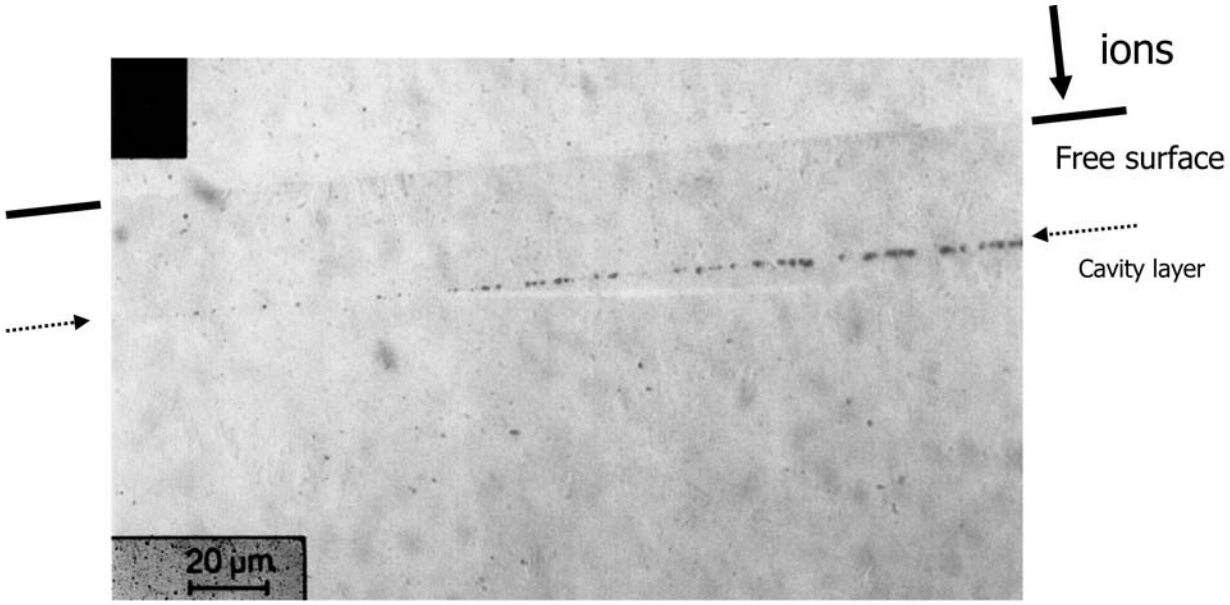

Figure 145 Optical micrograph of T92, irradiated with 4.5 dpa of 122 MeV Ne ions at 520°C.

5. Task 5 – Weld Behavior

5.1 Task Summary

Cladding and core internal components will have to be joined. The behavior of the weld microstructure may be an issue in materials exposed to the environment of the supercritical water reactor. The weld behavior study involved the production of welds in F-M alloys T-91 and HCM12A in order to evaluate the response of samples exposed to the SCWR environment. This task was modified from the original work scope to only include investigation evaluation of weld response rather than a more detailed study on alloy weldability. The modification was made based on comments from reviewers at the annual project presentations.

5.2 Preparation and welding of Grade 91 and HCM12A F-M alloys for corrosion and SCC study

Contributors:

James Cole, Jan-Fong Jue, INL

5.2.1 Welding Details

Ferritic-Martensitic (F-M) alloys Grade 91 and HCM12A plates were joined by GTAW (Gas-Tungsten-Arc-Weld) at Idaho Nation laboratory. According to the literature, the welding F-M alloys requires several cautions such as preheating the work pieces, selection of the proper filler and post-welding heat treatment. To avoid hydrogen cracking, the steel plates were first pre-heated to 250^{o}C then the GTAW was performed with filler. The filler used was Blue Max LNT 9CR(P91). The composition of the filler is Fe - 8.7Cr – 0.9Ni - 0.7Mo - 0.7C - 0.7Mn– 0.4Si – 0.2V – 0.04Nb – 0.005N. After welding, the joined pieces were air-cooled. A post welding treatment was conducted at 750^{o}C for 3 hours in air followed by furnace cooling. The post weld treatment is necessary to obtain the proper weld structure and adequate toughness. An oxide layer was developed after post-welding annealing. The surface oxidation layer was removed by machining the top face of the plate flat before they were shipped to the Shular Tool in Tennessee and EDM machined into SCC bars and coupons as shown in Figure 146. The finished corrosion coupons were shipped to the University of Wisconsin, while the SCC bars were sent to the University of Michigan. Testing of the samples will be completed under the GEN IV SCWR program. Some cross sections were cut from the welded plates and polished to a 0.05µm surface finish using a colloidal silica solution. The polished surfaces were then etched using a Nital solution (2%HNO_3 and 98% methanol).

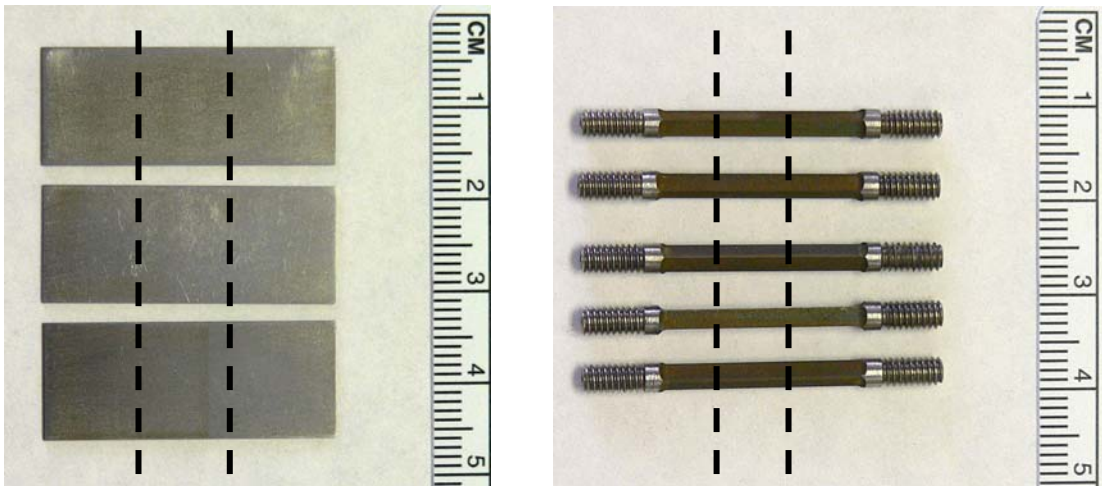

Figure 146 Images of weld samples. Area between dashed lines indicate the approximate location and width of the weld zone.

5.2.2 Weld Microstructures

Figure 147 contains optical micrographs from the T91 welded plate containing 9% Cr. Figures Figure 147 (a)-(c) show the microstructure of the weld-zone, the heat affected zone (HAZ) and the matrix respectively. . As shown in Figure 147 (d), the interface between weld and the base metal is very good.

Figure 148 provieds optical micrographs from the welded HCM12A plate containing 12 % Cr. Figure 148 (a) – (c) to 9 are grain structure of the weld-zone the HAZ and the matrix, respectively. Figure 148 (d) again shows a good interface between the weld and the base metal. The HAZ in the 9%Cr containing plate exhibits larger grain size than the plate containing 12%Cr. The weld zone of the 9% Cr containing plate also exhibits a slightly coarser microstructure.

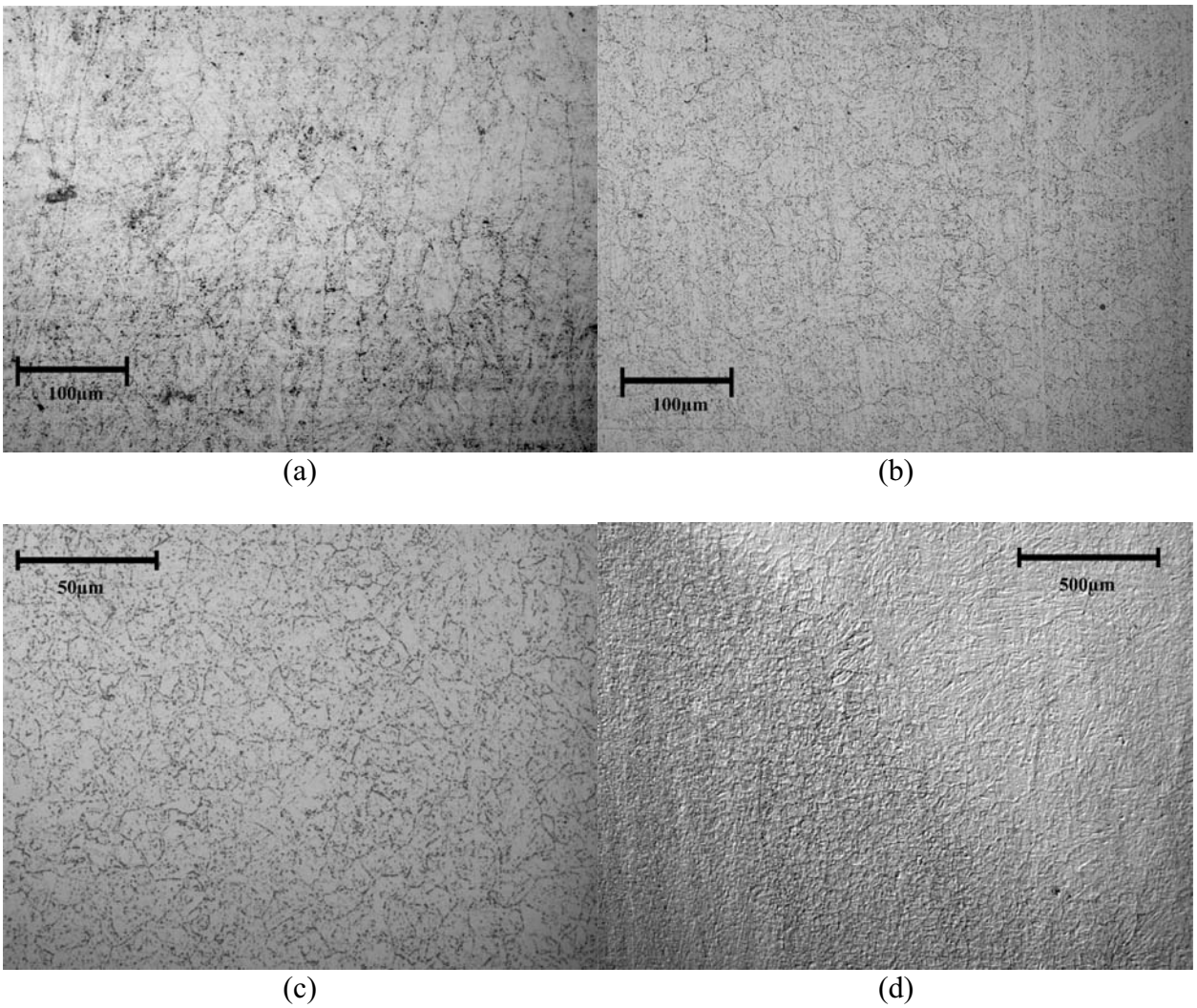

(a) (b)

(c) (d)

Figure 147 Optical images of weld and base metal in alloy T91: (a) Weld Zone, (b) HAZ, (c) Base Metal and (d) Interface between zones.

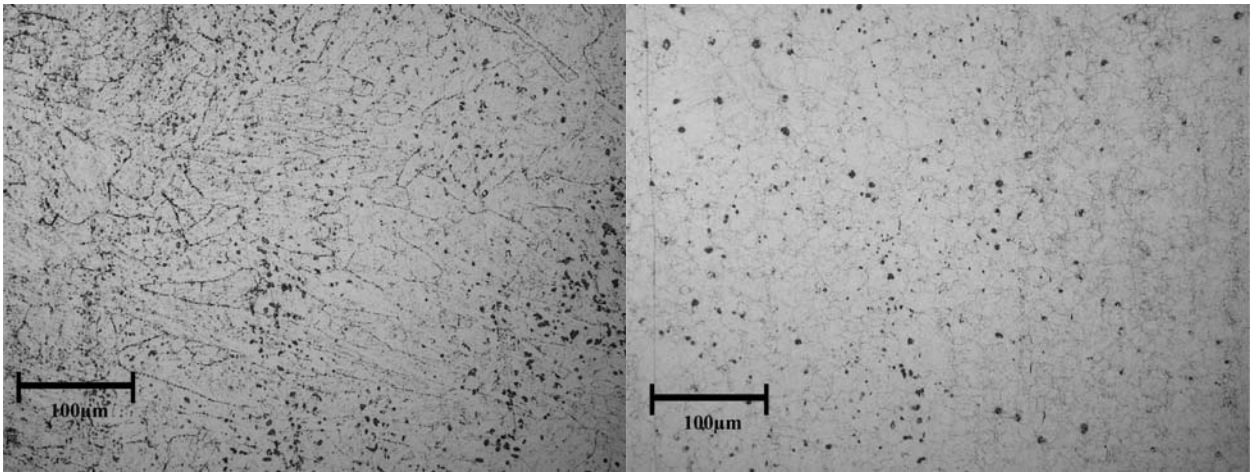

(a) (b)

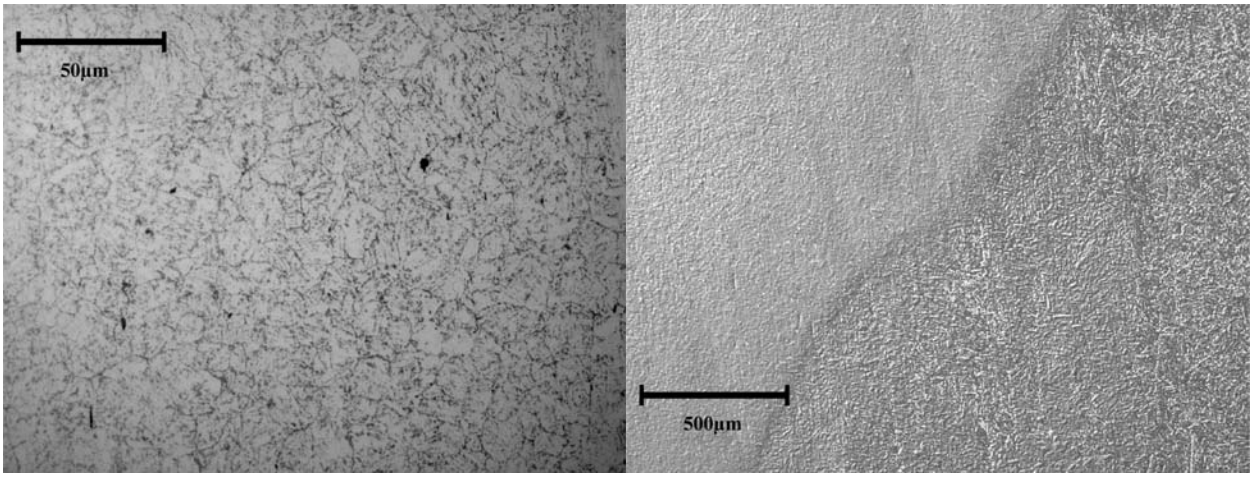

(c) (d)

Figure 148 Optical images of weld and base metal in alloy HCM12A: (a) Weld Zone, (b) HAZ, (c) Base Metal and (d) Interface between zones.

6. Task 6 - Irradiation Test Plan

Contributors:

James Cole, Joy Rempe and Terry Totemeier, INL
Todd Allen and Kumar Sridharan, U. W.
Gary Was, U. M.
Jinsung Jang, KAERI

6.1 Task Summary

Qualification of materials for SCWR systems will ultimately require irradiation testing. Based on the results of this project, recommendations are made for candidate materials and sample types to be irradiated to understand irradiation performance of core materials. This collaborators in this project have coordinated these activities with the larger GEN IV research program.

6.2 Summary of Materials and Irradiation Testing Recommendations

6.2.1 Overview

This brief summary is intended as a preliminary set of materials and irradiation testing recommendations based on qualification data collected as part of INERI project 2003-008-K, "Developing and Evaluating Candidate Materials for GEN IV Supercritical Water Reactors". Because similar and more extensive irradiation test plans are being assembled by the GEN IV National Technical Directors, the recommendations in this section should be viewed in context of the broader effort to develop candidate materials for the SCWR.

6.2.2 Materials Recommendations

Table 24 provides a summary of the materials recommendations for future irradiation testing campaigns. It is very much in line with the initial literature search conducted as part of the project. However, several additional limitations were identified in the qualification testing phase of the project.

Initial ion-irradiation studies indicate that the Fe-based ferritic-martensitic (F-M) alloys will have high resistance to swelling, which is a desired quality for components which will reside in core for longer periods of time. However, the advanced candidate F-M alloys, which were selected because of their widespread use in fossil supercritical water plants, were shown to have significant general corrosion when exposed to SC water over a range of temperatures and water chemistry conditions. In a fossil plant, where most components have thick cross-sections and can be routinely replaced, such general corrosion may not be an issue. For thin walled components such as fuel cladding, corrosion through a significant fraction of the wall thickness is unacceptable. Thus current advanced F-M alloys may not be suitable for cladding applications.

Because of the high rate of oxidation of the F-M alloys, it may be necessary to consider swelling resistant austenitic stainless such as alloy D9 for cladding applications. Such steels were developed for the fast breeder reactor program, and additional evaluation of these materials in terms of irradiation-

assisted-stress-corrosion-cracking and swelling under SCWR relevant irradiation conditions should be performed. The high Ni and Cr Fe-based Alloy 800H and Ni based alloys, such as alloy 690 should also be considered, however, previous and somewhat limited experience with helium embrittlement of irradiated alloys containing higher levels of nickel must be evaluated over the range of irradiation conditions relevant to the SCWR.

Although the scope of this project did not permit extensive examination of oxide dispersion strengthened (ODS) alloys, recent research in Japan has shown that ODS alloys can be tailored to specifically address some of the limitations of the F-M alloys such as excessive corrosion. These Japanese studies also indicate that ODS alloys have better high temperature creep strength. ODS alloys

Table 24 List of candidate alloys recommended for further irradiation testing.

Alloy Class	**Alloy**	**Potential Components**	**Issues**
Ferritic-Martensitic			
	T92 (NF616)- Fe-9Cr-MoVNb	Thick section components where greater general corrosion rates can be accommodated.	General corrosion limits use in thin section components. Low temperature irradiation embrittlement needs to be evaluated.
	T122 (HCM12A)- Fe-12Cr-MoVNbW	Thick section components where greater general corrosion rate can be accommodated	General corrosion limits use in thin section components. Low temperature irradiation embrittlement needs to be evaluated.
Austenitic Stainless Steels			
	Alloy D-9- Ti–Modified Fe-15Cr-15Ni 2.2Mo	Potential use for cladding and other components where higher corrosion resistance is needed.	Low thermal conductivity. Potential susceptibility to irradiation assisted stress corrosion cracking. Evaluation of swelling behavior over SCWR temperature range needs to be evaluated.
High Ni alloys			
	Alloy 690 Ni-30Cr-10Fe	Potential use for cladding and other components where higher corrosion resistance needed.. Components where high temperature creep strength needed.	Potential susceptibility to IASCC. Irradiation-induced grain boundary embrittlement needs to be evaluated..
	Alloy 800H Fe-32Ni-20Cr-TiAl	Potential use for cladding and other components where higher corrosion resistance needed..	Potential susceptibility to IASCC. Irradiation-induced grain boundary embrittlement needs to be evaluated.
ODS			
	Developmental 9-14 Cr ODS alloy	Cladding	Corrosion and low temperature irradiation embrittlement behavior need to be evaluated. Fabrication costs.

are in the early stages of development and are expensive to fabricate. As a result, they will require a more extensive R&D effort than commercially available alloys. However, because of there potential, this R&D effort should be seriously considered.

6.2.3 Irradiation Testing Recommendations

As a first cut, existing irradiated materials such as those irradiated as part of the fusion and/or fast breeder reactor programs should be considered for testing in supercritical water. This will serve two purposes, 1) develop a methodology for testing of irradiated components in SC water and 2) provide some initial lower cost data to guide future, more in depth testing campaigns. In the absence of in-pile testing capabilities, a variety of specimens including tensile, creep, fracture toughness and microstructure should be irradiated over the range of temperatures relevant to the SCWR (300-600°C). Post-irradiation testing of the irradiated materials in SC water can then be conducted to ensure that irradiation under conditions relevant to the SCWR do not lead to excessive swelling, embrittlement or loss of high temperature creep strength. In order to save costs, such irradiations can be piggy-backed onto current irradiation testing programs planned for either the Advanced Fuel Cycle Initiative or combined with other GEN IV materials irradiation programs where irradiation conditions overlap.